PHYSICS-BASED MODELING OF WAVE PROPAGATION FOR TERRESTRIAL AND SPACE COMMUNICATIONS

by

Feinian Wang

A dissertation submitted in partial fulfillment
of the requirements for the degree of
Doctor of Philosophy
(Electrical Engineering)
in The University of Michigan
2006

Doctoral Committee:
Professor Kamal Sarabandi, Chair
Professor Anthony W. England
Professor Wayne E. Stark
Associate Professor Mahta Moghaddam

To my lovely wife, Xin Li

ACKNOWLEDGEMENTS

I would first like to thank my advisor Professor Kamal Sarabandi for his continuous guidance and mentorship during my graduate studies at The University of Michigan. It has been a pleasant journey learning from and working with him. I also wish to thank Professor Tony England, Professor Mahta Moghaddam and Professor Wayne Stark for serving on my dissertation committee and for their thoughtful feedback.

Additionally, I would like to thank all the Radiation Laboratory faculties for their great knowledge and abundant research experience that helped me and many other students towards success. The Radiation Laboratory staff Karen Kirchner, Mary Eyler, Karla Johnson, Richard Carnes, and Susan Charnley, as well as the EECS department staff Beth Stalnaker and Karen Liska, deserve particular thanks for their kind and timely support. Special thanks are devoted to the agencies who provided generous financial support for my graduate studies, namely the Defense Advanced Research Projects Agency (DARPA) and the Jet Propulsion Laboratory (JPL).

I am indebted to all of my colleagues and friends in the Radiation Laboratory, especially to Il-Suek Koh who provided me great amount of tutorial and discussion on my research, to Mark Casciato for his help with my English writing, to Adib Nashashibi for helping me to conduct millimeter-wave foliage propagation measurement, to Leland Pierce for his enormous support on computer problems, and to many of my Chinese friends, Xun Gong, Xin Jiang, Zhang Jin, Yingying Zhang, Zhongde Wang, Pan Liang, Yongming Cai and Hua Xie for their encouragement and help. I also owe a special thanks to Professor Tai who gave me invaluable advice and lessons

from his life experience.

Finally and most importantly, I would like to express my deepest gratitude to my family: to my parents Jun Wang and Yinfeng Fan for their selfless love and sacrifice, to my lovely wife Xin Li for her continuous love, understanding and support, and to my dear son Aris for being the best gift ever to me.

TABLE OF CONTENTS

LIST OF TABLES

Table

LIST OF FIGURES

Figure

CHAPTER 1

INTRODUCTION

In 1864 *James Clerk Maxwell* established his famous equations and predicted the propagation of electromagnetic waves in free space at the speed of light. This was later proved by *Heinrich Rudolf Hertz* who conducted the historical experiment demonstrating the generation, propagation, and reception of radio waves. Inspired by these profound events, numerous innovations and new applications using radio waves instead of wirelines appeared in the first half of the 20^{th} century, such as wireless telegraph, broadcasting radio and television, navigation systems, and radar (radio detection and ranging). After a relatively quiet period, wireless communication again entered a splendid era in the 1990s with the advent of advances in digital communication technology and the prevalence of the internet. The ever-increasing demand for personal mobile communications has been the underlying driving force. For example, by mid-2000, more people in Europe had mobile phones than had personal computers or cars, and the number of cell phone subscribers in the U.S. reached about 118 million in 2001 [1]. Even bigger markets exist in developing countries such as China and India. In addition, wireless data services are becoming more and more frequent in our daily life. More and more people are using cell phones or PDAs (Personal Data Assistants) to access the internet for weather, traffic, or stock information while on the road. Using a laptop computer to surf the web or conduct M-commerce activity

through WLAN or Bluetooth in university campuses or a Starbucks café is more often seen. And subscribers to the satellite TV/internet or wireless local loop (WLL) in residential areas just keep increasing.

The amazing beauty of wireless communication lies in the fact that information is carried by an electromagnetic wave which propagates in free space and can potentially reach anywhere in any direction and distance. This provides the advantage of mobility and accessibility in that one or both communication ends are free from being attached to fixed cables. Sensors in the most remote areas on Earth can communicate with others, and beyond the globe radio links between spacecraft, satellites, space and ground stations are able to convey important information for various civilian, scientific and military applications. Such flexibility comes at a price: wireless communication channels involve complex environments inside which electromagnetic waves are propagating. Such environments generally pose great challenges on the wireless systems because:

- the waves propagating in these environments are not confined in space, as opposed to those in a transmission line;
- these environments usually contain numerous scatterers that interact with the propagating wave in a very complicated manner, e.g. the buildings in a city, trees, hills or mountains in rural areas, and rain drops in the atmosphere;
- often times the wireless channels are shared by multiple users, therefore wave signals of any individual user are susceptible to interference from other users in the same environment.

In order to overcome these constraints, in-depth knowledge of the wave propagation behavior in complex wireless channels is needed. Characterizing such behavior by conducting physical measurements is extremely expensive and inefficient. However, the alternative of using physics-based modeling of wave propagation in complex environments with fast computers in conjunction with Monte Carlo simulation has

attained prominence in recent years [2, 3, 4]. These models allow for simulations directly based on the physical environment, and give insight into the mechanisms of radio wave propagation. Therefore these models inherently provide much more accurate results compared to other heuristic empirical models, such as the Okumura model [5], and oversimplified analytical models, such as the Longley-Rice model [6]. Also such a physics-based modeling methodology is more comprehensive and generally applicable to a broad class of wireless communication scenarios. In addition, these computer-aided wave propagation models have the advantage of low-cost as compared to conducting physical measurements. If all detailed features of the physical environment are captured and correctly represented, these models can essentially run "experiments" in a virtual environment simulated on a computer. Not only signal power but also its phase, spatial and spectral correlation functions, and wideband time domain response can all be characterized. The statistical nature of the wave propagation channel can be accounted for by Monte Carlo simulation.

Despite significant progress in physics-based modeling of wave propagation for wireless applications, there are still many at standing problems to be solved in order to improve the propagation models both qualitatively and quantitatively. In this dissertation, two very challenging problems related to wave propagation for wireless systems are considered. One topic is related to the problem of wave propagation in foliage which is often encountered in terrestrial communications. The other topic involves enhancing the upward radio link between a ground station and a deep-space spacecraft. Complex electromagnetic models are developed in this dissertation to treat the wave propagation in random volumes and rough surfaces. These models are needed in order to deal with the practical issues encountered in the above two wireless applications in terrestrial and deep-space communications. The skills required to treat these problems are essentially the same and that is why such two apparently disparate problems are treated in a single dissertation. In the following sections the nature of

wave propagation in foliage and deep-space communication are described in detail and specific contributions of this dissertation to these problems are clearly presented.

1.1 Wave Propagation in Forested Environments

In many wireless systems such as land mobile communication systems as well as microwave remote sensing systems, vegetation such as trees, bushes, and crops may appear in the wireless channels. Channel characteristics need to be thoroughly studied if the accuracy of the system planning tools are to be improved and the spectrum utilization optimized. Foliage can obstruct the line-of-sight between the transmitter and receiver of a communication system or can obscure the view of a microwave sensor such as a radar. Scattering and absorption of the propagating wave by numerous foliage scatterers such as branches and leaves can significantly affect the wave propagation behavior and hence the electromagnetic filed at the receiver or an observation point. The wireless channel becomes extremely complex in this case due to the involvement of a forested environment. Existing empirical foliage channel models, such as the Weissberger model [7], are constructed from measured data under specific environmental and system conditions, and are not directly connected to the physical processes involved. Such limitations prevent these empirical models from general use. On the other hand, commonly used analytical foliage models are generally oversimplified and have very limited regions of validity. For example, one type of analytical model treats the foliage medium as dielectric slab(s) with constant permittivity and conductivity and employs ray-based methods to capture direct, reflected, and diffracted field components [8, 9]. In case the distance between the transmitter and receiver inside the medium is large, a lateral wave that propagates along the air-canopy interface has been shown to be very important [10]. However, such models are essentially low-frequency models since the slab approximation for the foliage medium is only valid at low frequencies (e.g. < 250 MHz).

Recently, physics-based foliage wave propagation models have attracted significant attention by representing the foliage as a mixture of trunks, branches, and leaves, while including all important mechanisms of radio wave interaction with these discrete scatterers [11, 12, 13]. Each particle (scatterer) is described by a simple geometry with complex permittivity and a spatial location as well as orientation. The statistical nature of the forest structure can be realized by associating the size, location and orientation of foliage scatterers with certain pre-assumed probability density functions (PDFs). A more accurate representation of the forest medium has been developed recently by using fractal geometry theory to generate realistic-looking trees, and placing tree samples randomly into a specified area [14]. Both radiative transfer and distorted Born approximation methods have been employed in the literature to compute the wave propagation inside a forested environment containing discrete scatterers. Radiative transfer [15, 16] is a heuristic method based on the law of energy conservation. This method only deals with power, therefore it supplies no phase information and neglects any coherence effect [13]. In addition, the radiative transfer method cannot be easily implemented for a forested environment, which is a complex three-dimensional (3D) medium with plenty of large scatterers, due to the lack of definition for the "unit volume" required by the integro-differential radiative transfer equation (RTE). On the other hand, the distorted Born approximation (DBA) method [11, 16] provides a better solution for modeling wave propagation inside forested environments. This method is based on stringent electromagnetic wave theory and hence is more accurate in terms of providing the coherence effects and phase information. Also DBA works quite well in dealing with large scatterers in the complex forest environment.

Based on a fractal-tree generator and a DBA wave computation engine, and in conjunction with a Monte Carlo simulation, a fractal-based coherent scattering model (FCSM) has been developed in the Radiation Laboratory at the University of Michi-

gan [14], and been applied to a number of different problems [17, 18, 19]. A detailed review of this model is given in Chapter 2 of this dissertation. Although it may be the most accurate foliage wave propagation model by far, FCSM has its own limitations, including:

- questionable applicability at millimeter-wave frequency range;
- extensive computation required for large distance wave propagation inside foliage;
- unmodeled multiple-scattering components;
- complicated implementation and difficult access for use.

It is the intent of this dissertation to develop more accurate and simple-to-use foliage propagation models by overcoming the above limitations of FCSM for many important applications.

Enhanced FCSM at Millimeter-Wave Range

Wideband wireless communication and remote sensing systems at millimeter-wave frequency are attracting more and more attention in recent years as a result of increasing demand for high data rate wireless applications. Forested environments pose a significant challenge for the operation of such systems. In order to assess the performance of these high frequency wireless systems, an accurate foliage propagation model at such high frequencies is required. The Weissberger model covers frequencies from 230 MHz to 96 GHz, however this model is an empirical model based on limited measured attenuation data carried out in several specific forest environments in the U.S., and hence is not generally applicable. Several vegetation path-loss models based on the radiative transfer method have been developed for millimeter-wave frequencies [20, 21, 22]. These models are semi-empirical though, in the sense that they all require input values of several model parameters based on measurement results. In addition, the above millimeter-wave foliage models only provide power information

while other important channel characteristics related to fields is not available. Wave theory foliage models working at millimeter-wave frequencies have not been developed yet in the literature. Physics-based foliage models based on the DBA method are only validated up to X-band [13]. It has been shown recently that applying the existing DBA models such as FCSM at millimeter-wave frequency can cause significant overestimation of the wave attenuation rate [23]. Such a limitation of FCSM is related to Foldy's approximation [16, 24] used to estimate the coherent mean-field. This approximation only applies for a sparse medium due to the employment of a single-scattering formulation. This is not the case for densely clustered foliage. Such inaccuracy is not significant at low frequencies where mutual coupling between foliage particles is negligible. While at millimeter-wave frequency range, such an effect is magnified to a degree where the multiple-scattering among leaves in a leaf cluster is no longer negligible. In this dissertation, an enhancement of FCSM is achieved by including the mutual coupling among leaves of the dense leaf clusters, which extends FCSM's region of validity up to Ka-band (35 GHz). Details regarding this work are presented in Chapter 3.

FCSM-Based Foliage Path-Loss Model

Accurate estimation of signal attenuation in highly scattering environments such as a forest has long been a challenging problem. The challenges arise from the fact that the incoherent power becomes dominant after the wave propagates for a long-enough distance. This results in a different slope of the foliage path-loss (in dB) at larger distances, compared to the much steeper slope for coherent power at closer distances. This is the so-called "dual-slope" phenomenon of the foliage path-loss often observed experimentally in forested environments [20, 25, 26]. Current models used to predict foliage path-loss are again those empirical or semi-empirical models which are not generally applicable. Analytical models such as those based on a slab

approximation and ray tracing methods are too simple to be valid, and the prediction of foliage path-loss at large distances by these models tends to be very erroneous. The physics-based FCSM model is an ideal candidate to attack such a problem in that it is able to capture the incoherent power contributed by the scattering from foliage particles. However, the extensive computational requirement of FCSM poses a great challenge. Computing scattered fields from all scatterers inside a large forest environment can be prohibitively time-consuming. In addition, FCSM is essentially a single-scattering model. For highly scattering environments and long propagation distances, multiple-scattering components become important in contributing to the incoherent power. In this dissertation, a statistical wave propagation model, SWAP, based on FCSM is developed to tackle these issues. Compared to a brute force approach which applies FCSM to the whole forest domain, the computation time of SWAP is significantly reduced since the extensive wave propagation computation is only confined to a single block of forest with much shorter range. Meanwhile the prediction accuracy is improved since the multiple-scattering components between scatterers inside different forest blocks are taken into account in the SWAP model. Details of this work are provided in Chapter 4.

Macro-Modeling Foliage Path-Loss

The FCSM and SWAP models have proven to be very accurate foliage propagation models. However the implementation of both FCSM and SWAP is very complicated. The existing codes for these models are developed in such a researcher-oriented way that ordinary users without enough knowledge on the subject find them too difficult to use. Even though a user-friendly interface could be designed so that users can set up the simulation with relative ease, the extensive computational requirements, such as powerful computers and long computation time, may still work against routine use of these models, especially for applications that require real-time computing. Therefore,

a macro-model with simple mathematical expressions similar to those in the empirical models is of great interest. Such a macro-model can be extracted from a large number of simulations based on the complicated FCSM or SWAP models. This procedure is analogous to developing empirical models from real experiments, but is much more cost-efficient and flexible due to the capability of simulating wave propagation inside any particular forest environment of interest. In this dissertation, a foliage macro-model named Michigan Foliage Attenuation Model (MiFAM) is developed based on this methodology to provide much more accurate prediction of foliage path-loss than the empirical models, while being as simple to use as those empirical models. Details of developing such a model are provided in Chapter 5, and examples of MiFAM for two typical tree species, red maple and red pine, are provided at UHF-band (300∼1100 MHz).

1.2 Phase Calibrating Uplink Ground Array

Space exploration is undergoing a great boom fueled by exciting missions spread throughout the solar system. Spacecraft such as the Voyagers are even traveling towards the boundary of the solar system which is thought to exist somewhere from 8 to 22.5 billion km (5 to 14 billion miles) from the sun. As of January 2006, Voyager 1 has traveled about 98 AU (astronomical unit, 1 AU $\sim$ 93 million miles and is the distance from the Earth to the Sun), after being in space for more than 28 years [27]. In order to maintain a reliable link as the distance between a ground station and a deep-space spacecraft increases, the effective isotropic radiated power (EIRP) of the radio link must be increased. Considering the limited available power and space on a spacecraft, most efforts on improving EIRP must be concentrated on the earth ground station. Current state-of-the-art NASA (National Aeronautics and Space Administration) DSN (Deep Space Network) ground stations are capable of transmitting a maximum EIRP of 149 dBm (0.8 TW) at S-band (2.1 GHz), 146 dBm

(0.4 TW) at X-band (7.2 GHz) with 70-m reflector antennas, and 138 dBm (0.07 TW) at Ka-band (35 GHz) with 34-m reflector antennas [28, 29]. A factor of about 13 dB for the EIRP enhancement is expected in the next two decades. Although serious limitations on power and space do not exist for ground stations, technological and economic challenges do exist. For instance, ground stations become dramatically more expensive as the size of their antennas increases [30].

The prohibitive cost of building colossus precise reflector antennas has triggered an effort to find alternative solutions for the problem [31, 32]. One of the most promising approaches is to use an array of many dish antennas, which provides a number of advantages including considerable cost-reduction. Currently the cost of building a single 70-m antenna station is about $100M, while about forty 12-m reflector antennas would produce the same performance for only a fraction of the cost [33]. However, difficulties exist for this approach in achieving phase coherence among the array elements in order to combine their signals at the receiver constructively. It turns out that for downlink operation, the proper phase distribution can be obtained *a posteriori* by cross-correlating recorded signals at each array element [34]. Such a technique cannot be used at the spacecraft for uplink arraying simply because the receiver of the spacecraft could not align signals from different ground antennas. Therefore the phase coherence of these signals has to be determined on the ground so that they arrive at the spacecraft receiver coherently. However, considering the large size of each antenna element and the distant spacing between these elements, it is very challenging to determine the phase center locations of all the elements to within a small fraction of the wavelength at the operating frequency (X- or Ka-band). Another factor that exacerbates the difficulty of achieving array phase coherence is the earth movement. To maintain the beam on the spacecraft, the array elements all have to track the spacecraft as the earth rotates. Since the rotation pivots of the antennas are not necessarily collocated with the antenna phase centers, the phase distribution

among array elements must be determined for all possible array attitudes.

This dissertation presents some original work on achieving phase coherence of an uplink phased array system containing a number of sparsely distributed large reflectors, through phase calibration. Very little research regarding this problem has been conducted in the literature. Therefore the relevant work in this dissertation is of great importance and novelty. Three different phase calibration methods are proposed and their feasibility studied through physics-based modeling of wave propagation in the respective calibration scenarios.

Radar Calibration Using LEO Targets

This method is based on a radar calibration approach in conjunction with the concept of phase conjugation. The system infrastructure is designed so that each array element can operate in both uplink and downlink modes. A group of orbiting space objects, such as low earth orbit (LEO) satellites are potential calibration targets. The abundance of such targets and their orbiting behavior can supply calibration opportunities at any required array attitude. An aerospace software, STK, can be employed to investigate such calibration opportunities. However there is a critical issue associated with this method which lies in the fact that the calibration targets usually fall into the near-field zone of the whole array. A path-length compensation technique is provided to resolve this problem. The performance of this calibration method is studied statistically by modeling the random positions of array element phase centers and the calibration targets, as well as signal phase fluctuation, in a Monte Carlo simulation. Details of this calibration method are presented in Chapter 6.

Radar Calibration Using the Moon

This method is also a radar calibration approach, but with all array elements operating in uplink mode only to save the unit cost of each element. Correspondingly the calibration has to be conducted in uplink mode as well. Orthogonal PN (pseudo noise) codes find the proper application in this all-transmitter array calibration scenario. The moon is selected as calibration target since it falls within the array far-field zone, therefore the undesired near-field effect does not exist. The difficulty of this method stems from the fact that the moon cannot be treated as a point target, instead it appears as a distributed target from the perspective of the Earth ground array. Synthetic aperture radar (SAR) imaging technique can be employed to overcome this difficulty. In addition, the lunar surface is essentially a random rough surface, and the backscattering of the incoming waves by such a surface must be modeled statistically. Details of implementing this calibration scheme are provided in Chapter 7.

Calibration Using VLBI Infrastructure

This last method is a different one based on the existing VLBI or VLA (Very Large Array) infrastructures. Celestial radio emitters, Quasars, serve as beacon sources and the downlink phase differences between array elements can be measured through cross-correlation of the received signals. Such phase differences are treated as references for determining the phase calibration values for uplink operation of the array. However, system modification of the existing downlink-only infrastructure is necessary. Several schemes are proposed and their feasibilities are studied in Chapter 8.

1.3 Dissertation Outline

This dissertation is composed of 9 chapters. The first major part includes the next 4 chapters and deals with modeling the wave propagation through forested environments. As mentioned above, Chapter 2 introduces the basis model, FCSM, as a computation engine for further advanced modeling. Chapter 3 enhances the FCSM model at millimeter-wave frequency range by accounting for the multiple-scattering inside leaf clusters when estimating the coherent mean-field. In Chapter 4, the foliage path-loss model, SWAP, is developed by dividing the forest into statistically similar blocks along the direction of wave propagation, and then applying FCSM to a typical block to estimate the wave propagation behavior. Such behavior is common and can be reused for all the forest blocks in a network cascading fashion. Chapter 5 attempts to derive a simple-to-use macro-model for foliage path-loss, based on numerous simulations using the complicated SWAP model. As the second major part of this dissertation, Chapter 6−8 present three methods for phase calibrating a large-reflector uplink ground array. Chapter 6 proposes a One-Transmitter-All-Receiver (OTAR) radar calibration approach based on the concept of phase conjugation. LEO satellites are candidates of the calibration targets. Chapter 7 provides a All-Transmitter-One-Receiver (ATOR) radar calibration approach which uses the Moon as calibration target. And Chapter 8 describes a different downlink approach using the existing VLBI/VLA infrastructures. In the end of this dissertation, Chapter 9 draws the conclusions and motivates the future work.

CHAPTER 2

FCSM: COMPUTATION ENGINE FOR FOLIAGE WAVE PROPAGATION MODELING

2.1 Introduction

Fractal-based Coherent Scattering Model (FCSM) is a wave theory model developed in the Radiation Laboratory at the University of Michigan to simulate radio wave propagation through foliage [14]. This chapter is devoted to outlining the features of this model, as it will be used as a baseline for: 1) enhancing its region of validity; 2) using it as a tool for developing other models presented in this dissertation. The algorithm of FCSM consists of three major components. The first component of FCSM is related to modeling of complex tree structures in a deterministic fashion using simple mathematical and statistical algorithms. The computer-generated forest is made up of realistic-looking trees described by fractal geometry [35]. The second component of FCSM is the electromagnetic engine where the distorted Born approximation (DBA) method is used to compute the wave propagation and scattering from the vegetation constituents. The algorithm is developed so that a forest stand of mixed or single species can be treated in a computationally efficient manner. Finally the third component of FCSM derives the statistical parameters of wave propagation through repeated calculation of wave propagation for different realizations of a statistically homogeneous forest stand. Such a Monte Carlo simulation procedure leads

to a number of samples of the received field, from which the field statistics such as the average received power and spatial or temporal correlation functions can be obtained. The advantage of FCSM is its inherent fidelity since it accounts for detailed tree architecture, which has been shown to significantly influence the wave scattering and attenuation by foliage [37, 38]. In addition, being a wave theory model, FCSM supplies complete information of the propagating wave including power, phase, and field polarization. The Monte Carlo simulation provides a database for statistically estimating all desired quantities and their random distributions, taking into account the random medium nature of the forested environment. Correspondingly, the performance of FCSM is then determined by three factors each associated with one of the three components, i.e. the fidelity of how the forested environment can be reconstructed, the accuracy of the wave propagation computation, and the number of realizations carried out in the Monte-Carlo simulation. In what follows, different components of FCSM are briefly reviewed and its applications and limitations are presented. For more details, one can refer to the original papers [14, 39].

2.2 Forest Reconstruction Using Fractal Theory

With computer graphics, various tree species of different architectures can be generated based on a fractal tree model using statistical Lindenmayer systems (L-systems) [14]. L-systems are well-known tools for constructing fractal patterns such as the geometrical features of most botanical structures in which self-similarity is preserved through a so-called rewriting process [36]. Such a recursive process based on simple structural grammar rules can easily be implemented by computers. Figure 2.1 shows an example of the growing process of a 2D fractal tree, and Figure 2.2 shows computer-generated branching structures of two different kinds of 3D fractal trees, namely deciduous and coniferous trees respectively. Leaves with a known geometry such as circular or elliptical disks can be generated as well, and attached to the

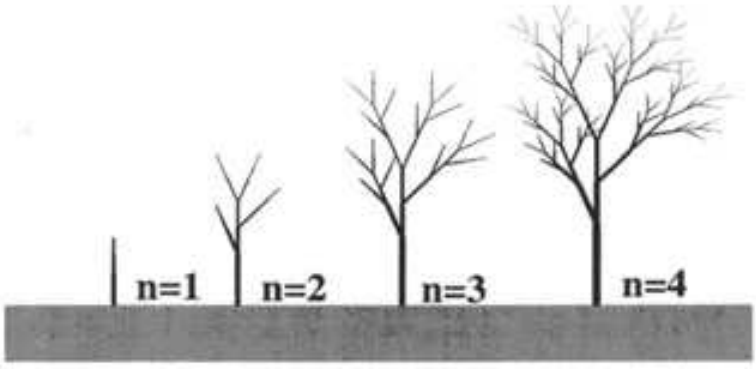

Figure 2.1: Four steps of the growing process of a 2D fractal tree (adapted from [14]).

branches with realistic orientations. Randomly varying these structural parameters, a number of tree samples are then generated and their locations inside the forest are assigned randomly according to certain parameters such as tree density and minimum tree spacing. By placing the tree samples into an area of specified dimensions, a tree stand, i.e. a block of forest, can be formed.

The fidelity of the computer-reconstructed forest environment depends on two factors, namely the fractal scheme and the geometrical parameters. The fractal scheme is defined based on the architecture of a particular tree species. For example, how the branches will taper as they grow higher vertically and farther horizontally? How the next branch will change its orientation compared to the previous one? And how branchy the tree will be? These details are all determined in a structural grammar file called the "DNA" file for each specific tree species, where a number of user-defined symbols representing different growing commands (e.g. move forward, reduce diameter, and rotate azimuthally) are combined in a specific way according to the botanical architecture. The length of the growing process, i.e. the number of iterations of rewriting, is also defined in the DNA file to determine the density of branches.

With the fractal growing scheme defined, one needs the specific quantities of the structural parameters to generate a realistic-looking tree. These include tree and

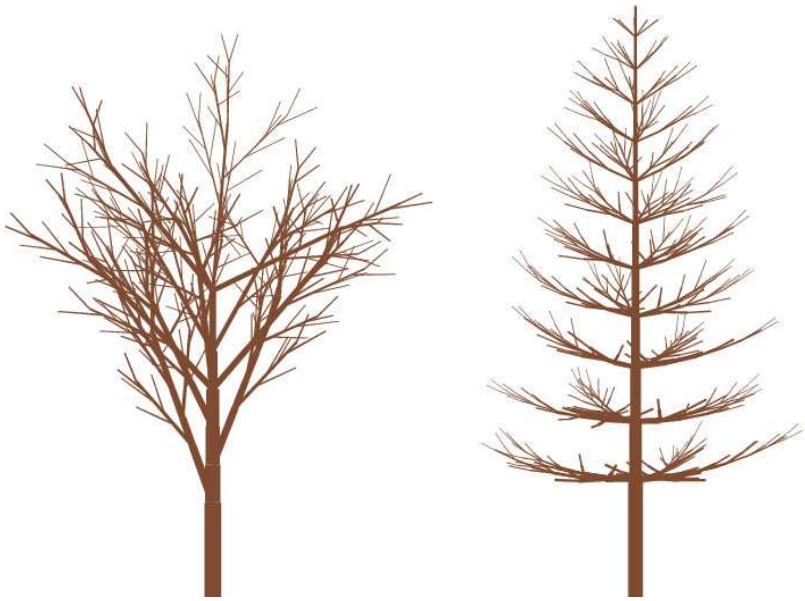

(a) (b)

Figure 2.2: Two different kinds of 3D tree branching structures, (a) deciduous tree; and (b) coniferous tree.

trunk height, crown radius, trunk diameter and tilt angle, branching (elevation) angle and rotation (azimuth) angle, branch forward step distance and tapering ratio (both vertically and horizontally), leaf orientation angle, number of leaflet, leaf dimensions, stem radius, stem length, etc. Usually a ground truth measurement is used to obtain such quantities at a forest site of interest. The mean and standard deviation of each measured parameter are then collected and stored in an input file. Such an input file, together with the DNA file, is then read by a computer program which decodes the fractal growing scheme and generates the tree trunk, branches, stems, and leaves with a random sample value of each structural parameter. Therefore the random nature of the tree structure is embodied through these random values. The PDF of each parameter is generally presumed to be a simple function, such as a normal distribution. Besides the tree structural parameters, forest parameters such as the tree density, and dielectric property parameters such as the moisture content of branches and leaves are also provided in an input file.

The accuracy of the ground truth measurement data obviously impacts the fidelity of the reconstructed fractal trees, however some parameters such as branching angle and branch forward step distances are difficult to measure accurately. Additionally, the DNA coding scheme usually starts with the general definition for the whole species, not the specific trees at the site of interest. Therefore a trial-and-error approach is adopted to adjust both the scheme and parameter values. Due to the large number of tree components, it is difficult to examine the accuracy by manual inspection of their dimensions and locations. Instead, visual inspection of the tree image provides a better way. For example, how branchy the tree is can be easily judged from the image of a defoliated fractal tree. Such a visualization program is also developed in [14].

2.3 Wave Scattering Computation Using DBA

The approach of wave propagation computation in FCSM is based on the distorted Born approximation (DBA). In this method scatterers, such as branches and leaves, inside the forest are assumed to be illuminated by the coherent mean-field propagating in an effective medium composed of air and vegetation. The scattered fields from each individual scatterer also propagate in the effective medium towards the receiver and are added coherently. The propagation constant of the mean-field is estimated by Foldy's approximation [16, 24]. The mean-field experiences exponential attenuation and additional phase shift due to the complex nature of the effective dielectric constant of the air-vegetation mixture. In terms of the scattered field computation, DBA is essentially a single-scattering approach. And the widely-used formula of Foldy's approximation is also based on the scattering of individual scatterers. Such a simplification reduces the computational complexity drastically, since multiple-scattering among branches and leaves is ignored.

Commonly the scatterers inside a forest are modeled as dielectric objects of dif-

ferent geometries. For example, tree trunk, branches and stems, as well as needle-like leaves of coniferous trees are treated as dielectric cylinders with finite length, while broad leaves of deciduous trees are approximated as thin dielectric disks of round, elliptical, or other arbitrary-shape boundaries. Scattering formulations of these single scatterers, whether based on low-frequency or high-frequency approximation techniques or exact eigen-series solution for infinite length objects, are thoroughly studied and implemented in literature [4, 18, 40, 41, 42] and hence will not be presented here. More accurate solutions including a full-wave solution using MoM (Method of Moments) can also be found in [23]. With these well-developed scattering formulae, one can first estimate the propagation constant of the effective forest medium, M_{pq}, according to Foldy's approximation

$$M_{pq} = \frac{j2\pi n}{k_0}\langle S_{pq}\rangle \tag{2.1}$$

where $j = \sqrt{-1}$, n is the number of scatterers per unit volume and k_0 is the free space wave number. S_{pq} is the forward scattering amplitude of a single scatterer, given by

$$\bar{E}_p^s = \frac{e^{jk_0R}}{R} S_{pq} \cdot \bar{E}_q^i \tag{2.2}$$

where $\bar{E}_q^i$, $\bar{E}_p^s$ are incident and scattered fields with polarizations q and p respectively, and R is the distance from the scatterer to the receiver which detects the scattered field. The operator $\langle\ \rangle$ in (2.1) represents the ensemble average of the forward scattering amplitude (S_{pq}) of all the scatterers inside the unit volume. Practically, each M_{pq} is calculated by computing the summation of S_{pq} of all scatterers inside a specified volume and then normalized by the occupying volume. Due to the inhomogeneous nature of tree structures along the vertical direction, the forest can be divided into a number of horizontal layers, for which M_{pq} are different depending on the constituents and the respective geometry and volume function [14]. The scheme of dividing lay-

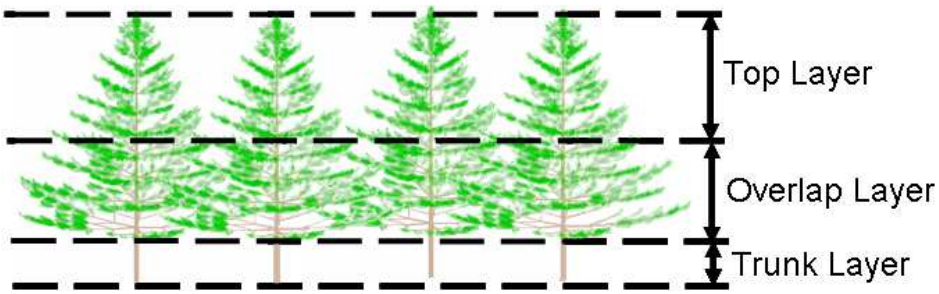

Figure 2.3: Layer division of a red pine stand.

ers vertically results from a trade-off between accuracy and simplicity. Usually for coniferous trees, the forest block is divided into three layers, i.e. the trunk layer, the overlap layer, and the top layer, as shown in Figure 2.3 for a red pine stand. The distinction between the overlap and top layers is due to the overlapping of conical structures of the neighboring tree crowns. For deciduous trees the division of the tree crown has no specific rules and can be customized according to the specific tree and stand structure as well as the accuracy requirement of the application.

Next the scattered field from each individual scatterer to the receiver is calculated using the above-mentioned scattering formulations, with both incident and scattered field modified by Foldy's propagation constant compared to their free-space counterparts, i.e.

$$\mathbf{E} = \mathbf{T} \cdot \mathbf{E_0} \tag{2.3}$$

where

$$\mathbf{E} = \begin{pmatrix} E^v \\ E^h \end{pmatrix}, \quad \mathbf{E_0} = \begin{pmatrix} E_0^v \\ E_0^h \end{pmatrix} \tag{2.4}$$

and

$$\mathbf{T} = \begin{pmatrix} e^{jM_{vv}R} & 0 \\ 0 & e^{jM_{hh}R} \end{pmatrix}. \tag{2.5}$$

$\mathbf{E}$ and $\mathbf{E_0}$ represent polarized electric field vectors of the radio wave propagating inside the effective forest medium and inside free space, respectively. The superscript v and

h stand for vertical and horizontal polarizations. $\mathbf{T}$ is the transmissivity matrix of the effective medium with Foldy's propagation constant M_{vv} and M_{hh}, and R being the distance that the incident wave travels upon hitting the scatterer or the scattered wave travels before arriving at the receiver. It is worth mentioning that in most natural structures such as a forest, azimuthal symmetry can be assumed and hence the averaged transmissivity of depolarized components is approximately zero, that is $M_{vh} \simeq 0$, $M_{hv} \simeq 0$.

Another important feature of wave propagation computation in FCSM is the ground effect. As shown in Figure 2.4, four different wave propagation mechanisms exist inside a forested environment, where $\vec{E}_d$, $\vec{E}_{tg}$, $\vec{E}_{gt}$ and $\vec{E}_{gtg}$ stand for the direct scattered field with the scatterer illuminated by the direct incident wave, the reflected scattered field with the scatterer illuminated by the direct incident wave, the direct scattered field with the scatterer illuminated by the reflected incident wave, and the reflected scattered field with the scatterer illuminated by the reflected incident wave, respectively. The ground effect is accounted for by using the GO (Geometric Optics) method, with the Fresnel reflection coefficients modified by Kirchhoff's approximation [16] to take into account the ground surface roughness. Alternatively, image theory can be applied where the approximate image current under the ground can be derived to compute the reflected scattered field [18].

A subtle point in implementing the scattered field computation lies in the fact that the available formulations of scattering from a single scatterer usually depend on the polarization of the incident and scattered waves. And such a polarization is defined as $\hat{v}$ (vertical polarization) or $\hat{h}$ (horizontal polarization), where

$$\hat{h} = \frac{\hat{z} \times \hat{k}}{|\hat{z} \times \hat{k}|} \tag{2.6}$$

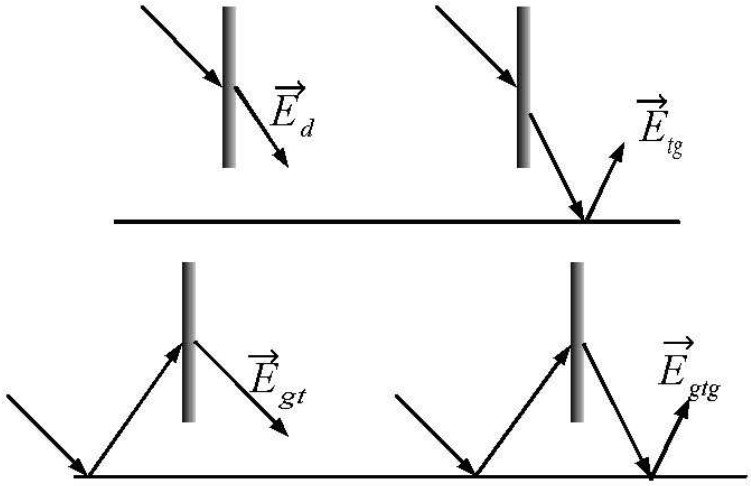

Figure 2.4: Components of scattered field from a scatterer above ground plane corresponding to four wave propagation scenarios: direct-direct, direct-reflected, reflected-direct, and reflected-reflected.

and

$$\hat{v} = \hat{h} \times \hat{k} \tag{2.7}$$

with $\hat{k}$, $\hat{z}$ being unit vectors of the direction of incident or scattered wave and the z-direction, respectively. All these unit vectors are defined in the local coordinates of the scatterer which could be different from the global coordinates of the real environment, since these scatterers all have their specific orientations. In this case, coordinate transformation has to be performed frequently, that is, one first transforms the incident wave from global to local, then computes the scattered field, and at the end transforms the scattered field back from local to global [18]. In some special cases where the scattering formulation can be modified to a new version that can be applied directly in the global coordinates, the coordinate transformation process is minimized and hence computation time is reduced. Calculating the scattered field from a cluster of pine needles is such an example (see Appendix A).

Once the scattered field at the receiver from all scatterers are computed, they are coherently added to obtain the total scattered field. This is in fact only one

random sample. In order to estimate the wave propagation behavior statistics, the Monte-Carlo simulation technique is employed where the above forest-reconstruction and scattering computation are repeated for many "realizations". At each realization, the structural parameters of the forest are varied randomly according to their prescribe PDFs, resulting in a random sample of the forested environment. The required number of realizations can be determined by standard convergence verification techniques.

2.4 Applications & Limitations of FCSM

Figure 2.5 illustrates various scenarios to which FCSM can be applied directly. Originally FCSM was developed for the purpose of interpreting the radar backscatter of a forest and extracting the desired botanical parameters such as the biomass and average tree height [17, 43]. For such applications (corresponding to a satellite or aircraft above the forest), both the transmitter and receiver are outside the foliage and in the far-field region of the foliage scatterers. In this case plane wave illumination can be assumed where the wave enters the foliage through a diffuse top boundary and gets scattered back by scatterers inside the forest as well as the ground or the interaction between these two [14]. Another scenario of interest is the problem of camouflaged targets under foliage. In this case the hard targets are in the near-field region of the scatterers. An additional scenario of similar arrangement is communication to a point (transmitter or receiver) inside the forest from an aircraft or satellite above the foliage. For example, to assess the performance of GPS receivers under foliage, or to design a satellite radio link such a scenario is encountered. This wave propagation scenario is similar to the previous one in that a plane wave still illuminates the foliage. Instead of computing the backscatter field, however, the scattered field at the receiver location will be calculated. The reciprocity theorem can be applied for the case of a transmitter sending electromagnetic waves to a target far beyond the canopy

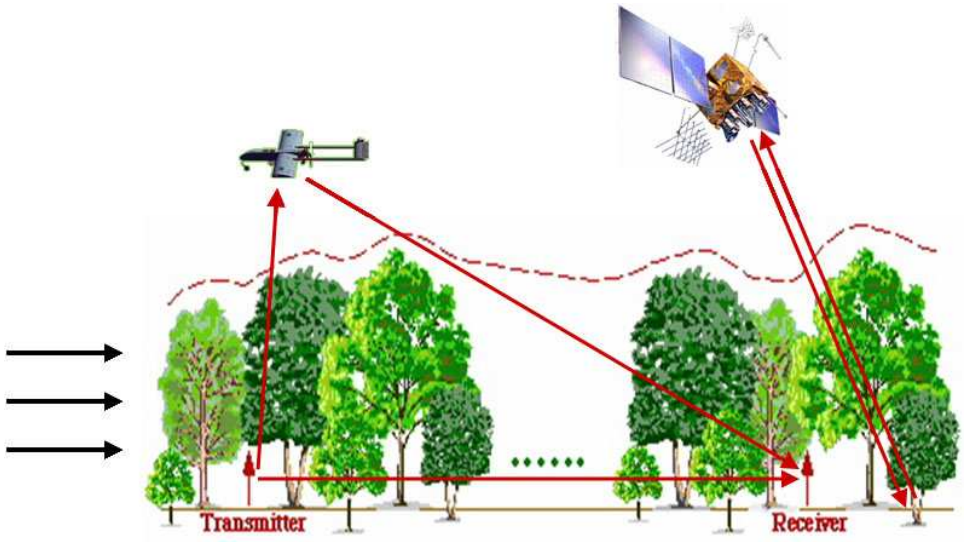

Figure 2.5: Wave propagation scenarios of different applications where FCSM can be applied.

top. Wireless communications between a transmitter and a receiver both inside the forest are also of importance especially for military applications. In this case, a spherical wave has to be considered instead of plane wave propagation, and again the transmitter and receiver may be in the near-field region of the scatterers. One more application is to estimate the foliage path-loss for a horizontally propagating wave through the foliage. This wave propagation scenario can be considered as a plane wave illuminating the forest from its edge, as shown in Figure 2.5.

There are several limitations associated with FCSM though. The Foldy's approximation used in FCSM applies only for a sparse medium, since it assumes independent scatterers in the medium. This results in a single-scattering approximation for computing the average forward scattering amplitude in 2.1. Such an approximation is reasonable for the frequency bands where multiple-scattering effects are negligible. However, at upper microwave and millimeter-wave frequencies, where the size of densely packed particles becomes larger or comparable with the wavelength, the single-scattering model is not sufficient. Basically near-field interactions between scatterers, such as those within a dense leaf cluster, influence the value of the forward

scattering amplitude which determines the attenuation rate of the coherent mean-field through the foliage. Such an effect has to be taken into account if the accuracy of FCSM is to be enhanced at high frequencies. Some intensive numerical techniques, such as MoM, may be needed to provide the exact full-wave solution.

The second limitation of FCSM is again related to the multiple-scattering effect, and this time it is the multiple-scattering components in the scattered field at the receiver that attract the attention. As described earlier, the DBA technique employed by FCSM is essentially a single-scattering method, although the effective medium accounts for scatterers along the wave propagation path in an average sense. For highly scattering environments or long propagation distances, multiple-scattering components involving two or more discrete scatterers become important and must be accounted for, although the computational complexity may be increased drastically. The third limitation of FCSM corresponds to a particular kind of application where the propagation distance inside a forest is very large, such as when estimating foliage path-loss. Direct application of FCSM over long distances would require computation of scattering from many scatterers which is practically impossible. Smarter approaches and algorithms have to be developed to overcome or circumvent such limitations.

Finally the applicability of FCSM is limited to users with in-depth knowledge of the wave propagation model which consists of thousands of lines of computer codes. Without a user-friendly interface and powerful computers for running simulations, such a model is not easy to use. Therefore it is of great interest to develop some simple-to-use formulae based on the simulation results using FCSM. In other words, just like conducting real experiments and extracting an empirical model from the measured data, one essentially runs numerical "experiments" with FCSM on computers and develops a macro-model from the simulated data.

CHAPTER 3

AN ENHANCED MILLIMETER-WAVE FOLIAGE PROPAGATION MODEL

3.1 Introduction

The demand for high data rate wireless communication is on the rise in recent years. People enjoy exchanging photos or even videos through their cell phone or laptop, satellites in space transmit more and more valuable data and images back to Earth frequently, etc. For this purpose wideband communication at millimeter-wave frequencies is under consideration for various applications. Forested environments pose a significant challenge for the operation of such systems. In order to assess the performance of communication devices operating at high frequencies, characteristics of the communication channel such as path-loss, coherence bandwidth, fading statistics, etc., must be determined. This requires an accurate electromagnetic model to predict the wave propagation behavior inside forested environments.

The fractal-based coherent scattering model (FCSM) described in the previous chapter has proven to be one of the most accurate models for foliage wave propagation. However, the Foldy's approximation used in FCSM assumes scatterers are independently interacting with the propagating wave and have no mutual coupling, resulting in a single-scattering formulation for estimating the Foldy's propagation constants. Such an approximation is reasonable for sparse media where scatterers are

far apart, or for frequency bands where multiple-scattering effects are negligible. At upper microwave and millimeter-wave frequencies, where the size of densely packed particles becomes larger or comparable with the wavelength, the single-scattering formulation is not sufficient. It has been shown that neglecting near-field mutual coupling, such as those that occur within a dense leaf cluster, tends to overestimate the attenuation rate of the effective forest medium at millimeter-wave frequencies [23].

In this chapter, in order to overcome such a limitation, the multiple-scattering that occurs among leaves of highly dense leaf clusters is included in the wave propagation model. Other constituents of the forest, such as branches and trunks, however, are distributed sparsely and single-scattering is still applicable for them. A full-wave numerical technique, MoM (Method of Moments) [44], is used to calculate the exact scattering from a cluster of leaves or needles exactly. However, this technique requires significant computational resources which prohibit its direct application in the wave propagation model. Therefore a computationally efficient technique is presented. For a semi-random cluster of pine needles the scattered field remains coherent only in the forward direction and a small angular range near the forward direction, which depends on the size of the cluster relative to the wavelength. To calculate the coherent field, the distorted Born approximation (DBA) is applied to an inhomogeneous, anisotropic dielectric object having the same boundary as the needle cluster. The scattered field outside the forward scattering cone has a random phase with almost uniform scattered power. In situations where a clear boundary between leaf clusters and the surrounding air cannot be recognized, such as those of deciduous trees, this technique is not applicable. However, for those leaf clusters where broad leaves are relatively sparse, the effect of multiple-scattering is not as significant.

To examine the accuracy of the enhanced wave propagation model, an outdoor measurement through a pine tree stand was conducted at Ka-band (35 GHz). Sim-

ulation results using the single-scattering model (FCSM) and the multiple-scattering model (the enhanced model) are compared with the measured result, and the importance of the latter is clearly justified.

3.2 Multiple-Scattering Effects from Needle Clusters

In this section a MoM solution for calculating the scattered field from red pine needle clusters is presented and compared with the single-scattering solution to investigate multiple-scattering effects. The computational requirements are also examined to justify the need for developing a macro-model for the cluster. Since the macro-model encapsulates the effect of many needles (e.g. $\sim$100), the computation time for the propagation model can be greatly reduced.

A red pine needle cluster has its needle buds distributed as three concentric spirals around a small stem. Needles come off of the stem at an angle which will be referred to as the tilt angle. There are two kinds of clusters on coniferous trees, the end-cluster and the stem-cluster. For the end-cluster, the tilt angle decreases as the needle bud approaches the tip of the stem. For the stem-cluster, the tilt angles are the same for each needle. The distance between each pair of needles can be as small as 5 mm, less than half a wavelength at 35 GHz, and the needle length can vary from 1 cm to 10 cm, which is much larger than a wavelength. In this case mutual coupling among needles may be significant. Based on a ground truth measurement for the red pine stand used in the path-loss measurement, the end-cluster and the stem-cluster (see Figure 3.1) were measured to have an average of 96 and 117 needles, respectively. The average needle length and diameter for this pine tree were measured to be 3.5 cm and 0.45 mm respectively.

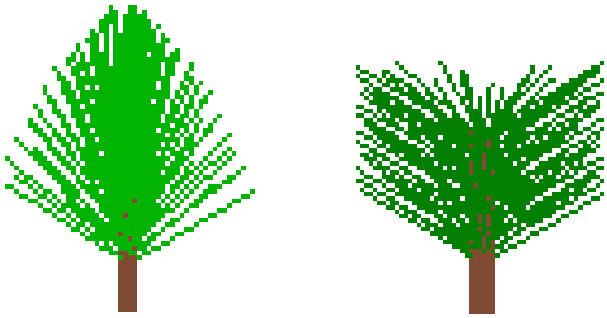

(a) (b)

Figure 3.1: The needle cluster structures: (a) end-cluster, (b) stem-cluster.

3.2.1 MOM Formulation

In this specific application of MoM for needle clusters, pulse basis functions (constant current across each cell), point matching for weighting functions, along with the volume equivalence principle, are assumed in the formulation [44]. For the time being, the stem is excluded. The volumetric integral equation for the MoM formulation is given by

$$\bar{E}_s(\bar{r}_m) + \bar{E}_i(\bar{r}_m) = \bar{E}(\bar{r}_m) = \frac{\bar{J}_{eq}(\bar{r}_m)}{-j\omega\epsilon_0(\epsilon_r - 1)} \tag{3.1}$$

and

$$\bar{E}_s(\bar{r}_m) = \iiint_V j\omega\mu_0 \overline{\overline{G}}(\bar{r}_m, \bar{r}') \cdot \bar{J}_{eq}(\bar{r}')dV' \tag{3.2}$$

where subscripts s and i indicate the scattered and incident field, respectively, and the right side of (3.1) is an equivalent volumetric current. Also $\bar{r}_m$ is the center position of the m^{th} cell, $\overline{\overline{G}}(\bar{r}_m, \bar{r}')$ is the free space electric dyadic Green's function which indicates the electric field at $\bar{r}_m$ generated by a point current source at $\bar{r}'$ and is given by

$$\overline{\overline{G}}(\bar{r}_m, \bar{r}') = \left(\overline{\overline{I}} + \frac{\nabla\nabla}{k_0^2}\right)\frac{e^{jk_0R}}{4\pi R} \tag{3.3}$$

where $\overline{\overline{I}}$ is the unit dyadic and R is the distance between $\bar{r}_m$ and $\bar{r}'$ which is $|\bar{r}_m - \bar{r}'|$. Substituting (3.2) into (3.1), one obtains

$$\bar{E}_i(\bar{r}_m) = \frac{\bar{J}_{eq}(\bar{r}_m)}{-j\omega\epsilon_0(\epsilon_r - 1)} - \iiint_V j\omega\mu_0 \overline{\overline{G}}(\bar{r}_m, \bar{r}') \cdot \bar{J}_{eq}(\bar{r}')dV'. \tag{3.4}$$

Discretizing this equation using a total of N cells for all the needles, a $3N \times 3N$ matrix equation is obtained as

$$\begin{pmatrix} E_i^x \\ E_i^y \\ E_i^z \end{pmatrix} = \begin{pmatrix} Z_{xx} & Z_{xy} & Z_{xz} \\ Z_{yx} & Z_{yy} & Z_{yz} \\ Z_{zx} & Z_{zy} & Z_{zz} \end{pmatrix} \begin{pmatrix} J_{eq}^x \\ J_{eq}^y \\ J_{eq}^z \end{pmatrix} \tag{3.5}$$

which can be solved for the unknown current coefficient J_{eq} in each cell. Notice that each matrix or vector component in (3.5) represents the quantity for N cells. The matrix of 3×3 components is defined as the impedance or Z-matrix and given by

$$\overline{\overline{Z}}(\bar{r}_m) = \frac{\overline{\overline{I}}}{-j\omega\epsilon_0(\epsilon_r - 1)} - \iiint_V j\omega\mu_0 \overline{\overline{G}}(\bar{r}_m, \bar{r}')dV'. \tag{3.6}$$

Equation (3.5) cannot be decomposed in the normal fashion into TM and TE incident fields in order to reduce the number of unknowns as each needle is oriented at a different angle so that a TM or TE incident wave only has meaning in the local coordinates of one single needle. Instead, this problem is directly solved in the coordinates of the whole cluster without decomposition, where the needle cluster stem is assumed to be oriented along the z-axis. The Z-matrix is independent of the incident field and hence need only be calculated and inverted once to compute the unknown currents for different excitations, i.e.

$$\bar{J}_{eq} = \overline{\overline{Z}}^{-1} \bar{E}_i. \tag{3.7}$$

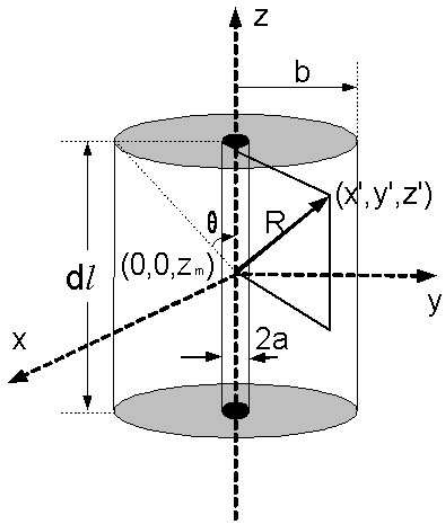

Figure 3.2: Self-cell configuration.

Therefore $\overline{\overline{Z}}^{-1}$ can be reused for clusters with various orientations in the foliage. Note that according to the reciprocity theorem, the Z-matrix is symmetric. Therefore, the number of elements requiring storage is reduced from $3N \times 3N$ to $3N \times (3N+1)/2$. To obtain $\overline{\overline{Z}}^{-1}$, (3.5) should be solved directly, which requires significant computer memory. In order to evaluate the Z-matrix in an efficient fashion, the self-cell, the adjacent cells in the same needle, and the adjacent cells in different needles are treated in different ways.

Self-cell

Due to the singularity of the electric dyadic Green's function in the source region, the impedance matrix of self-cells must be evaluated in an alternate way. A source dyadic $\overline{\overline{L}}$ is introduced according to [45]. As seen in Figure 3.2, a self-cell, with b the radius of its transverse cross-section and dl the length, is divided into two parts, an infinitesimally thin cylinder (radius of the transverse cross-section, a, approaching zero) along the z-axis of the cell and the remainder of the volume. The contribution

from the infinitesimally thin cylinder is given by $-\overline{\overline{L}}/(j\omega\epsilon_0)$ where [45]

$$\overline{\overline{L}} = \begin{pmatrix} 1/2 & 0 & 0 \\ 0 & 1/2 & 0 \\ 0 & 0 & 0 \end{pmatrix}. \tag{3.8}$$

The remainder is calculated by applying the principal value integral

$$\lim_{a\to 0} \iiint_V j\omega\mu_0 \overline{\overline{G}}(\bar{r}_m, \bar{r}')dV', \tag{3.9}$$

where V stands for the volume of the self-cell excluding the infinitesimally thin cylinder. According to (3.3), two integrals need to be evaluated:

$$I_1 = \lim_{a\to 0} \iiint_V \frac{e^{jk_0R}}{R} dV' \tag{3.10}$$

and

$$\overline{\overline{I_2}} = \lim_{a\to 0} \iiint_V \nabla\nabla \frac{e^{jk_0R}}{R} dV', \tag{3.11}$$

where $R = \sqrt{x'^2 + y'^2 + (z' - z_m)^2} = \sqrt{\rho'^2 + (z' - z_m)^2}$.

Since each cell is electrically small ($k_0R << 1$), (3.10) can be expanded using the first 2 terms of a Taylor series, i.e.

$$I_1 \simeq \lim_{a\to 0} \iiint_V \left(\frac{1}{R} + jk_0\right) dV', \tag{3.12}$$

which simplifies to

$$I_1 \simeq jk_0\Delta V + 2\pi \left[\frac{dl}{2}\sqrt{b^2 + \left(\frac{dl}{2}\right)^2} + b^2 \ln\left(\frac{dl/2 + \sqrt{b^2 + (dl/2)^2}}{b}\right) - \left(\frac{dl}{2}\right)^2\right] \tag{3.13}$$

where $\Delta V = \pi b^2 dl$ is the volume of the cell. To evaluate (3.11), one can first evaluate

$$I_3 = \lim_{a\to 0} \iiint_V \frac{\partial^2}{\partial z^2} \frac{e^{jk_0 R}}{R} dV' = \lim_{a\to 0} -\frac{\partial}{\partial z} \iiint_V \frac{\partial}{\partial z'} \frac{e^{jk_0 R}}{R} dV', \tag{3.14}$$

where the identity $\frac{\partial}{\partial z}\frac{e^{jk_0 R}}{R} = -\frac{\partial}{\partial z'}\frac{e^{jk_0 R}}{R}$ is applied. By integrating over z' on of the partial derivatives, $\frac{\partial}{\partial z'}$ in (3.14) is eliminated. Evaluation of the remaining integral and then evaluation of the second partial derivative in (3.14) gives

$$I_3 = 4\pi \left[e^{jk_0\sqrt{b^2+(dl/2)^2}} \frac{dl/2}{\sqrt{b^2+(dl/2)^2}} - e^{jk_0 dl/2} \right]. \tag{3.15}$$

The other two diagonal elements are difficult to evaluate directly. However, they can be evaluated alternatively according to the Helmholtz equation

$$\iiint_V (\frac{\partial^2}{\partial x^2} + \frac{\partial^2}{\partial y^2} + \frac{\partial^2}{\partial z^2} + {k_0}^2) \frac{e^{jk_0 R}}{R} dV' = 0, \tag{3.16}$$

since the integration is performed over a source-free region (the source point is inside the infinitesmally thin cylinder and has been excluded). In addition, it can be noticed that there is no difference between the integration with respect to x and y. Therefore, one obtains

$$I_4 = \iiint_V \frac{\partial^2}{\partial x^2} \frac{e^{jk_0 R}}{R} dV' = \iiint_V \frac{\partial^2}{\partial y^2} \frac{e^{jk_0 R}}{R} dV' = -\frac{1}{2}(I_3 + {k_0}^2 I_1) \tag{3.17}$$

The off-diagonal elements of $\overline{\overline{I_2}}$ are equal to zero since the cell is symmetric about the z-axis.

An alternative way to evaluate the self-cell is to treat the whole cell as the source

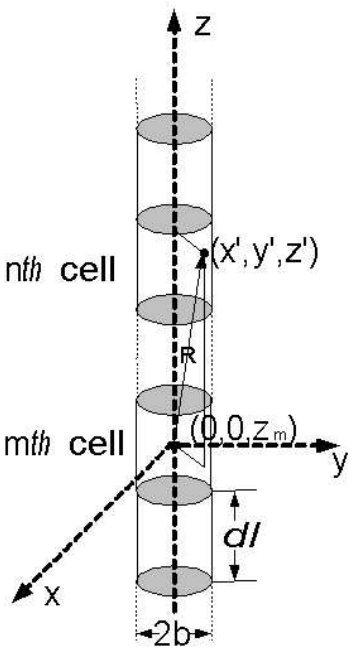

Figure 3.3: Configuration of two adjacent cells in the same needle.

region which contributes as a source dyadic [45]

$$\overline{\overline{L}} = \begin{pmatrix} \frac{1}{2}\cos\theta & 0 & 0 \\ 0 & \frac{1}{2}\cos\theta & 0 \\ 0 & 0 & 1-\cos\theta \end{pmatrix}. \tag{3.18}$$

Provided that the dimensions of the self-cell are small enough, this approach can give similar results to that given by the previous method.

Adjacent Cells in a Single Needle

Figure 3.3 shows the individual cells in a single needle. The electric field at the center of the m^{th} cell generated by the n^{th} cell is calculated by evaluating similar integrals as for the self-sell. The difference lies in that for this case the observation point (center of the m^{th} cell) is out of the integration region (the n^{th} cell), therefore no singularity occurs. Also for the integral $I_5 = \iiint \frac{e^{jk_0R}}{R} dV'$, the approximation used

in (3.12) is not suitable due to the relatively large distance between the two cells. Instead, I_5 is evaluated as the following

$$\begin{aligned} I_5 &= \int_{-dl/2}^{dl/2}\int_0^{2\pi}\int_0^b \frac{e^{jk_0R}}{R}\rho' d\rho' d\phi' dz' \\ &= \frac{2\pi}{jk_0}\int_{-dl/2}^{dl/2}(e^{jk_0\sqrt{b^2+(z_m-z_n-z')^2}} - e^{jk_0\sqrt{(z_m-z_n-z')^2}})dz', \end{aligned} \tag{3.19}$$

where z_m, z_n are the z-coordinates of the m^{th} and n^{th} cell, respectively. The evaluation of integral $\int_{-dl/2}^{dl/2} e^{jk_0\sqrt{b^2+(z_m-z_n-z')^2}}dz'$ can be approximated by expanding the integrand into a Taylor series up to the cubic term.

The evaluation of the elements of $\overline{\overline{I_6}} = \iint\int \nabla\nabla\frac{e^{jk_0R}}{R}dV'$ are performed the same way as evaluating $\overline{\overline{I_2}}$. First, we compute

$$\begin{aligned} I_7 =& \iint\int_{\text{nth cell}} \frac{\partial^2}{\partial z^2}\ \frac{e^{jk_0R}}{R}dV' = -\frac{\partial}{\partial z}\int_0^{2\pi}\int_0^b\int_{-dl/2}^{dl/2}\frac{\partial}{\partial z'}\frac{e^{jk_0R}}{R}dz'\rho' d\rho' d\phi' \\ =& -2\pi\Bigg[e^{jk_0\sqrt{b^2+(z_m-z_1)^2}}\frac{z_m-z_1}{\sqrt{b^2+(z_m-z_1)^2}} - e^{jk_0(z_m-z_1)} \\ & -e^{jk_0\sqrt{b^2+(z_m-z_2)^2}}\frac{z_m-z_2}{\sqrt{b^2+(z_m-z_2)^2}} + e^{jk_0(z_m-z_2)}\Bigg]. \end{aligned} \tag{3.20}$$

where $z_1 = z_n + dl/2, z_2 = z_n - dl/2$. The other two diagonal elements are computed similarly to that for the self-cell (see (3.16) and (3.17)). Again, the off-diagonal elements equal zero due to the symmetry of the cylinder.

The integrals above, including that for the self-cell, are evaluated in the local coordinates of a single needle. When modeling the whole needle cluster, global coordinates of the cluster must be used. A coordinate transformation matrix [18] is employed to transform the impedance matrix from each needle's local coordinates to the global coordinates.

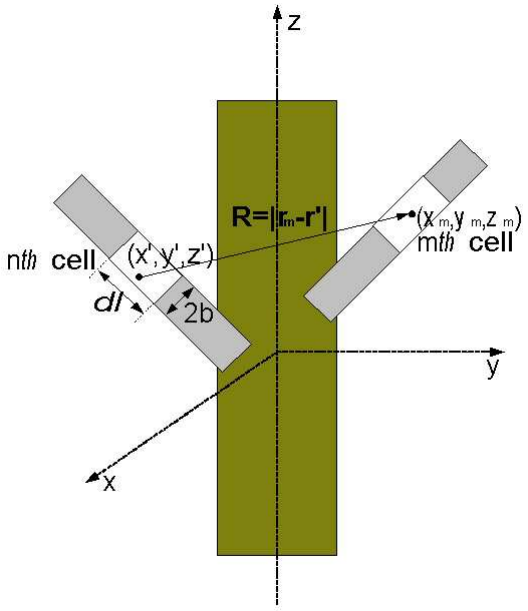

Figure 3.4: Configuration of two adjacent cells in different needles.

Cells in Different Needles

Evaluating individual cells in different needles (Figure 3.4) is more difficult as they are not oriented identically. Performing a coordinate transformation for each needle will greatly increase the problem complexity. In addition, those volume integrals in (3.19) and (3.20) are difficult to evaluate in this case since the two cells are not coaxial. However, due to the relatively far distance between these two cells, it is possible to make the following mid-point approximation [46]

$$\iiint_{\text{nth cell}} j\omega\mu_0 \overline{\overline{G}}(\bar{r}_m, \bar{r}')dV' \simeq \Delta V j\omega\mu_0 \overline{\overline{G}}(\bar{r}_m, \bar{r}_n). \tag{3.21}$$

The elements of $\overline{\overline{G}}(\bar{r}_m, \bar{r}_n)$ are given by

$$G^{mn}_{x_p x_q} = \frac{j\omega\mu_0 k_0 \Delta V \exp(j\alpha_{mn})}{4\pi\alpha^3_{mn}} \big[(\alpha^2_{mn} - 1 + j\alpha_{mn})\delta_{pq} + \frac{(x^m_p - x^n_p)(x^m_q - x^n_q)}{R^2_{mn}}(3 - \alpha^2_{mn} - 3j\alpha_{mn})\big], \tag{3.22}$$

where p and q both take on the values 1, 2, and 3, independently, so that they represent the coordinates x, y, and z. Also, $R_{mn} = |\bar{r}_m - \bar{r}_n|$, and $\alpha_{mn} = k_0 R_{mn}$. The Kronecker delta $\delta_{pq} = 0$ if $p \neq q$ and $\delta_{pq} = 1$ if $p = q$. In (3.21), every cell is in the global cluster coordinates and a coordinate transformation is not necessary.

3.2.2 Simulation Results

The above MoM formulation is applied to examine the multiple-scattering from both the end-cluster and stem-cluster in Figure 3.1. For comparison, the single-scattering from needle clusters is also calculated where the scattered field from each single needle is added coherently. Two solutions are employed to compute the scattered field from a single needle. One is based on a low frequency technique, Rayleigh-Gans approximation [40], which is quite simple but not accurate at millimeter-wave frequencies. The other is the semi-exact solution based on the eigen-series solution for scattering from an infinite dielectric cylinder [48], which is accurate but more complicated computationally. Figure 3.5 shows the forward scattering from the end-cluster versus the incident angle θ_i (angle between the stem axis and the incident wave). It is obvious that the Rayleigh-Gans approximation is no longer valid at millimeter-wave frequencies, and the semi-exact single-scattering solution overestimates the forward scattering by an amount as large as 3 dB, compared with the multiple-scattering solution using MoM.

According to Foldy's approximation, the attenuation rate is proportional to the

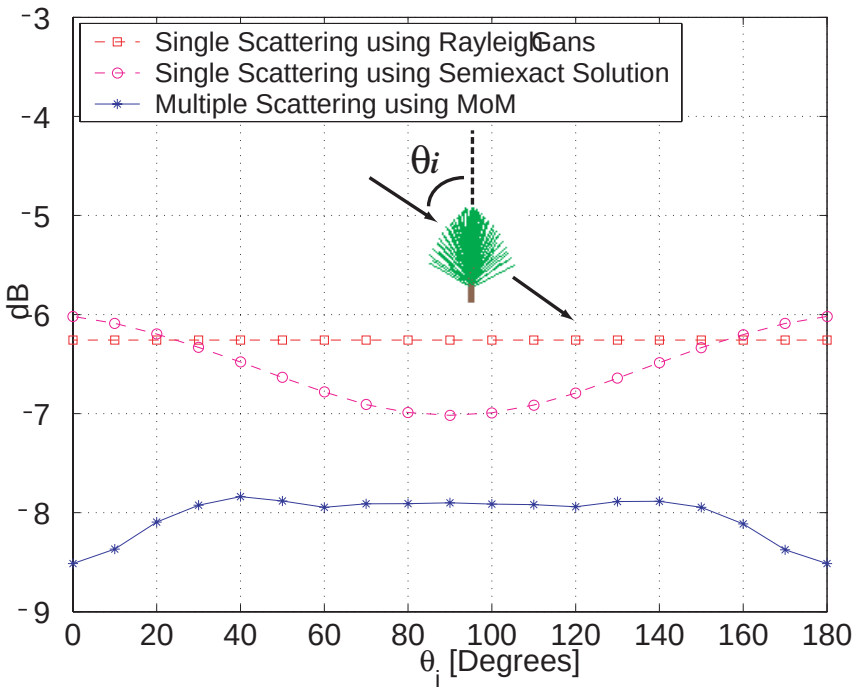

(a)

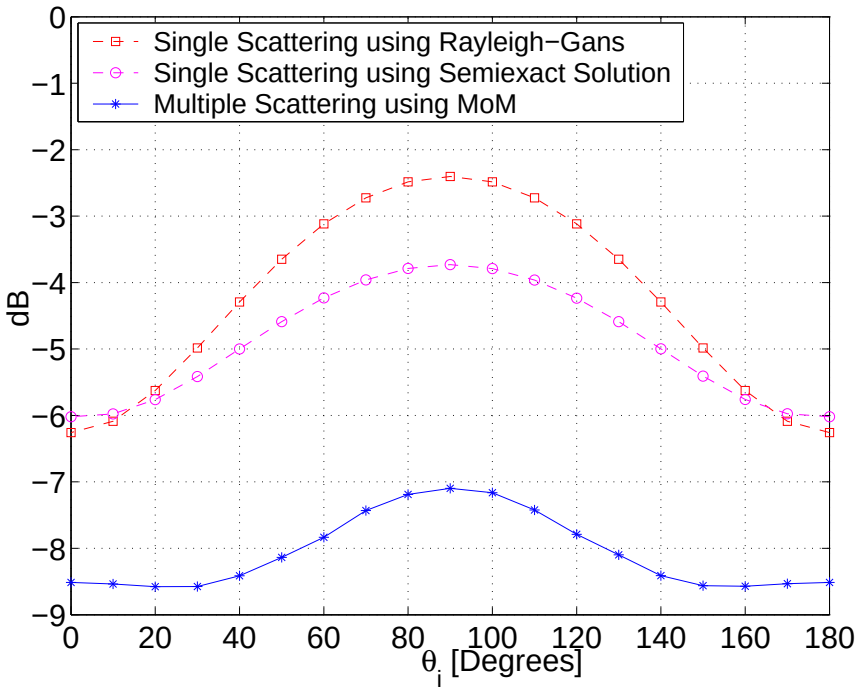

(b)

Figure 3.5: Comparison of forward scattering from an end-cluster: (a) $|S_{hh}|$, (b) $|S_{vv}|$.

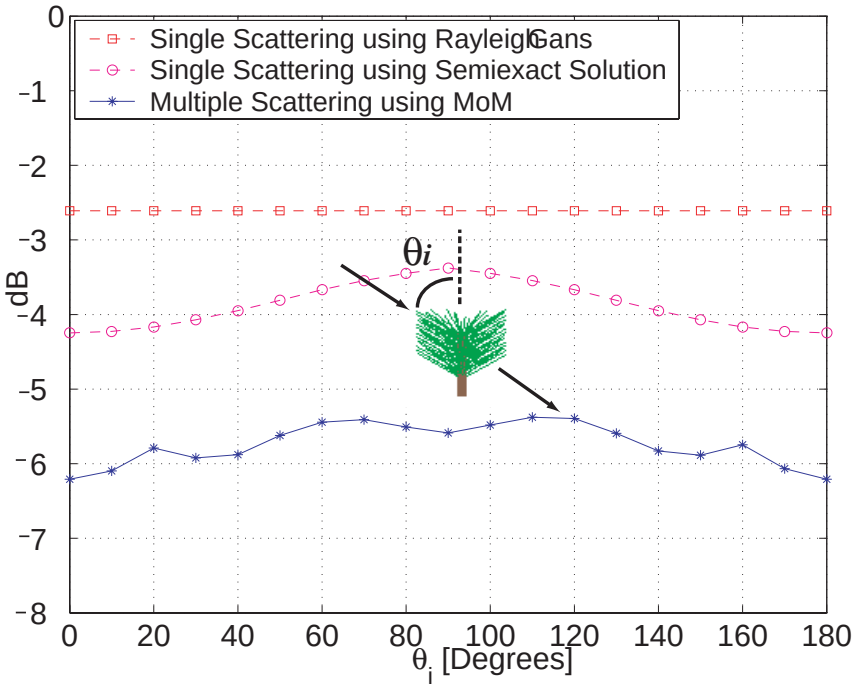

(a)

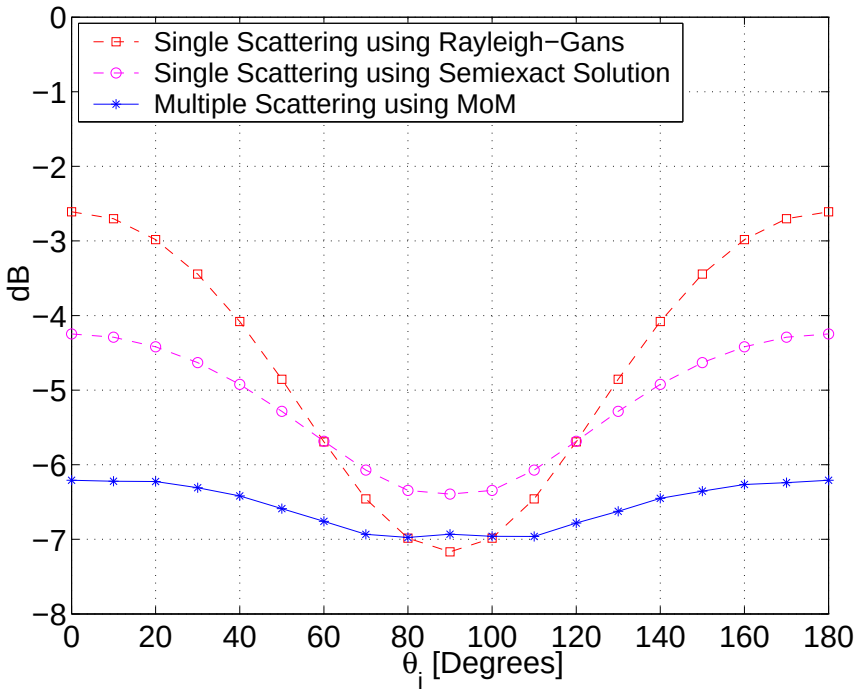

(b)

Figure 3.6: Comparison of forward scattering from a stem-cluster: (a) $|S_{hh}|$, (b) $|S_{vv}|$.

imaginary part of the forward scattering amplitude. Examination of this quantity based on the above simulation shows that using single-scattering theory to calculate scattering from needle clusters will cause a significant overestimation of the attenuation rate which mandates inclusion of the effects of multiple-scattering. That is, if the effects of multiple-scattering are ignored, calculation of the mean-field through the foliage will be erroneous. On the other hand, it is quite challenging to keep track of multiple-scattering in needle clusters, as MoM is computationally intensive. First, the direct inversion of the impedance matrix is required in order to reuse it for clusters with the same structure but different orientation. This poses great challenges on computer memory and speed requirements. For example, at 35 GHz, a typical end-cluster shown in Figure 3.1 requires about 387 MB (megabyte) of memory to store the impedance matrix, and a stem-cluster requires 471 MB. If the number or length of the needles increases, the number of cells (or unknowns) will also increase. To account for variabilities in clusters many such matrices must be stored. Moreover, since the direct inversion algorithm must be employed, and the computation time is proportional to N^3, where N is the number of unknowns, the time for inverting the impedance matrices could be prohibitively long. For instance, it takes about 1 hour to invert a matrix with 6000 unknowns using a Linux machine with a 2.4 GHz processor.

Second, even when the inverse impedance matrices are stored for reuse, the direct usage of the pre-stored matrices is still prohibitive since there are many clusters in one tree, many trees in a forest, and many realizations required by the Monte-Carlo simulation. A better approach is to calculate and pre-store the full bistatic scattering matrix, $S_{mn}(\theta_i, \phi_i, \theta_s, \phi_s)$, where m, n stand for vertical or horizontal polarization, θ_i, ϕ_i and θ_s, ϕ_s represent the incident and scattering angles, respectively. The pre-stored $\overline{\overline{S}}$ can be used as a lookup table which can be searched based on the incident and scattering angles. However to generate $\overline{\overline{S}}$ lookup table for each cluster, more than

1 GB (gigabyte) of memory and 3 hours of computation time are required. Our goal is to find an alternative approach to the aforementioned techniques. A macro-model based on an analytical method and computational results obtained from the MoM is developed.

3.3 Macro-modeling Multiple-scattering from Needle Clusters

In this section, the statistical behavior of scattered field that is important to the development of the macro-model is presented first and then the detailed algorithm using the distorted Born approximation (DBA) to model scattering near the forward direction is described. Finally the comparison between the macro-model results and those obtained from the brute force full-wave numerical simulations are presented.

3.3.1 Statistical Behavior of Scattering from Needle Clusters

For a needle cluster inside a forest canopy, the rotation angle around its central stem is random. Also the position, pitch angle, and length of needles on a stem has a certain degree of randomness. These random parameters are used in a Monte-Carlo simulation of bistatic scattering from needle clusters to study the statistical behavior of the bistatic pattern. Figure 3.7 shows the bistatic scattering pattern of a needle cluster having 96 needles of diameter 0.45 mm, length 3.54 cm, and relative dielectric constant $6.6 + j6.2$ at 35 GHz. The solid line represents the average scattered power and the dashed line represents the power of the averaged field. Outside the forward scattering beam the significant difference between the power of the mean-field and total power indicates that the phase of the scattered field along these directions varies randomly, that is, the field is totally incoherent. In addition, the averaged power in this region is substantially lower than that in the forward direction and has small fluctuation. Therefore, a constant function can be used to approximately model the

average scattered power over the scattering angles outside forward scattering beam. The scattered field in this region can be given a random phase.

Near the forward direction, scattering from all individual scatters are in-phase and therefore the mean-field is strong only in this region. Over the forward scattering beam the total scattered power and the power of the mean-field are identical. This indicates that over this region the scattering is coherent. The accuracy requirement for the macro-model in this region is much more strict since the attenuation rate is directly proportional to the imaginary part of the forward scattering amplitude. To model the mean-field it is sufficient to model scattering from the "average" scatterer. The average scatterer can be viewed as a body of revolution having a surface defined by the envelope of the needles tip as shown in Figure 3.8. Due to the preferred vertical orientation of needles in the cluster and the variation of vegetation volume fraction within the cluster volume, the average scatterer is modeled by an inhomogeneous anisotropic medium. As an initial estimate, using a simple mixing formula [49], the average permittivity of the end and stem-clusters at 35 GHz are calculated to be around $1.16 + j0.18$ and $1.086 + j0.095$, respectively. This effective dielectric constant is not low enough to allow for the application of the Born approximation in the calculation of the bistatic scattered field. However, accounting for the attenuation and phase velocity of the incident wave through the effective dielectric block, i.e. using DBA, the interior field can be estimated and used to calculate the scattered field.

3.3.2 The Distorted Born Approximation

In this section, a general algorithm for the calculation of scattering from an arbitrary dielectric object is described first, then the validity region of such a method is examined by comparing the exact solution for a dielectric sphere with that obtained from DBA. Next, the DBA algorithm is applied to the needle clusters and the

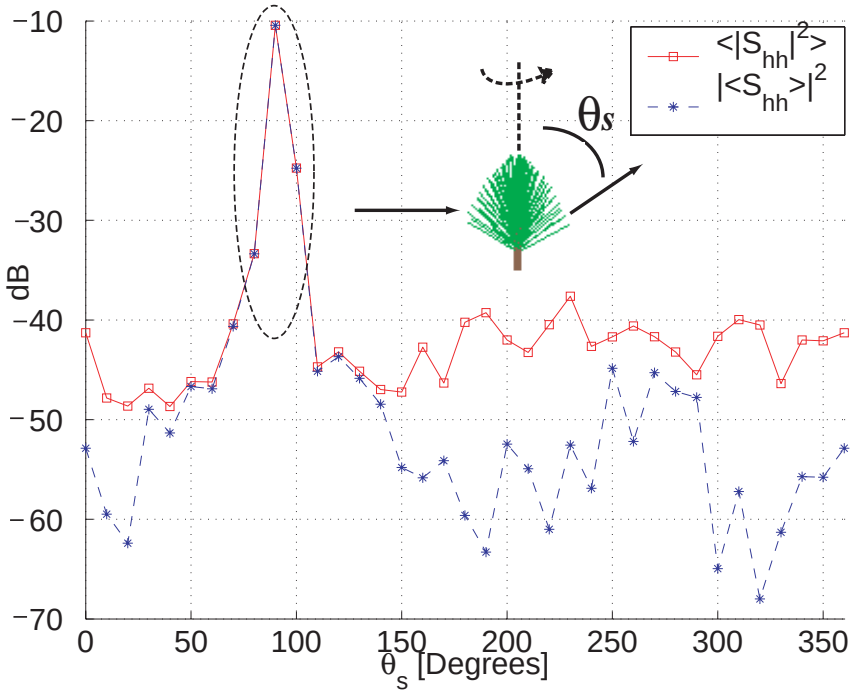

(a)

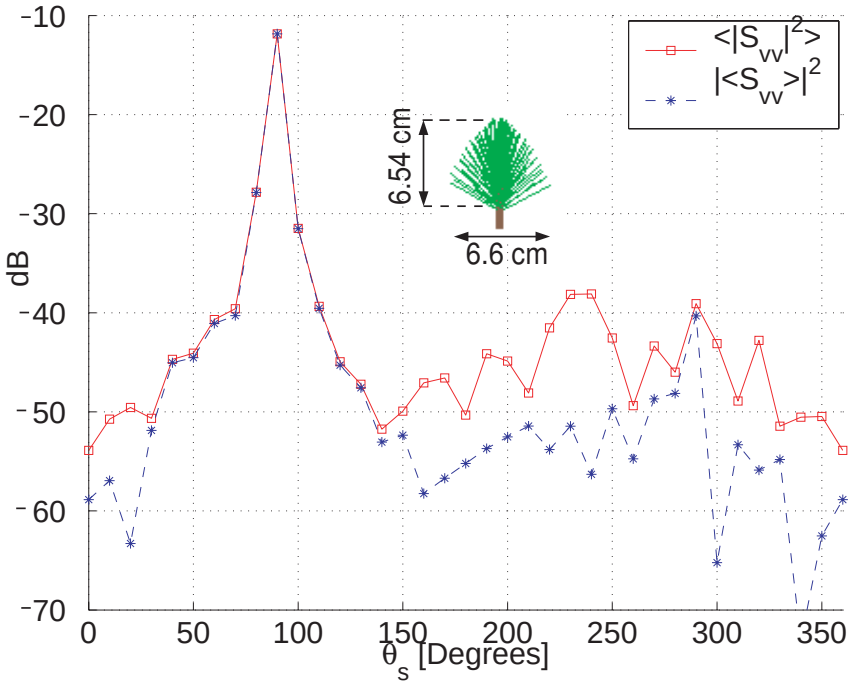

(b)

Figure 3.7: Bistatic scattering from a needle cluster, averaged over the rotation angle around central stem: (a) H-polarization, (b) V-polarization.

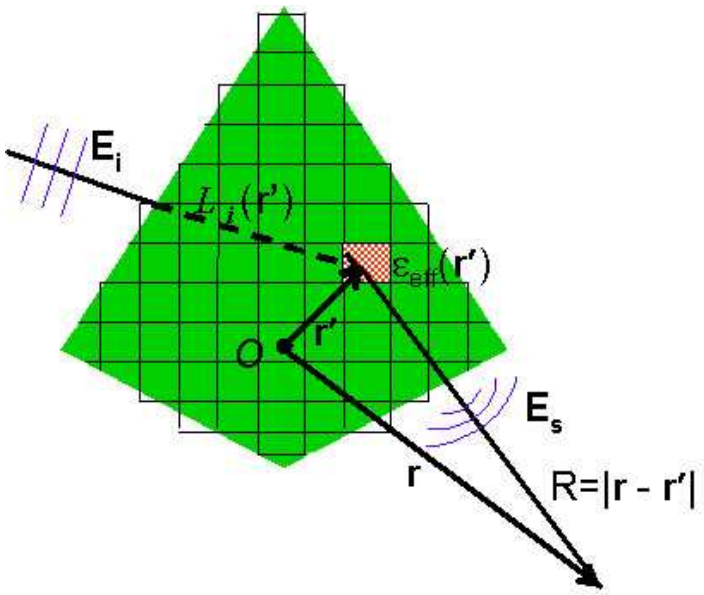

Figure 3.8: Algorithm of Distorted Born Approximation.

simulation results are compared with the MoM solution.

DBA Algorithm

The distorted Born approximation algorithm proposed here has a slightly different implementation from the one employed in FCSM. It is a classic method for computation of the scattered field from dielectric objects whose permittivity is close to that of the surrounding medium. The first step of the proposed DBA algorithm is target discretization and phase change of incident field as shown in Figure 3.8. The interior field of the cell centered at the point $\bar{r'}$, $\bar{E}(\bar{r'})$, is computed by calculating the attenuation and phase change along the path $L_i(\bar{r'})$. The induced polarization currents in each cell are then easily obtained from $\bar{J}_p(\bar{r'}) = -ik_0Y_0(\epsilon - 1)\bar{E}(\bar{r'})$. In this approximation the interior field of the dielectric object is approximated by a field similar to the incident field having the same amplitude and polarization but a different propagation constant. The propagation constant of this field is that intrinsic to the medium the scatterer is made of. Because of its simplicity, DBA can be applied to

scatterers of arbitrary shape and dielectric profile. The scattered field in the far-field region at an observation point $\bar{r}$ is then given by

$$\begin{aligned}\bar{E}_s(\bar{r}) &= j\omega\mu_0 \iiint_V \overline{\overline{G}}(\bar{r},\bar{r}') \cdot \bar{J}_p(\bar{r}')dV' \\ &= \frac{k_0^2}{4\pi} \iiint_V \frac{e^{jk_0R}}{R}(\overline{\overline{I}} - \hat{k}_s\hat{k}_s) \cdot (\overline{\overline{\epsilon}}_{eff}(\bar{r}') - \overline{\overline{I}}) \cdot \bar{E}(\bar{r}')e^{-jk_0\hat{k}_s\cdot\bar{r}'}dV'\end{aligned} \tag{3.23}$$

where $\overline{\overline{G}}$ is the free space dyadic Green's function, R is the distance from the cell center to the observation point, $\hat{k}_s$ is the unit vector along the scattering direction, and $\overline{\overline{I}}$ is the dyadic idemfactor. $\overline{\overline{\epsilon}}_{eff}(\bar{r}')$ represents the effective permittivity tensor of the medium. The attenuation and phase change of the incident field along the path $L_i(\bar{r}')$ can be simply calculated by identifying cells along this path.

Validity Region of DBA

Although the distorted Born approximation is a classic approach, except qualitatively, its region of validity in terms of dielectric contrast and object size is not reported in the literature. The exact Mie-series solution of the scattering from a dielectric sphere is well-known. Figure 3.9(a) and 3.9(b) show the magnitude and phase of the forward scattering as a function of normalized size k_0a (k_0 is the free space wavenumber, a is the radius of the sphere), computed by the DBA algorithm and Mie solution, for a dielectric sphere with $\epsilon_r = 1.5 + j0.5$ at 35 GHz. Very good agreement is shown for spheres as large as $k_0a = 50$. This agreement verifies our correct implementation of DBA and indicates that the DBA algorithm can be applied to needle clusters at millimeter-wave frequencies. Figure 3.10(a) and 3.10(b) show the percentage errors of the magnitude of the forward scattering versus the normalized size (k_0a) and the real part of the relative dielectric constant (ϵ_r') assuming a fixed

loss tangent ($\tan\delta$) of 0.1 and 0.3, respectively. Less than 10%, i.e. 1 dB error for magnitude is achieved for k_0a up to 50 and ϵ_r' up to 2.0 in both cases. A phase error (not shown in Figure 3.10) of less than 3% is achieved as well. It is observed from Figure 3.10a and 3.10b that a null (minimum error) exists in both cases, and above the null, the error increases as k_0a and ϵ_r' increase. The larger the loss tangent, the closer the null is to the bottom-left corner of the figure, and the larger error for the same k_0a and ϵ_r' above the null.

Scattering from Needle Clusters Using DBA

As mentioned earlier needle clusters cannot simply be modeled by a homogeneous isotropic medium. Figure 3.11 shows the surfaces of "the average scatterer" for an end-cluster and a stem-cluster. The end-cluster is approximately a double-cone and the stem-cluster resembles a cylinder with concave and convex conical ends. The effective permittivity profile is computed according to the local needle volume fraction. For instance, in both end-cluster and stem-cluster, the needle volume fraction decreases radially. Figure 3.12(a) shows a transverse slice of a needle cluster. The needle volume fraction is inversely proportional to radial distance $|OA|$. For end-clusters, the needle volume fraction also increases from the bottom to the tip due to the decrease of the tilt angle of the needles. Figure 3.12(b) shows a longitudinal slice of an end-cluster. The needle volume fraction is proportional to $1/\sin\theta_t$, where θ_t is the local needle tilt angle.

Once the information related to needle volume fraction is known, the effective permittivity at each point can be calculated using the Clausius-Mossotti dielectric mixing formula [52]

$$\bar{\bar{\epsilon}}_{eff} = \epsilon_h \left[\bar{\bar{I}} + (\bar{\bar{I}} - \frac{\eta < \bar{\bar{\alpha}} >}{3\epsilon_h})^{-1} \cdot \frac{\eta < \bar{\bar{\alpha}} >}{\epsilon_h} \right] \tag{3.24}$$

where ϵ_h is the permittivity of the background medium which is air, η is the needle

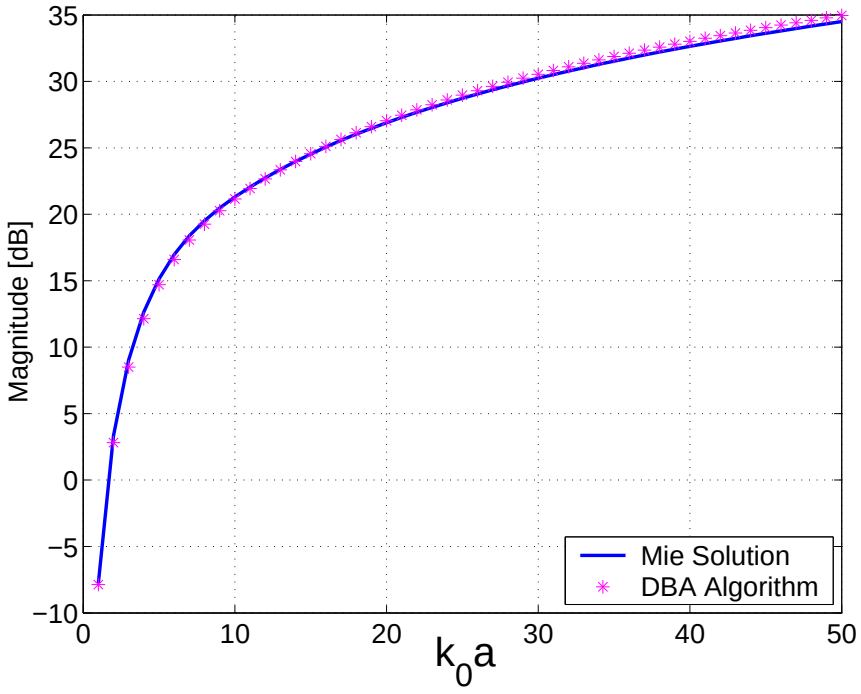

(a)

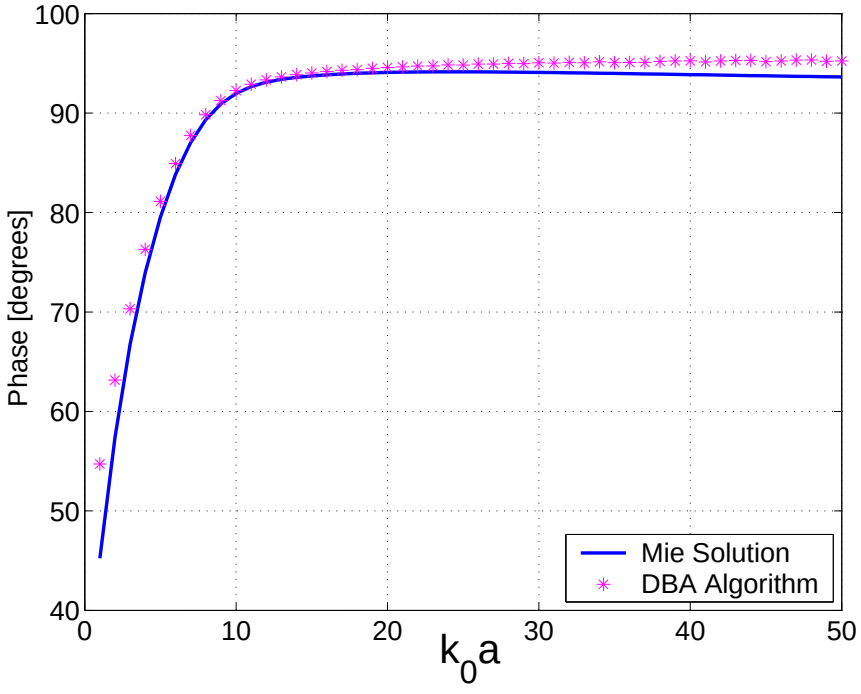

(b)

Figure 3.9: Forward scattering from a dielectric sphere ($\epsilon_r = 1.5 + j0.5$) versus $k_0 a$, computed by DBA algorithm and Mie solution : (a) magnitude (in dB), (b) phase (in Degrees).

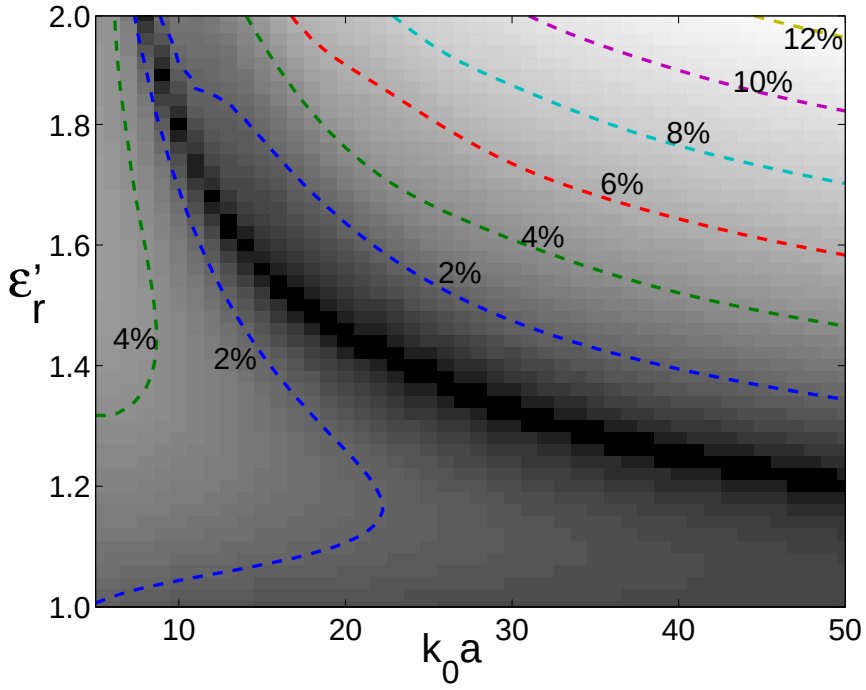

(a)

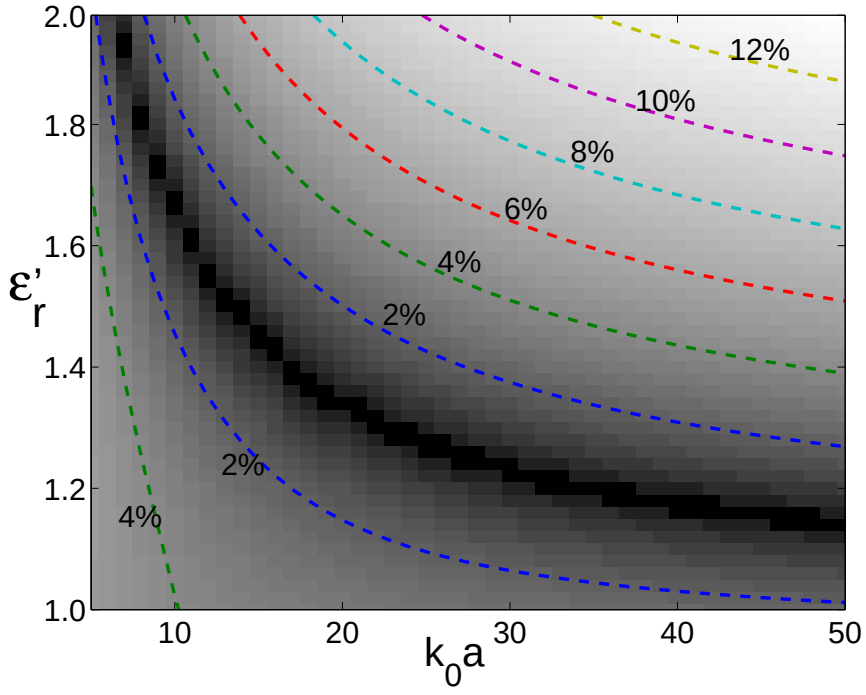

(b)

Figure 3.10: Percentage error of forward scattering magnitude computed by DBA algorithm compared to Mie solution for a dielectric sphere with fixed loss tangent, versus normalized size k_0a and real part of relative dielectric constant ϵ_r': (a) loss tangent = 0.1, (b) loss tangent = 0.3.

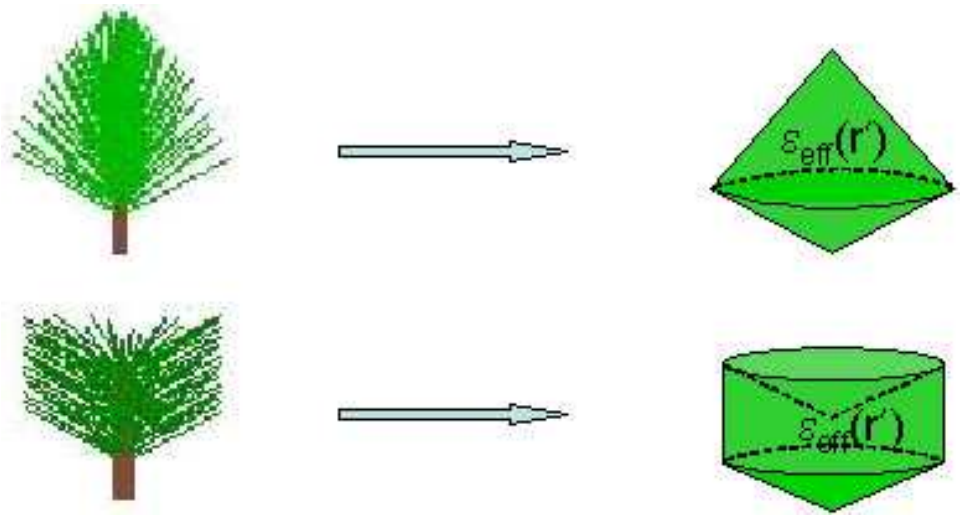

Figure 3.11: Effective dielectric blocks approximated from needle clusters.

volume fraction of the cell, and $< \overline{\overline{\alpha}} >$ is the polarizability tensor averaged over the needle orientation angle. For a needle segment oriented at angle (θ_t, ϕ_t) the associated polarizability tensor of the needle can be calculated as

$$\overline{\overline{\alpha}} = \overline{\overline{T}}^{-1} \cdot \overline{\overline{\alpha}}_0 \cdot \overline{\overline{T}} \tag{3.25}$$

where, $\overline{\overline{\alpha}}_0$ is the polarizability tensor when $(\theta_t, \phi_t) = (0, 0)$ and is given by [50]

$$\overline{\overline{\alpha}}_0 = \begin{pmatrix} \frac{2(\epsilon_n - 1)}{\epsilon_n + 1} & 0 & 0 \\ 0 & \frac{2(\epsilon_n - 1)}{\epsilon_n + 1} & 0 \\ 0 & 0 & \epsilon_n - 1 \end{pmatrix}, \tag{3.26}$$

ϵ_n is the permittivity of the needles, and $\overline{\overline{T}}$ is the coordinate transformation matrix given by [51]

$$\overline{\overline{T}} = \begin{pmatrix} \cos\theta_t \cos\phi_t & \cos\theta_t \sin\phi_t & -\sin\theta_t \\ -\sin\phi_t & \cos\phi_t & 0 \\ \sin\theta_t \cos\phi_t & \sin\theta_t \sin\phi_t & \cos\theta_t \end{pmatrix}. \tag{3.27}$$

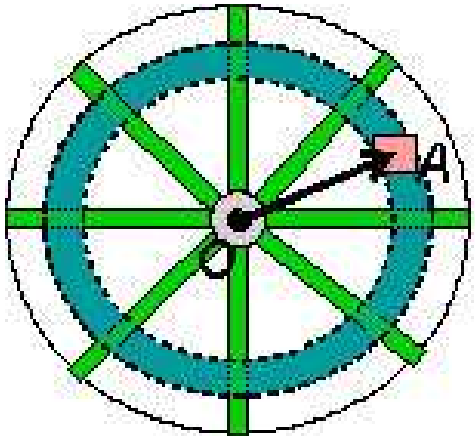

(a)

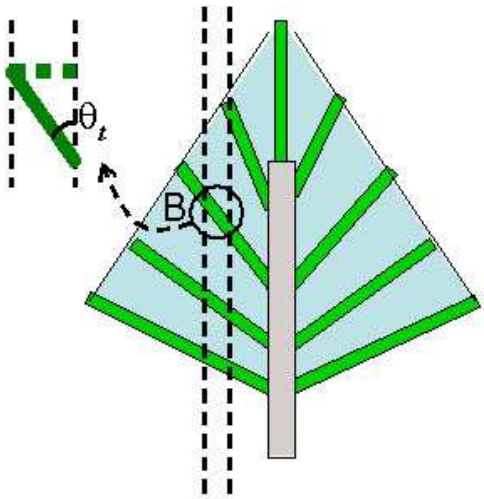

(b)

Figure 3.12: (a) A transverse slice of the needle clusters, (b) A longitudinal slice of the end-cluster.

Due to the azimuthal symmetry of the needles, ϕ_t is a random variable uniformly distributed over $[0, 2\pi]$. Averaging over ϕ_t leads to a diagonal tensor $\overline{\overline{\alpha}}$ with $\alpha_{11} = \alpha_{22} = (1 + \cos^2\theta_t)/(\epsilon_n + 1) + \sin^2\theta_t/2$ and $\alpha_{33} = 2\sin^2\theta_t/(\epsilon_n + 1) + \cos^2\theta_t$.

After implementing the DBA algorithm for the needle clusters, the scattering pattern is compared with the exact MoM solution. Figure 3.13 shows the forward scattering from an end-cluster versus the incident angle. The DBA solution (dashed line) agrees well with the MoM solution (solid line) with less than 0.5 dB in error magnitude and less than 10 degrees error in the phase. Figure 3.14 plots the bistatic scattering patterns from the same needle cluster at angles near the forward scattering direction. Comparison with MoM shows very good agreement in both magnitude and phase of the bistatic scattering patterns. It should be mentioned that the simulation results presented so far are all based on a free space environment. The ground plane effect on the scattered wave from the needle clusters is taken into account afterwards in the wave propagation model using a geometric optics approach [14, 18, 53]. Since the needle clusters are not very close to the ground (many wavelengths away), the ground does not affect the multiple-scattering within the needle clusters.

It should be noted that the DBA algorithm described above requires numerical integration over the volume of the scatterer, however, compared to MoM, DBA is much less computationally intensive, and is scalable with the increase in the number of needles since the shape of the average scatterer is not affected by the number and only the needle volume fraction increases. The computation time for the end-cluster using MoM takes about 1 hour, whereas the same simulation using DBA takes only about 20 seconds.

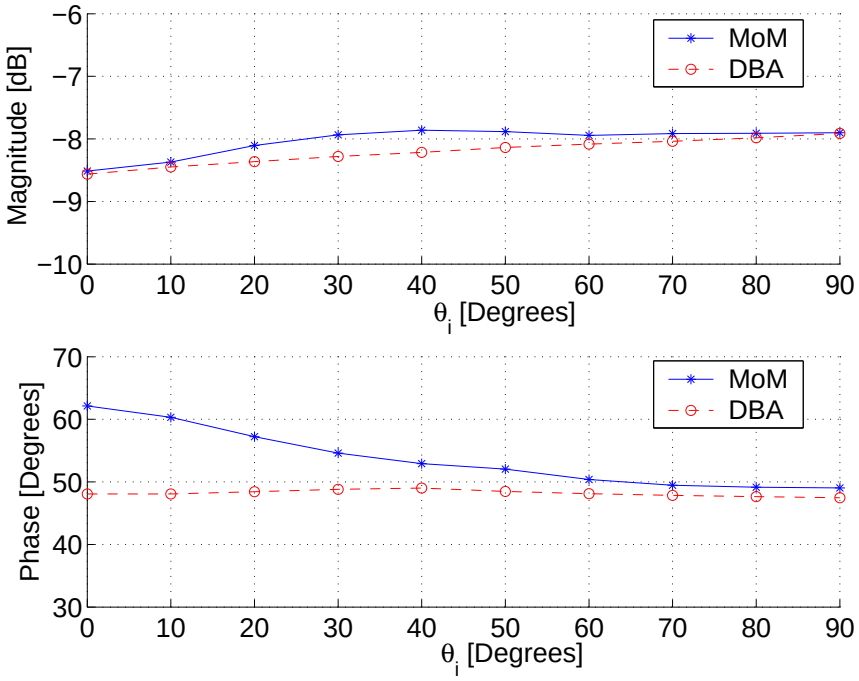

(a)

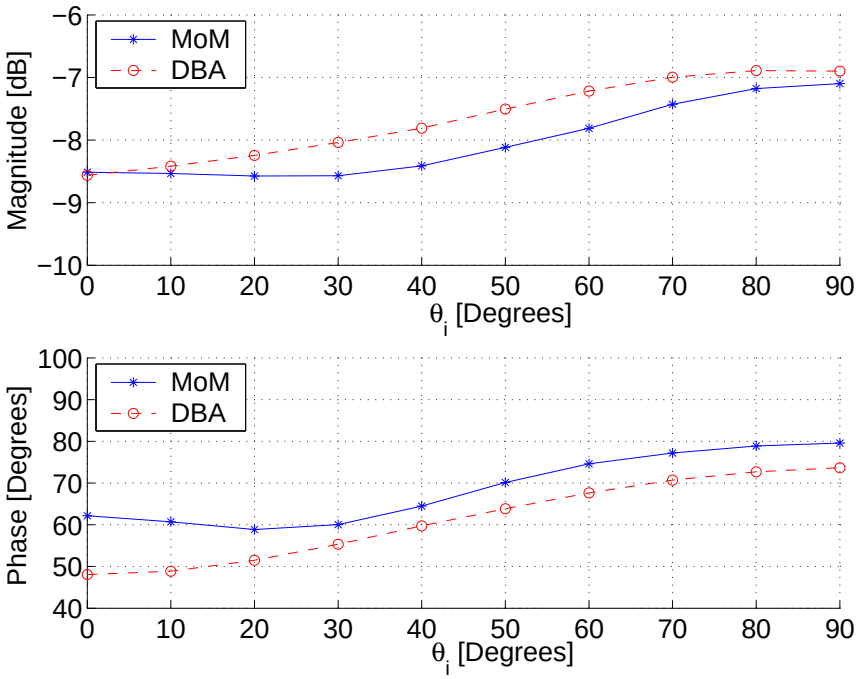

(b)

Figure 3.13: Comparison of forward scattering from a needle cluster between DBA and MoM: (a) S_{hh}, (b) S_{vv}.

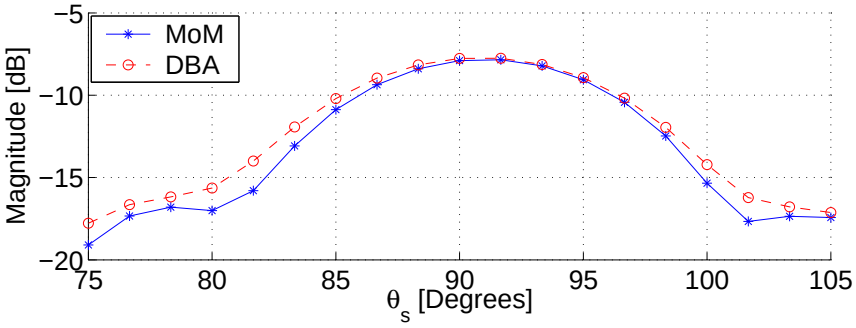

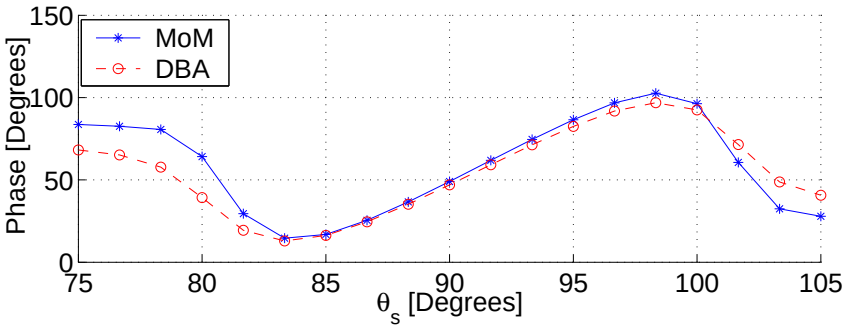

(a)

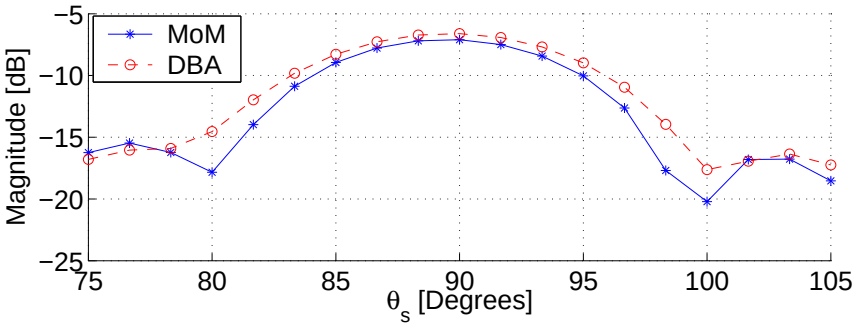

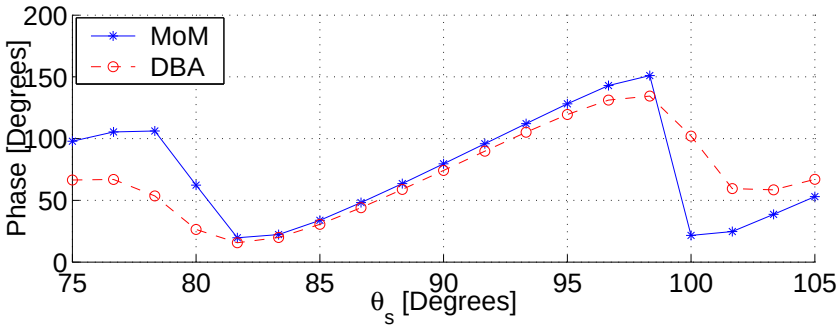

(b)

Figure 3.14: Comparison of bistatic scattering pattern from a needle cluster between DBA and MoM: (a) S_{hh}, (b) S_{vv}.

3.4 Outdoor Measurement of Wave Propagation Through Foliage

In this section, the procedure for an outdoor wave propagation measurement is described and the comparison between the measurement and wave propagation simulation results is presented. Simulation results using single-scattering and using the macro-model to estimate the coherent mean-field attenuation rate are both presented, indicating an improvement by including the effect of multiple-scattering in the dense leaf clusters.

The outdoor measurement was conducted in November, 2002 for a pine tree stand including 13 red pine trees (5 rows, 2-3 trees each row) at Ka-band (35 GHz). This stand occupies a 15m $\times$ 25m area with an average distance of 5m between two adjacent trees. The average tree height, crown depth, and crown diameter are 7.5m, 6.4m, and 5.5m, respectively. Figure 3.15 shows the measurement system block diagram designed for this experiment. Power measurement was performed for determining the path-loss. The transmitted power was set at 23 dBm which was radiated through a horn antenna with a gain of 28 dB. The received signal was down-converted to an IF band (30 MHz) using a harmonic mixer. The IF signal was then amplified and filtered before detection by a spectrum analyzer. The receiver antenna was a horn antenna identical to the transmitter antenna having a half-power beamwidth of 10 degrees. The transmitter was located in a clear area, 20m away from the tree stand, illuminating it from the side. The distance was chosen so that the tree line was in the far-field of the transmitter antenna. The antenna footprint at 20m away is about 3m $\times$ 3m which is substantially smaller than the tree crown dimensions, ensuring a distributed illumination. The receiver was first set up in front of the tree line for calibrating the system, and then moved behind the trees for taking power measurements. The received power in front of the tree stand is proportional to the system gain minus the free space loss, and the power received behind the tree stand

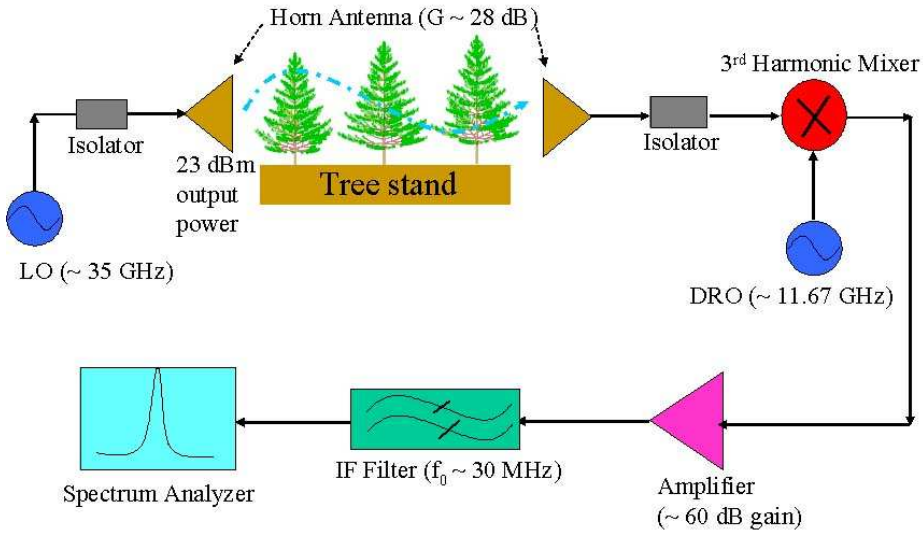

Figure 3.15: Block diagram of the wave propagation measurement system.

is equal to the same system gain minus the sum of a different free space loss and the path-loss due to the tree stand. By comparing these two power measurements and correcting for the difference in the free space loss, the path-loss through the tree stand is obtained.

For this measurement both the transmitter and receiver antennas were kept 1.3m above the ground, at a height above the trunk layer. The alignment of the transmitter and receiver antennas was achieved by attaching a laser pointer parallel to the antenna boresight at each antenna. To acquire the desired path-loss statistics, 84 independent spatial samples of the transmitted signal through the pine stand were collected. The FCSM is used to simulate propagation and scattering through the tree stand. Ground truth measurements were performed to ensure that the computer-generated fractal tree model is as close as possible to the real trees. FCSM is modified for the normal incidence case, and the antenna patterns of both transmitter and receiver antennas are taken into account. 100 realizations were performed for this Monte-Carlo simulation to obtain the statistics of the field through foliage. The cumulative distribution function (CDF) of the calibrated path-loss from outdoor measurements

Table 3.1: Comparison of mean and stand deviation of path-loss between measurement and simulation results.

	Mean (dB)	Std. (dB)
Measurement	-24.8	-23.8
Multi. Scat. (macro-model)	-26.4	-25.6
Single Scat. (semi-exact)	-33.1	-32.3
Single Scat. (Rayleigh-Gans)	-51.7	-51.9

(solid line) and computer simulations are shown in Figure 3.16. Table 7.1 also shows the mean and standard deviation of the path-loss of these results. It is obvious that single-scattering applied to pine needles whose scattering are computed by Rayleigh-Gans approximation (dotted line) grossly overestimates path-loss at millimeter-wave frequencies. Using single-scattering in conjunction with the semi-exact solution to calculate the scattering from individual needles (dashed line), the path-loss estimate improves but there is still 8$\sim$9 dB of difference between the simulation and measured results. Using the macro-model where the multiple-scattering effects in the needle clusters are accounted for in the wave propagation model (dot-dash line) the agreement between the measurement and simulation results is markedly improved. It is also worth mentioning that the macro-model also improves the computation time of the wave propagation simulation as well. This is due to the fact that many needles ($\sim$100) are lumped into one scatterer, and the scattering matrix of this scatterer is pre-computed and stored to be used as a lookup table. Comparing the computation time of the propagation simulation using the macro-model multiple-scattering and the Rayleigh-Gans single-scattering, a speedup of about 30% is achieved (the latter one takes about 10 hours).

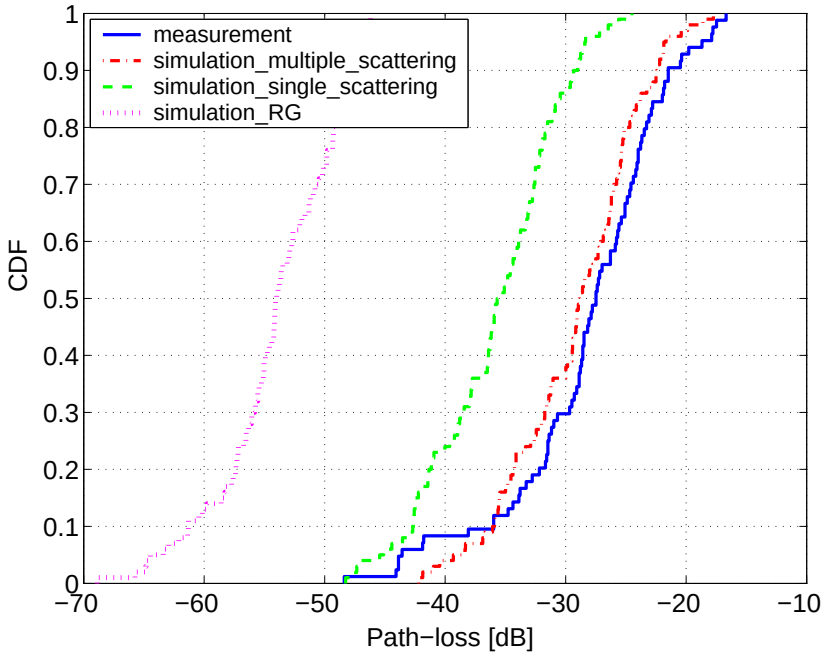

Figure 3.16: Comparison of path-loss through foliage between measurement and simulation results.

3.5 Conclusions

In this chapter the accuracy of single-scattering theory for estimation of attenuation rate of a dense medium like a needle cluster is examined by comparing methods based on single-scattering theory and a full-wave solution MoM. Simulations of forward scattering show that single-scattering theory usually overestimates the attenuation rate. This is severe at high frequencies since scatterers become electrically large and fall within the near field of each other.

To incorporate the multiple-scattering effects from needle clusters without increasing the complexity or the computation time, a novel macro-modeling approach is presented. This is done by modeling the bistatic scattering outside the forward scattering beam by an incoherent field having a constant average bistatic scattering pattern, and inside the forward scattering beam by the distorted Born approximation (DBA). It is shown that when DBA is applied to the equivalent "average scatterer"

having an inhomogeneous and anisotropic dielectric constant the mean bistatic scattered field can be computed very accurately. The results of the macro-model for an end-cluster and a stem-cluster are compared with the MoM solution. The macro-model is accurate, and is by two orders of magnitude faster than the MoM solution.

An outdoor path-loss measurement was conducted for a pine tree stand to examine the accuracy of the wave propagation model using the macro-model. The comparison between the measurement and simulation results shows that for this specific case the propagation model that uses single-scattering to estimate coherent mean-field overestimates the path-loss by 8$\sim$9 dB, whereas when the macro-model is used the path-loss estimate is within 1$\sim$2 dB of the measured results.

CHAPTER 4

SWAP: ACCURATE AND TIME-EFFICIENT PREDICTION OF FOLIAGE PATH-LOSS

4.1 Introduction

It is well known that forested environments can affect wireless communication significantly and impose stringent constraints on system design. The most important effect introduced by the forest is the extra signal path-loss in addition to that due to free space propagation. This extra path-loss is often referred to as foliage path-loss. Signal attenuation caused by the forest is due to absorption and scattering by discrete scatterers such as branches and leaves within the forest. Foldy's approximation [16, 24] has been widely used to estimate the signal attenuation rate in sparse random media. It predicts an exponential decay of the field, which corresponds to a linear foliage path-loss (in dB) versus the wave propagation distance. However, Foldy's approximation can only capture the coherent power which is due to the mean-field of the signal. In addition, the random distribution of foliage particles outside the line-of-sight scatters the incident wave and redirects some of it towards the receiver, generating incoherent power. For long distance communication systems, such a contribution tends to dominate the overall received power after the exponentially-decaying coherent power becomes insignificant. For larger distances, this phenomenon results in a different slope of the foliage path-loss (in dB). This is the so-called "dual-slope"

phenomenon of the foliage path-loss often observed experimentally in forested environments [20, 25, 26].

In order to account for the effects of incoherent power in the propagation model, both radiative transfer and wave theory approaches have been pursued [15]. As mentioned earlier, the radiative transfer approach is not suitable for forested environments which contain three-dimensional complex tree structures, due to the difficulties in determining the phase and extinction matrices; while the wave theory model, FCSM (fractal-based coherent scattering model), introduced in the previous chapters provides a better solution. However, FCSM is essentially a single-scattering model. For highly scattering environments and long propagation distances, multiple-scattering effects become important in estimating both the coherent mean-field and the incoherent power, and must be taken into account. In chapter 3, an enhanced model was developed to improve the Foldy's approximation in estimating the coherent mean-field. The enhanced model is especially necessary at high frequency bands (e.g. millimeter-wave range) where mutual coupling of densely clustered leaves is strong. At lower frequencies, such as the UHF (ultra high frequency) band, mutual coupling is not as significant, but the multiple bounces between distant scatterers, such as those between two branches, contribute to the incoherent power at the receiver. Such a contribution is generally smaller than the single-scattering components. However, when the propagation distance is large, where the incoherent power dominates, this contribution may result in an observable increment in the overall incoherent power.

Another limitation of FCSM lies in the required computation time. Computing scattered fields from all scatterers inside the large dimensions of a forested environment can be prohibitively time-consuming even when single-scattering models are used. The aforementioned difficulty can be circumvented by treating the forest as a statistically homogeneous medium along the direction of wave propagation and only analyzing a typical block of forest using FCSM. This way, the computation time

can be significantly reduced while the prediction accuracy can still be maintained as compared to a brute force approach which applies FCSM to the whole forest environment. A new model based on such methodology, which is referred to as the Statistical WAve Propagation model (SWAP), has been developed recently and is presented in this chapter. The new model can also be adjusted to incorporate multiple-scattering in computing the incoherent power. Using the SWAP model, simulation results for foliage path-loss as a function of propagation distance, frequency, and forest density are presented, and the new model is also validated by comparing its predictions against independent propagation measurements through foliage.

4.2 SWAP Model

In this section, the details of the SWAP model are described. Figure 4.1 shows the scenario of plane wave propagation through a forested environment which is statistically homogeneous in the sense that the average structural features of the forest, such as tree species and tree density, along the direction of wave propagation are the same. Therefore the forest can be divided into similar blocks cascaded along the propagation direction. With a sufficient number of trees in every block, the wave propagation behavior within each block is statistically identical. By applying the existing FCSM model to a single block, these properties can be obtained and then reused for all blocks. Together with network theory, the field statistics over arbitrarily large distances can be calculated. This approach keeps track of all coherent and incoherent wave components through all forest blocks, and accounts for multiple-scattering effects between scatterers in different blocks. In addition, it only requires wave propagation computation over a relatively short distance, i.e. the extent of a single block of forest, hence reducing computation time significantly. The dimensions of the forest block must be carefully selected to be just large enough to ensure cap-

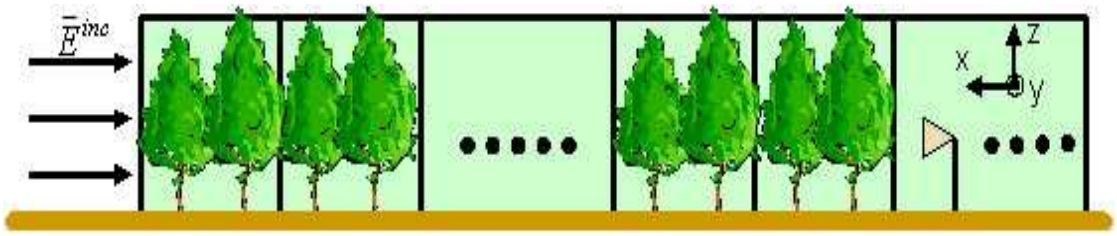

Figure 4.1: A forest divided into statistically similar blocks.

turing all structural features of the forest. Any larger and the time efficiency will suffer.

4.2.1 Estimation of Wave Propagation Parameters

The most important wave propagation parameters include: 1) the coherent mean-field propagation constants; 2) the coefficient of variation and the spatial correlation function of the field distribution on the output surface of a forest block; and 3) the transfer matrix between field distributions on the input and output surfaces of that block.

The coherent mean-field propagation constants M_{pq} are estimated according to Foldy's approximation by (2.1). In order to estimate the coefficient of variation and the spatial correlation function, the electric field statistics at the output surface of the block is computed using the FCSM model. Considering the statistical homogeneity along the horizontal dimension of the forest (y-direction in Figure 4.1), the data points obtained along the horizontal direction are averaged to obtain better statistical values. Since field variation is small in a half-wavelength neighborhood, these points are spaced by less than that before averaging. Similarly the spacing of data points along the vertical direction is selected to be half a wavelength or smaller. The coefficient of variation is defined by

$$\sigma/\mu = \frac{\sigma[\bar{E}_p(\bar{r}')]}{|\langle \bar{E}_p(\bar{r}') \rangle|} \tag{4.1}$$

where $\bar{E}_p(\bar{r}')$ is the field distribution of polarization p at the location $\bar{r}'$ on the output

surface and can be written as a sum of the mean and fluctuating components, i.e.

$$\bar{E}_p(\bar{r}') = \langle \bar{E}_p(\bar{r}') \rangle + \widetilde{E_p}(\bar{r}'). \tag{4.2}$$

$\sigma[\bar{E}_p(\bar{r}')]$ is the standard deviation of $\bar{E}_p(\bar{r}')$, and in fact $\sigma[\bar{E}_p(\bar{r}')] = \sigma[\widetilde{E_p}(\bar{r}')]$, since $\langle \widetilde{E_p}(\bar{r}') \rangle = 0$. The spatial correlation function of the electrical field is defined and computed as

$$\begin{aligned} C[\bar{E}_p(\bar{r}_1'), \bar{E}_q(\bar{r}_2')] &= \frac{\langle [\bar{E}_p(\bar{r}_1') - \langle \bar{E}_p(\bar{r}_1') \rangle] \cdot [\bar{E}_q(\bar{r}_2') - \langle \bar{E}_q(\bar{r}_2') \rangle]^* \rangle}{\sigma[\bar{E}_p(\bar{r}_1')] \cdot \sigma[\bar{E}_q(\bar{r}_2')]} \\ &= \frac{\langle \widetilde{E_p}(\bar{r}_1') \cdot \widetilde{E_q}(\bar{r}_2')^* \rangle}{\sigma[\widetilde{E_p}(\bar{r}_1')] \cdot \sigma[\widetilde{E_q}(\bar{r}_2')]} \end{aligned} \tag{4.3}$$

where $\widetilde{E_p}(\bar{r}_1')$ and $\widetilde{E_q}(\bar{r}_2')$ are the field distributions at $\bar{r}_1'$ and $\bar{r}_2'$ on the output surface, of polarization p and q, respectively. Numerical experiments show that the quantities defined in (4.1) and (4.3) depend only on the properties of the forest, not the incident wave. Figure 4.2 shows some typical spatial correlation functions along the vertical and horizontal dimensions, as calculated with this method. These simulations were conducted with a red pine tree stand at a tree density of 0.05 trees/m^2 (i.e. 5 trees per 100 square meters) and a frequency of 0.5 GHz. V-V polarization is assumed, i.e. both p and q are vertical polarizations. $C_1(\Delta z)$ is the correlation function between a fixed point (near the trunk region) on a vertical line and another point on the same line, where Δz is the distance between these two points. $C_2(\Delta z)$ is the correlation function along the vertical line for a fixed point in the crown region. $C_3(\Delta y)$ and $C_4(\Delta y)$ are correlation functions along the horizontal direction for two fixed points at the same height above the ground. As shown in Figure 4.2, $C_3(\Delta y)$ and $C_4(\Delta y)$ are almost the same, as expected. $C_1(\Delta z)$ and $C_2(\Delta z)$ are much different from each other due to the inhomogeneous forest structure along the vertical dimension. Also notice

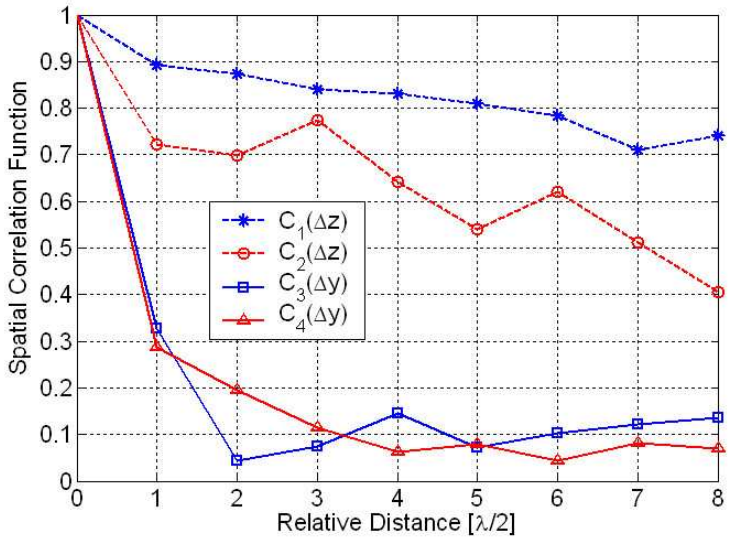

Figure 4.2: Spatial correlation functions along the vertical and horizontal dimensions.

that $C(\Delta z)$ drops much more slowly than $C(\Delta y)$, indicating a strong correlation along the vertical dimension caused by structural correlation of the forest.

The relationship between the input and output surface fields of a single forest block is of great importance in building the propagation network in the SWAP model, and can be estimated by computing a field transfer matrix. As shown in Figure 4.3, both input and output surfaces of a single forest block are divided into K pixels with spacing half a wavelength or smaller. Therefore the field within one pixel can be assumed approximately constant. According to the field equivalence principle [54], equivalent surface currents (two polarizations) at each input pixel can be deduced from the field distribution inside that pixel. These currents, acting as a radiation source, emit electromagnetic waves that propagate through the forest block and generate a field at every output pixel. Therefore the input-output field relationship can be represented as a $K \times K$ transfer matrix $\overline{\overline{T}}(\bar{r}', \bar{r}'')$. The elements, T_{ij}, relate the field distribution at the j^{th} pixel on the input surface and the i^{th} pixel on the output surface, where $\bar{r}'$ and $\bar{r}''$ stand for the locations of an input surface pixel and an output surface pixel, respectively. When the mean-field on the output surface is desired, it can be obtained

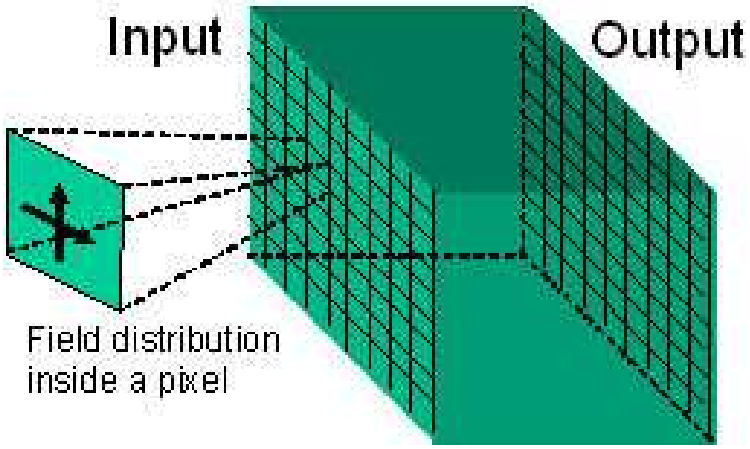

Figure 4.3: Input-output field relationship of a single block of forest.

by treating the forest block as an "average" lossy dielectric medium with propagation constants M_{pq}, and letting the emitted electromagnetic waves travel in the effective medium.

4.2.2 Propagation Network of Cascaded Forest Blocks

In this section, the procedure for computing the received power (from which the foliage path-loss can be deduced) is explained. The single-block wave propagation parameters estimated previously will be used repeatedly, in conjunction with a propagation network. Figure 4.4 shows the block diagram of the proposed propagation network in the SWAP model. There are altogether N cascaded forest blocks between the transmitter (Tx) and receiver (Rx). The total field at the receiver is given by

$$\bar{E}(\bar{r}) = \langle \bar{E}(\bar{r}) \rangle + \widetilde{E}(\bar{r}) \tag{4.4}$$

where $\bar{r}$ represents the receiver location. $\langle \bar{E}(\bar{r}) \rangle$ represents the coherent mean-field; $\widetilde{E}(\bar{r})$ is the fluctuating field and $\langle \widetilde{E}(\bar{r}) \rangle = 0$. Therefore, the average received power

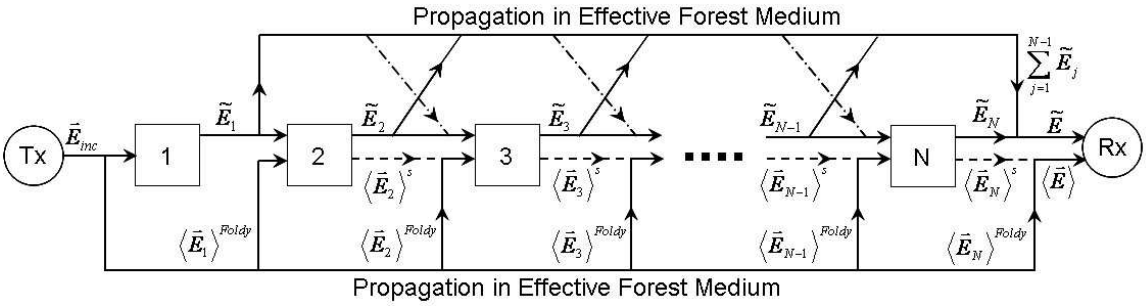

Figure 4.4: Network block diagram of in-forest horizontal wave propagation model using cascaded forest blocks.

contains coherent and incoherent components and is given by

$$\langle |\bar{E}(\bar{r})|^2 \rangle = |\langle \bar{E}(\bar{r}) \rangle|^2 + \langle |\widetilde{E}(\bar{r})|^2 \rangle. \tag{4.5}$$

Consequently the foliage path-loss can be computed as $|\bar{E}^{inc}|^2 / \langle |\bar{E}(\bar{r})|^2 \rangle$, where $|\bar{E}^{inc}|^2$ represents the power carried by the incident wave when hitting the front edge of the forest.

To compute the coherent power $|\langle \bar{E}(\bar{r}) \rangle|^2$ and the incoherent power $\langle |\widetilde{E}(\bar{r})|^2 \rangle$, express the total field at the surface of each block as the sum of the mean-field and the fluctuating field. That is, at the output surface of the $(j-1)^{th}$ block, the field distribution can be written as

$$\bar{E}_{j-1}(\bar{r}'') = \langle \bar{E}_{j-1}(\bar{r}'') \rangle + \widetilde{E}_{j-1}(\bar{r}'') \tag{4.6}$$

where $\bar{r}''$ is an arbitrary point on the surface. According to the field equivalence principle, $\bar{E}_{j-1}(\bar{r}'')$ acts as an excitation source illuminating the j^{th} block and generating fields at its output surface. An operator $L\{\ \}$ can be defined between the equivalent sources on the input surface and the mean-fields on the output surface of the block.

That is, $\langle \bar{E}_j(\bar{r}') \rangle$ can be computed as

$$\langle \bar{E}_j(\bar{r}') \rangle = L\{\bar{E}_{j-1}(\bar{r}'')\} = L\left\{\langle \bar{E}_{j-1}(\bar{r}'') \rangle + \widetilde{E}_{j-1}(\bar{r}'')\right\} \tag{4.7}$$

where $\bar{r}'$ is an arbitrary point on the output surface of the j^{th} block. In fact, as shown in Figure 4.4, $\bar{E}_j(\bar{r}')$ has two components, i.e.

$$\langle \bar{E}_j(\bar{r}') \rangle = \langle \bar{E}_j(\bar{r}') \rangle^{Foldy} + \langle \bar{E}_j(\bar{r}') \rangle^{s} \tag{4.8}$$

where $\langle \bar{E}_j(\bar{r}') \rangle^{Foldy}$ corresponds to the attenuated direct coherent mean-field from the transmitter, and $\langle \bar{E}_j(\bar{r}') \rangle^{s}$ (indicated by the dashed lines) corresponds to all other contributions. Changing the subscript in equation (4.8) from "j" to "$j-1$" and substituting into equation (4.7), one obtains

$$\begin{aligned} \langle \bar{E}_j(\bar{r}') \rangle &= L\left\{\langle \bar{E}_{j-1}(\bar{r}'') \rangle^{Foldy} + \langle \bar{E}_{j-1}(\bar{r}'') \rangle^{s} + \widetilde{E}_{j-1}(\bar{r}'')\right\} \\ &= L\{\langle \bar{E}_{j-1}(\bar{r}'') \rangle^{Foldy}\} + L\left\{\langle \bar{E}_{j-1}(\bar{r}'') \rangle^{s} + \widetilde{E}_{j-1}(\bar{r}'')\right\}. \end{aligned} \tag{4.9}$$

Comparing equations (4.8) and (4.9), one finds that

$$\langle \bar{E}_j(\bar{r}') \rangle^{Foldy} = L\left\{\langle \bar{E}_{j-1}(\bar{r}'') \rangle^{Foldy}\right\} \tag{4.10}$$

and

$$\langle \bar{E}_j(\bar{r}') \rangle^{s} = L\left\{\langle \bar{E}_{j-1}(\bar{r}'') \rangle^{s} + \widetilde{E}_{j-1}(\bar{r}'')\right\}. \tag{4.11}$$

$\langle \bar{E}_j(\bar{r}') \rangle^{Foldy}$ can be obtained from the incident wave $\bar{E}^{inc}$ propagating through the "average" forest medium using Foldy's approximation, i.e.

$$\langle \bar{E}_j(\bar{r}') \rangle^{Foldy} = \bar{E}^{inc} \cdot e^{j(k_0+M)R} \tag{4.12}$$

where M is the Foldy's propagation constants (polarization subscript neglected) and R is the propagation distance inside the forest. For $\langle \bar{E}_j(\bar{r}') \rangle^s$, the operator $L\{\ \}$ can be realized approximately via the transfer matrix, $\overline{\overline{T}}(\bar{r}', \bar{r}'')$. By cascading the mean-field through each block to the output of the N^{th} block, the coherent power can be calculated since $\langle \bar{E}_N \rangle = \langle \bar{E} \rangle$, as shown in Figure 4.4. The incoherent power at the receiver is made up of contributions from scattered fields by random scatterers within all individual forest blocks. For example, the fluctuating field $\widetilde{E}_j(\bar{r}')$at the output surface of the j^{th} block is caused by random scattering within the j^{th} block. It then reradiates as a secondary source through the "average" forest medium and generates a component of the fluctuating field, $\widetilde{E}_j(\bar{r})$, at the receiver, where $\bar{r}$ is the position of the receiver. Therefore the total incoherent power can be obtained by

$$\langle |\widetilde{E}(\bar{r})|^2 \rangle = \sum_{j=1}^{N} \langle |\widetilde{E}_j(\bar{r})|^2 \rangle. \tag{4.13}$$

Here we have used the fact that the fluctuating scattered fields generated by different blocks are statistically independent.

The fluctuating field $\widetilde{E}_j(\bar{r}')$ is computed by reusing the statistical parameter σ/μ instead of applying the brute force FCSM to each forest block over and over again, since numerical simulations show that this quantity is invariant for different forest blocks along the direction of wave propagation. With the mean-field $\langle \bar{E}_j(\bar{r}') \rangle$ calculated, the standard deviation of $\bar{E}_j(\bar{r}')$, or $\widetilde{E}_j(\bar{r}')$, can be obtained by multiplying σ/μ with the mean-field amplitude $|\bar{E}_j(\bar{r}')|$. Once $\sigma[\widetilde{E}_j(\bar{r}')]$ is known, pseudo-random samples of $\widetilde{E}_j(\bar{r}')$ are generated assuming it is a zero-mean Gaussian random variable. This pseudo-random sample of $\widetilde{E}_j(\bar{r}')$ is generated for each realization in a Monte-Carlo simulation (different one from that used for single block wave propagation behavior estimation), enabling one to compute a sample of the received power. With a sufficient number of samples computed, the average and variance of the received

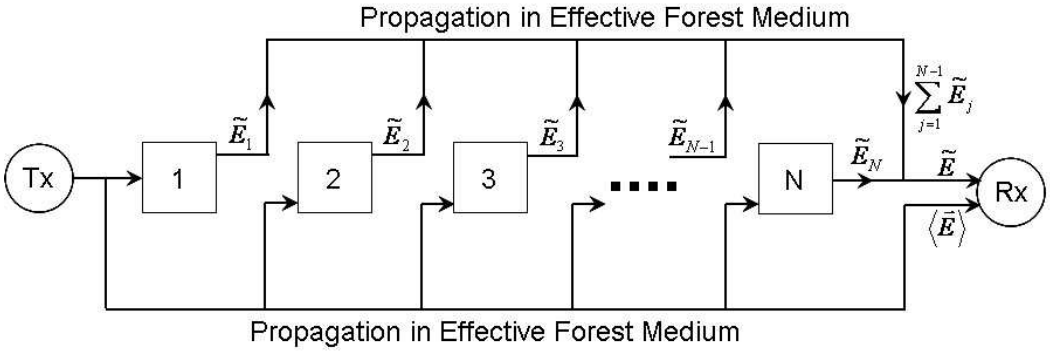

Figure 4.5: Simplified network block diagram of the SWAP model with only single-scattering mechanisms accounted for between blocks.

power can be obtained.

It is worth mentioning that Figure 4.4 includes all the multiple-scattering effects in the forward direction between scatterers within different forest blocks. For example, the transfer matrix $\overline{\overline{T}}(\bar{r}', \bar{r}'')$ relays the scattering from inside the $(j-1)^{th}$ block into the scattering inside the j^{th} block ($\widetilde{E}_{j-1}(\bar{r}'') \rightarrow \langle \bar{E}_j(\bar{r}') \rangle \rightarrow \widetilde{E}_j(\bar{r}')$). In fact, $\overline{\overline{T}}$ can be generalized to relate scattering that occurs inside any two distant blocks, as illustrated in Figure 4.4 by the dash-dotted lines. However, multiple-scattering between scatterers within the same block is not accounted for. In the case where single-scattering is sufficient for the entire forest, the SWAP model can be simplified by turning off the between-block multiple-scattering mechanisms, i.e. neglecting the excitations of $\langle \bar{E}_{j-1}(\bar{r}'') \rangle^s$ and $\widetilde{E}_{j-1}(\bar{r}'')$ on the j^{th} block. The resulting single-scattering SWAP model is equivalent to the FCSM model applied to the entire forest. Figure 4.5 shows the block diagram of this simplified model. In the SWAP model described so far, backscattering mechanisms are neglected since they are generally much smaller than the contribution from forward scattering.

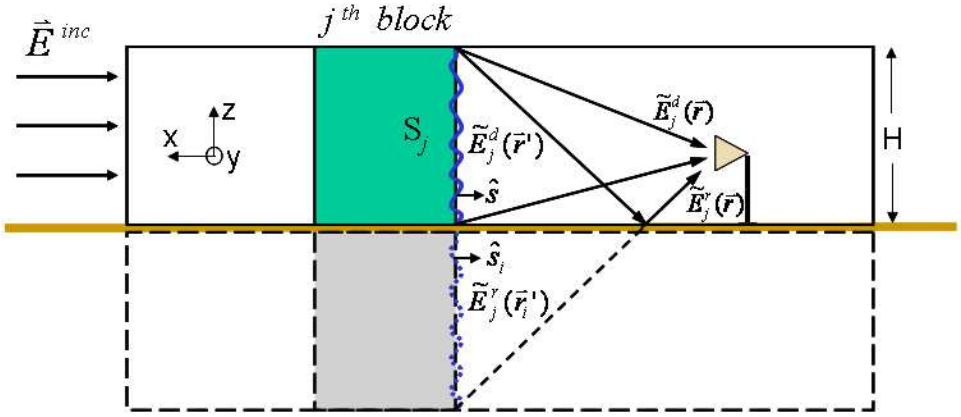

Figure 4.6: Fluctuating fields from each block generate incoherent power at the receiver (ground reflection effect accounted for by using image of the fluctuating fields).

4.2.3 Formulation for Computing Incoherent Power

To complete the specification of the SWAP model, one must compute the contribution of $\widetilde{E}_j(\bar{r}')$ to the incoherent power, i.e. $\langle|\widetilde{E}_j(\bar{r})|^2\rangle$. Figure 4.6 shows the geometry of this propagation problem where the output surface of the j^{th} block is shown as S_j. Also shown is the image of the j^{th} block in the ground plane. The ground effect is accounted for by using approximate image theory [55]. Here the fluctuating field distribution and its image are respectively denoted by $\widetilde{E}_j^d(\bar{r}')$ and $\widetilde{E}_j^r(\bar{r}')$, where the superscripts "d" and "r" stand for "direct" and "reflected". The vertical (z-direction) and horizontal (y-direction) extent of the forest block are denoted by H and W respectively.

Based on the field equivalence principle, the surface fields on S_j can be replaced with a magnetic current $\widetilde{J}_m(\bar{r}')$, given by

$$\widetilde{J}_m(\bar{r}') = \widetilde{E}_j^d(\bar{r}') \times \hat{s} = \widetilde{E}_j^d(\bar{r}') \times (-\hat{x}), \tag{4.14}$$

backed by a perfect electric conductor (PEC). Similarly, the image fields are equivalent

to the image magnetic current $\widetilde{J}_m^i(\bar{r}_i')$, given approximately by [55]

$$\widetilde{J}_m^i(\bar{r}_i') \approx \Re_{\|}\widetilde{J}_{my}(\bar{r}')\hat{y} + \Re_{\perp}\widetilde{J}_{mz}(\bar{r}')\hat{z}, \tag{4.15}$$

also backed by a PEC. $\Re_{\|}$, $\Re_{\perp}$ are the modified Fresnel reflection coefficients taking into account the ground surface roughness using Kirchhoff's approximation [16]. Then the field radiated from these surface currents to the receiver can be computed as

$$\begin{aligned}\widetilde{E}_j(\bar{r}) &= \widetilde{E}_j^d(\bar{r}) + \widetilde{E}_j^r(\bar{r}) \\ &= \iint_{S_j} \nabla' \times \overline{\overline{G}}(\bar{r},\bar{r}') \cdot 2\widetilde{J}_m(\bar{r}')ds' + \iint_{S_j^i} \nabla' \times \overline{\overline{G}}(\bar{r},\bar{r}_i') \cdot 2\widetilde{J}_m^i(\bar{r}_i')ds_i'.\end{aligned} \tag{4.16}$$

The factor of 2 indicates that the current sources are backed by a planar PEC over the surface S_j and its image. $\overline{\overline{G}}(\bar{r},\bar{r}')$ is the dyadic Green's function of a medium having a permittivity equal to the effective dielectric constant of the forest, and the curl of $\overline{\overline{G}}(\bar{r},\bar{r}')$ is given by

$$\nabla' \times \overline{\overline{G}}(\bar{r},\bar{r}') = \nabla' g(\bar{r},\bar{r}') \times \overline{\overline{I}} = \begin{pmatrix} 0 & -\frac{\partial}{\partial z'} & \frac{\partial}{\partial y'} \\ \frac{\partial}{\partial z'} & 0 & -\frac{\partial}{\partial x'} \\ -\frac{\partial}{\partial y'} & \frac{\partial}{\partial x'} & 0 \end{pmatrix} g(\bar{r},\bar{r}') \tag{4.17}$$

where $\overline{\overline{I}}$ is the dyadic idemfactor, and $g(\bar{r},\bar{r}')$ is the scalar Green's function given by

$$g(\bar{r},\bar{r}') = \frac{e^{jk_eR}}{4\pi R} \tag{4.18}$$

where $R = \sqrt{(x-x_j')^2 + (y-y')^2 + (z-z')^2}$ is the distance from a source point on surface S_j to the receiver location $\bar{r}$, and k_e is the effective wave number in the "average" forest medium. Using equation (4.16), the incoherent power at the receiver

contributed by the j^{th} block of forest can be calculated from

$$\langle|\widetilde{E}_j(\bar{r})|^2\rangle = \langle\widetilde{E}_j(\bar{r})\cdot\widetilde{E}_j(\bar{r})^*\rangle \ = \langle|\widetilde{E}_j^d(\bar{r})|^2\rangle + \langle|\widetilde{E}_j^r(\bar{r})|^2\rangle + 2Re\left\{\langle\widetilde{E}_j^d(\bar{r})\cdot\widetilde{E}_j^r(\bar{r})^*\rangle\right\}. \tag{4.19}$$

The three components in (4.19) are obtained in a similar manner, therefore only the derivation of the first term is presented below, i.e.

$$\begin{aligned}
\langle|\widetilde{E}_j^d(\bar{r})|^2\rangle &= \langle\widetilde{E}_j^d(\bar{r})\cdot\widetilde{E}_j^d(\bar{r})^*\rangle \\
&= \left\langle\left[\int_0^H\int_{-W/2}^{W/2}\nabla'\times\overline{\overline{G}}(\bar{r},\bar{r}_1')\cdot 2\widetilde{J}_m(\bar{r}_1')ds_1'\right]\right. \\
&\quad \left.\cdot\left[\int_0^H\int_{-W/2}^{W/2}\nabla'\times\overline{\overline{G}}(\bar{r},\bar{r}_2')\cdot 2\widetilde{J}_m(\bar{r}_2')ds_2'\right]^*\right\rangle \\
&= \left\langle\int_0^H\int_{-W/2}^{W/2}\int_0^H\int_{-W/2}^{W/2}[\nabla'\times\overline{\overline{G}}(\bar{r},\bar{r}_1')\cdot 2\widetilde{J}_m(\bar{r}_1')]\cdot[\nabla'\times\overline{\overline{G}}(\bar{r},\bar{r}_2')\right. \\
&\quad \left.\cdot 2\widetilde{J}_m(\bar{r}_2')]^* dy_1'dz_1'dy_2'dz_2'\right\rangle.
\end{aligned} \tag{4.20}$$

Substituting equations (4.14) and (4.17) into (4.20), and after some algebraic manipulations one obtains

$$\begin{aligned}
\langle|\widetilde{E}_j^d(\bar{r})|^2\rangle = \frac{1}{4\pi^2}\int_0^H\int_{-W/2}^{W/2}\int_0^H\int_{-W/2}^{W/2}&\frac{e^{jk_eR_1-jk_e^*R_2}(jk_eR_1-1)(-jk_e^*R_2-1)}{R_1^3R_2^3} \\
&\cdot\Big\{\langle\widetilde{E}_{jz}(\bar{r}_1')\cdot\widetilde{E}_{jz}(\bar{r}_2')^*\rangle(z-z_1')(z-z_2') \\
&+\langle\widetilde{E}_{jz}(\bar{r}_1')\cdot\widetilde{E}_{jy}(\bar{r}_2')^*\rangle(z-z_1')(y-y_2') \\
&+\langle\widetilde{E}_{jy}(\bar{r}_1')\cdot\widetilde{E}_{jz}(\bar{r}_2')^*\rangle(y-y_1')(z-z_2') \\
&+\langle\widetilde{E}_{jy}(\bar{r}_1')\cdot\widetilde{E}_{jy}(\bar{r}_2')^*\rangle(y-y_1')(y-y_2') \\
&+\langle\widetilde{E}_{jy}(\bar{r}_1')\cdot\widetilde{E}_{jy}(\bar{r}_2')^*\rangle(x-x_j')^2 \\
&+\langle\widetilde{E}_{jz}(\bar{r}_1')\cdot\widetilde{E}_{jz}(\bar{r}_2')^*\rangle(x-x_j')^2\Big\}dy_1'dz_1'dy_2'dz_2'.
\end{aligned} \tag{4.21}$$

According to equation (4.3)

$$\langle \widetilde{E}_{jp}(\bar{r}'_1) \cdot \widetilde{E}_{jq}(\bar{r}'_2)^* \rangle = C[\widetilde{E}_{jp}(\bar{r}'_1), \widetilde{E}_{jq}(\bar{r}'_2)] \cdot \sigma[\widetilde{E}_{jp}(\bar{r}'_1)] \cdot \sigma[\widetilde{E}_{jq}(\bar{r}'_2)] \tag{4.22}$$

where subscripts "p", "q" can represent either "y" or "z". The dimensions of surface S_j are truncated to the forest extent since the scattered field distribution with significant magnitude and proper phase is confined within the forest extent.

Since the forest is statistically homogeneous along the horizontal dimension and assuming stationarity in the wide sense, the correlation function $C[\widetilde{E}_{jp}(\bar{r}'_1), \widetilde{E}_{jq}(\bar{r}'_2)]$ can be considered a smooth function of the coordinate difference $y'_1 - y'_2$, and the standard deviation function $\sigma[\widetilde{E}_{jp}(\bar{r}')]$ is uniform along the y-axis. Then the stationary phase approximation method [15] can be applied to the integral in equation (4.21). With the stationary phase point at $y'_1 - y'_2 = y$, the integrand terms with multiplier terms or vanish, and equation (4.21) reduces to

$$\begin{aligned}
\langle |\widetilde{E}^d_j(\bar{r})|^2 \rangle = \frac{1}{2\pi k_0} \int_0^H \int_0^H & \frac{e^{jk_e R_1^{sp} - jk_e^* R_2^{sp}} (jk_e R_1^{sp} - 1)(-jk_e^* R_2^{sp} - 1)}{(R_1^{sp} R_2^{sp})^3 (R_1^{sp} R_2^{sp})^{1/2}} \\
& \cdot \Big\{ C[\widetilde{E}_{jz}(y, z'_1), \widetilde{E}_{jz}(y, z'_2)] \sigma[\widetilde{E}_{jz}(z'_1)] \sigma[\widetilde{E}_{jz}(z'_2)] \\
& \cdot [(z - z'_1)(z - z'_2) + (x - x'_j)^2] \\
& + C[\widetilde{E}_{jy}(y, z'_1), \widetilde{E}_{jy}(y, z'_2)] \sigma[\widetilde{E}_{jy}(z'_1)] \sigma[\widetilde{E}_{jy}(z'_2)] \\
& \cdot (x - x'_j)^2 \Big\} dz'_1 dz'_2
\end{aligned} \tag{4.23}$$

where $R_1^{sp} = \sqrt{(x - x'_j)^2 + (z - z'_1)^2}$ and $R_2^{sp} = \sqrt{(x - x'_j)^2 + (z - z'_2)^2}$. Due to variations in particle distribution and density along the vertical dimension, $\sigma[\widetilde{E}_{jp}(z')]$ and $C[\widetilde{E}_{jp}(y, z'_1), \widetilde{E}_{jq}(y, z'_2)]$ are functions of z' over the finite vertical extent of the forest block. Lacking analytical expressions for C and σ, numerical integration must be carried out for equation (4.23).

4.3 Model Validation

In this section, the validity of the SWAP model is examined in two different ways. The first method studies simulation results for red pine stands. The second is a quantitative comparison in which foliage path-loss predictions obtained from the SWAP model are compared against a set of independent experimental data of path-loss through a pecan orchard at 9.6 GHz [26]. Despite the fact that the trees are evenly planted and only a very limited number of measurements at each receiver location are available, very good agreement between the measured results and the model prediction is obtained.

4.3.1 Qualitative Validation of the SWAP Model

Here three sets of simulation experiments are conducted. The single-scattering SWAP model, as shown in Figure 4.5, is first compared with the FCSM model for propagation in forests. Next, the single-scattering SWAP model is applied to forest stands with different tree densities and at different frequencies to examine the dependence of path-loss on these parameters qualitatively. Finally, the multiple-scattering components are included in the SWAP simulations to evaluate their importance in the path-loss estimation. For all simulations a vertically polarized plane wave is normally incident upon a red pine stand which is about 8m tall, having a trunk layer of about 1.2m high, an individual tree crown diameter of approximately 5m and trunk diameter of about 20cm, and several different tree densities. A receiver detecting fields at vertical polarization is placed at a number of locations along the wave propagation direction. A block of the forest, 15m long, 15m wide, and 8m tall, is selected for evaluation of statistical wave propagation parameters. All simulations are performed on a Linux workstation with a 2.4 GHz processor and 1 GB memory.

Figure 4.7 shows the foliage path-loss versus propagation distance in the red pine

stand with a tree density of 0.05 trees/m^2, using the SWAP and the FCSM models at a frequency of 0.5 GHz. The receiver is located 1.5m above the ground, in the crown overlap layer. The simulation results from the FCSM model are based on 40 realizations. As a reference, the coherent power calculated based on Foldy's approximation is also plotted in the figure. Clearly the single-scattering SWAP model provides very accurate results when compared to the FCSM model. The simulation time using SWAP is significantly less than the "brute force" FCSM model. Specifically, running one realization for all receiver locations using the FCSM model took about 2800 seconds and 40 realizations took more than 30 hours of computation time. On the other hand, the computation time to run the SWAP model required only 200 seconds. However, to estimate the behavior of wave propagation inside the forest, 100 Monte-Carlo realizations that took about 8 hours had to be carried out. It should be noted that this Monte-Carlo simulation for SWAP is required once and the results can be reused for simulations of wave propagation through forests with arbitrary distances and receiver heights.

Figure 4.8 shows the foliage path-loss as a function of propagation distance when the SWAP model is applied to the same red pine stand with a tree density of 0.05 trees/m^2 at different frequencies: 1.0 GHz, 2.0 GHz, and 4.0 GHz. Each curve has a knee, the point of slope change where the SWAP model curve starts deviating from the Foldy's path-loss prediction. It can be seen that the knee occurs at a shorter propagation distance as the frequency increases, which indicates that the ratio of incoherent power to coherent power increases with frequency. However, since the coherent mean-field is attenuated faster at higher frequency, the foliage path-loss may still be larger at higher frequency, as seen from the comparison between 1 GHz and 2 GHz data. At larger propagation distances, where the incoherent power dominates the overall received power, the foliage path-loss at higher frequency becomes less than that at lower frequency. For instance, at distances greater than 200m, the foliage

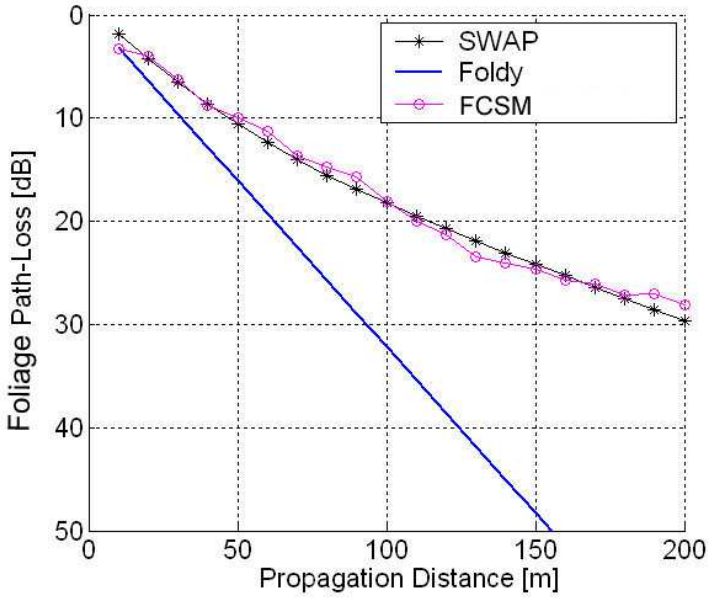

Figure 4.7: Comparison between the single-scattering SWAP and FCSM models (frequency = 0.5 GHz, tree density = 0.05 trees/m^2). The good agreement shows that the single-scattering SWAP is implemented correctly.

path-loss at 4 GHz is less than that at 2 GHz.

A similar result is shown in Figure 4.9 where the SWAP model is applied to red pine stands at three different tree densities (0.05 trees/m^2, 0.1 trees/m^2, and 0.15 trees/m^2) all at 0.5 GHz. This time the receiver is located 0.75m above the ground, in the trunk layer. As expected, higher tree density causes more attenuation and scattering, resulting in more incoherent power relative to coherent power after the wave propagates a long distance inside the forest. This also shows that the foliage path-loss knee occurs at a shorter propagation distance for higher tree densities.

Figure 4.10 shows the results of applying the multiple-scattering SWAP model, as shown in Figure 4.4, to the red pine stand of tree density 0.15 trees/m^2. At this high density the multiple-scattering effects are expected to be significant. Simulation frequency is chosen to be 0.5 GHz and the receiver is located at 1.5m above ground. An obvious decrease of foliage path-loss is observed at range values where the incoherent intensity dominates, beyond about 100m.

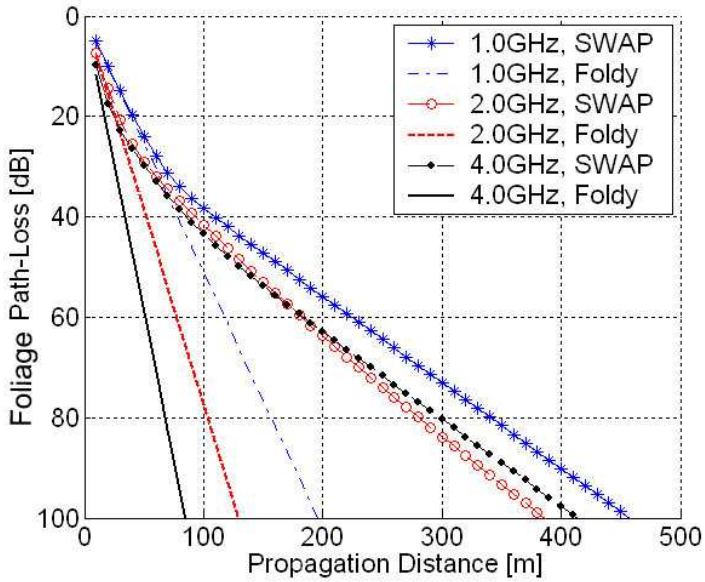

Figure 4.8: Comparison of the single-scattering SWAP model applied at three different frequencies for a tree density of 0.05 trees/m^2. The ratio of incoherent to coherent power increases with frequency.

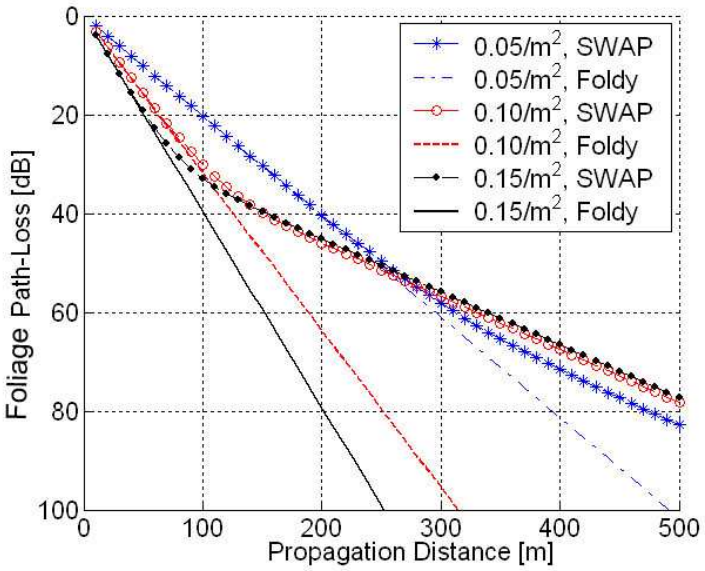

Figure 4.9: Comparison of the single-scattering SWAP model applied to different tree densities at a frequency of 0.5 GHz. The ratio of incoherent to coherent power increases with tree density.

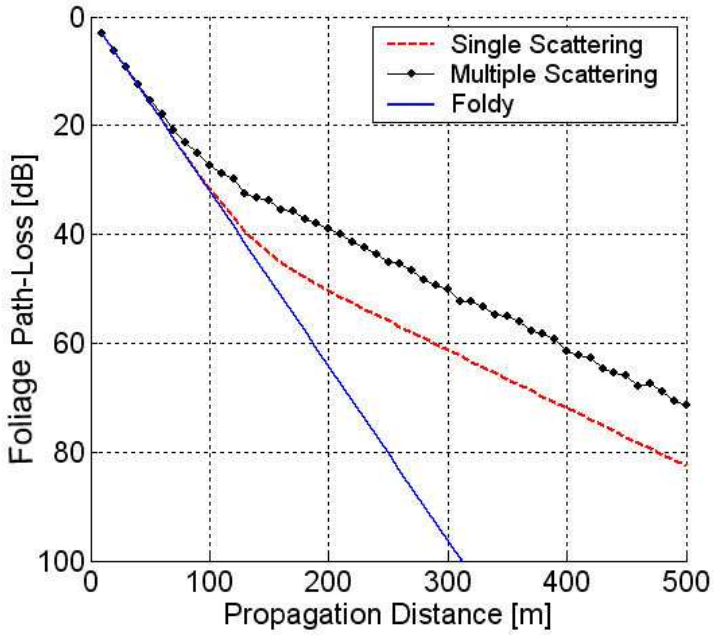

Figure 4.10: Multiple-scattering effects decrease the foliage path-loss through the forest as compared to the single-scattering model (frequency = 0.5 GHz, tree density = 0.15 trees/m^2).

4.3.2 Comparison with Measurements

Schwering *et al.* conducted a propagation measurement through a pecan orchard at 9.6 GHz [26]. Range dependence of the foliage path-loss was obtained for both foliated and defoliated conditions for transmitter-receiver heights of 1, 4, and 6 m, respectively. Despite the random fluctuations of the measured data points, the underlying dual-slope phenomenon can be observed in the measurement results (see Figure 4.13). For each measurement, the transmitter was located 300m away from the front edge of the orchard and the receiver was placed at a height equal to that of the transmitter at different spots into the orchard, as shown in Figure 4.11. The pecan trees are uniformly planted in a grid with about 13m spacing. There is little overlap between neighboring tree crowns. The line of receiver locations passes through the center of a tree row and encounters maximum vegetation density, and hence the coherent field attenuation was maximized as well, especially at the trunk layer where

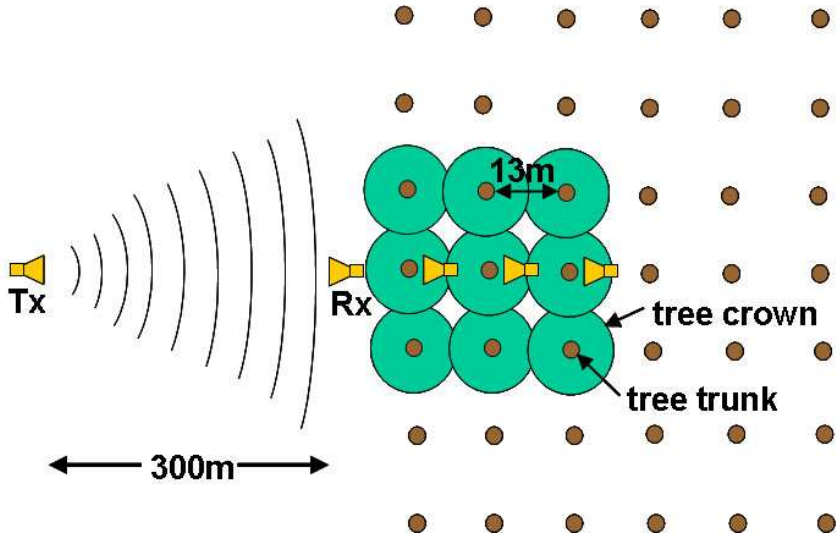

Figure 4.11: Path-loss measurement scenario in a pecan orchard, according to [26].

the shadowing effect is significant. A calibration measurement was first conducted by setting the receiver at the front edge of the orchard to remove the effects of instrument loss and free space (ground present) path-loss. The remaining foliage path-loss can then be modeled as the attenuation of a plane wave propagating through the orchard.

The ground truth for the pecan orchard was described in [26], however it lacks information on average trunk diameter and detailed branching structure, which makes the fractal tree modeling difficult. With the help of pictures of the orchard presented in Schwering's paper and botanical information of the typical pecan tree [56], computer-generated pecan trees out-of-leaf and in-leaf are obtained as shown in Figure 4.12(a)and 4.12(b), respectively. Both trees have a tree height of approximately 9m and a canopy crown diameter of about 13m. The trunk layer height is about 1.5m, although for the in-leaf pecan tree some branches can droop to the 1m level. The trunk diameter is chosen to be 50cm in order to match the coherent field attenuation observed from the measured data.

To apply the SWAP model, a 25m long, 40m wide, and 9m tall block of pecan trees is used for estimating the required statistical wave propagation parameters. About 6

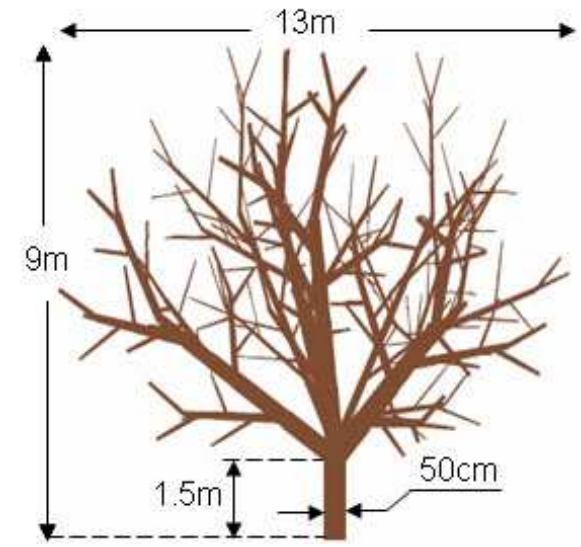

(a)

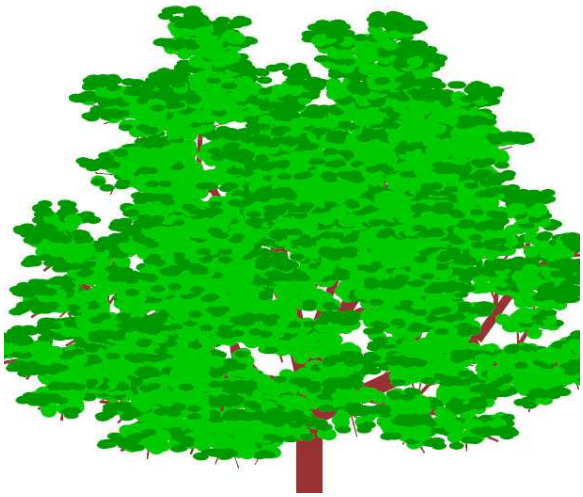

(b)

Figure 4.12: Computer-generated fractal model of pecan trees: (a) out-of-leaf condition; (b) full-leaf condition.

trees are randomly located inside the block. Although this random distribution of tree locations deviates from the uniform plantation of the pecan orchard, the scatterers inside the canopy crown, such as the leaves and branches, should have similar random distributions especially at high frequencies where the size of the scatterers is much larger or comparable to wavelength. The vertical dimension of the block is divided into 4 layers. The depth of each layer from the trunk to the top of the canopy is 1.5, 3.0, 2.5, and 2.0 m, respectively. This way we can distinguish the trunk layer, the two crown layers where the 4m and 6m measurement heights respectively fall into, and the crown top layer where scatterers are relatively sparse. Foldy's propagation constants are first estimated using a number of random tree samples. Field distribution statistics, i.e. the variances and correlation functions, along a vertical line with sample points at half-wavelength spacing in the middle of the output surface of the block is then obtained through a Monte-Carlo simulation of 100 realizations, at which point the convergence of the field statistics is achieved.

Figure 4.13(a) and 4.13(b) illustrate the comparison between SWAP model simulation and Schwering's measured data of the foliage path-loss at 9.6 GHz versus the number of trees obstructing the signal path (see Figure 4.11) at the heights of 4 and 6 m respectively. The pecan trees are in a defoliated state. Figure 4.14(a) and 4.14(b) show similar results for the pecan orchard in full-leaf. The measured data shows some fluctuation along an underlying dual-slope trend due to the fact that the signal path was fixed during each measurement and no averaging on independent spatial samples was carried out. All simulations assume V-V polarization in accordance with the measurement scenario, i.e. the transmitter sends a vertically polarized wave and the receiver detects vertical polarization as well. As seen from these plots, the multiple-scattering SWAP model predicts the foliage path-loss reasonably accurately. For instance, the simulated foliage path-loss slope agrees well with the measurement. Specifically, the path-loss slope changes more abruptly for the foliated state. Approx-

imately 5 dB more path-loss in the foliated state compared to the defoliated state is predicted as well (notice the difference of the propagation distance ranges in Figure 4.13 and 4.14. By including higher order multiple-scattering effects which is important in this scenario, the path-loss estimation agrees more closely to the measured data.

It is worth noticing that the difference between single-scattering and multiple-scattering estimations is much larger for the defoliated state. This is because of the less coherent attenuation experienced by the multiple scattered fields when leaves are not present as a major scattering and absorption source. The comparison for the scenario where transmitter and receiver are located at the trunk layer (e.g. height of 1m) has not been carried out due to the difference of trunk locations in the SWAP simulation and the real measurement site. As mentioned before, the trunks are in rows and the transmitter and receiver are placed along a row. However this is not a limitation of the SWAP model since the tree locations are easily adjustable, merely a limitation of this specific implementation of this orchard in our model.

4.4 Conclusions

A statistical wave propagation (SWAP) model has been introduced in this paper that provides an accurate and time-efficient simulation tool for wave propagation over long distances within forested environments. SWAP uses an existing wave theory model (FCSM) and applies it to a representative block of the forest to pre-compute the statistical wave propagation parameters. These parameters are then used in conjunction with a network approach to calculate the total power at the receiver. The computation time is significantly reduced. Modeling accuracy is enhanced by including multiple-scattering components. Three sets of simulation experiments are conducted on a red pine stand to examine the validity of the SWAP model qualita-

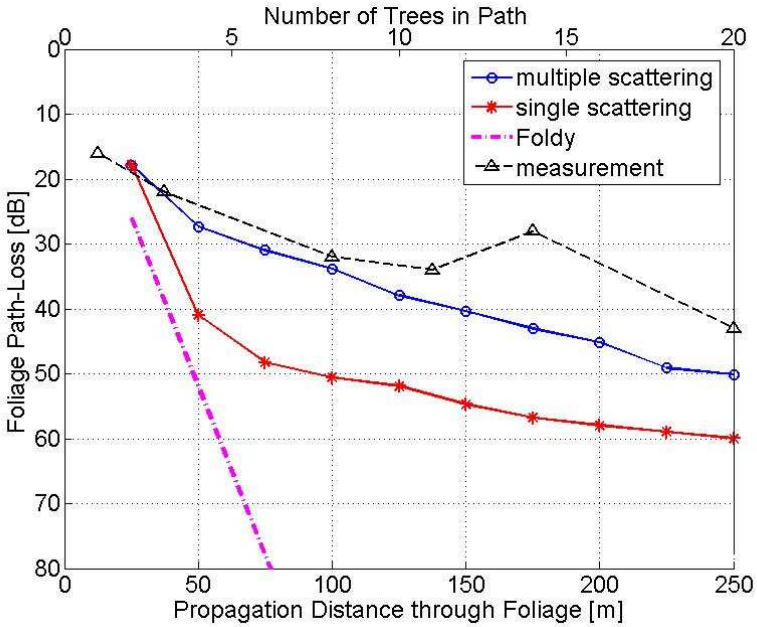

(a)

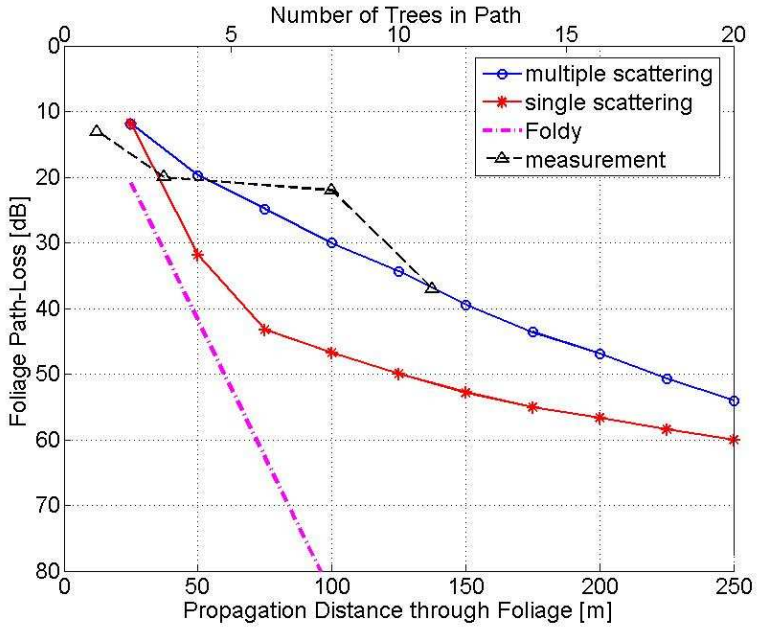

(b)

Figure 4.13: Comparison between SWAP model simulation and measurement data, (a) receiver height at 4m; (b) receiver height at 6m. Pecan trees are out-of-leaf. Note that the multiple-scattering SWAP model results are very close to the measurements.

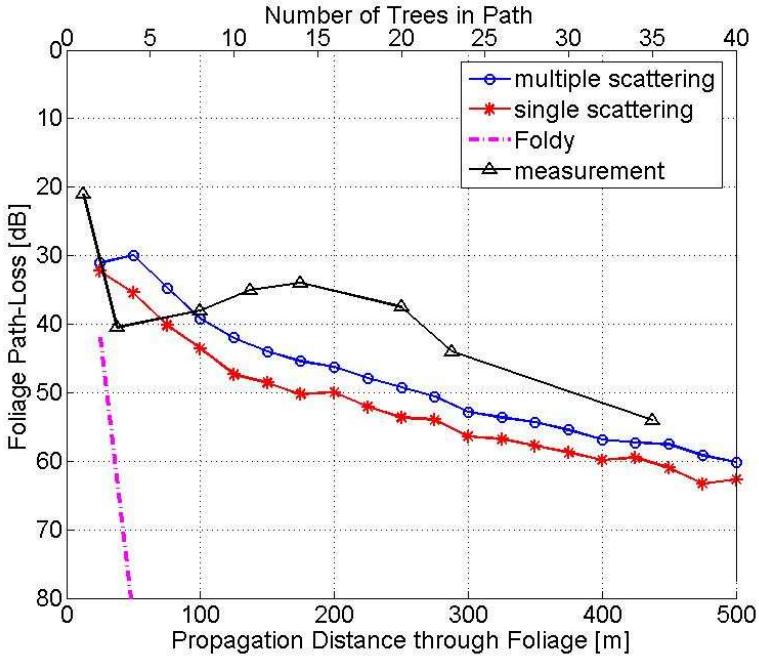

(a)

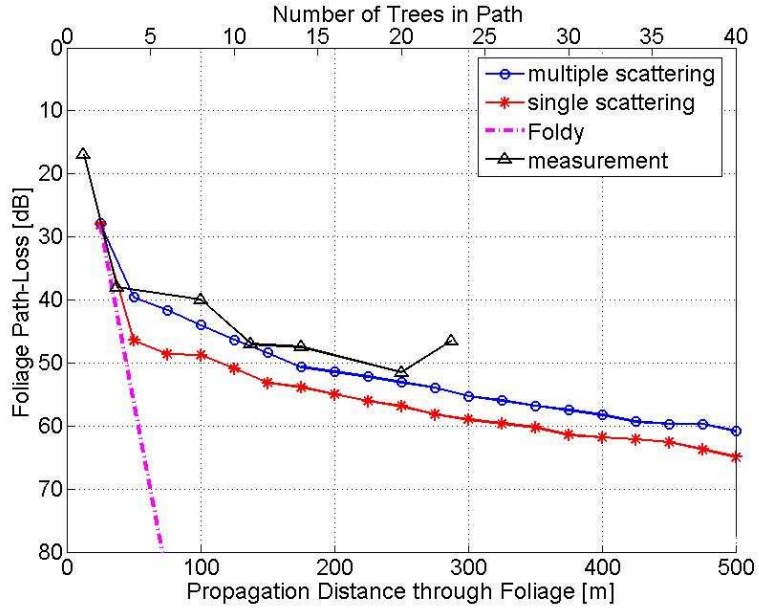

(b)

Figure 4.14: Comparison between SWAP model simulation and measurement data, (a) receiver height at 4m; (b) receiver height at 6m. Pecan trees are in full-leaf.

tively. Independent measured data at X-band for path-loss through a pecan orchard is predicted by the SWAP model accurately. Further improvement of the SWAP model can be made by including multiple-scattering among scatterers within each forest block, and by accounting for backscattering mechanisms which are neglected for the time being due to their relatively small contributions. The SWAP model is also applicable to inhomogeneous forests containing different tree species by including different block types throughout the forest.

CHAPTER 5

MiFAM: A MACRO-MODEL OF FOLIAGE PATH-LOSS

5.1 Introduction

In the previous chapter, an accurate and time-efficient foliage path-loss model, SWAP, was introduced. As discussed, SWAP is based on applying a state-of-the-art wave propagation model, FCSM, to a block of forest in order to estimate the wave propagation behavior in foliage over a long distance in a computationally tractable manner. FCSM and SWAP are research codes, however, and are difficult for ordinary users who do not possess in-depth knowledge of the codes to use. Although SWAP is capable of predicting the path-loss through foliage of arbitrary parameters, at any desired frequency, or over any radio link distance, its accessibility and operability to a wide range of users are rather limited. A macro-model using simple mathematical expressions while maintaining the accuracy of the original model is desired. Such a macro-model can be extracted from a large number of simulations using the original codes. As mentioned earlier, this procedure is similar to developing empirical models from real measured data, but has the advantage of greater flexibility and more general applicability. For example, the empirical Weissberger model [7] for foliage path-loss only involves the operating frequency as a single parameter besides the propagation distance; the aforementioned macro-modeling methodology can include

all parameters of the forested environment and radio link attributes. Additionally, this macro-modeling methodology is more cost-efficient as compared to conducting physical experiments.

In this chapter, an accurate foliage path-loss macro-model called the Michigan Foliage Attenuation Model (MiFAM) is developed. First, a physics-based parametric model for the foliage path-loss which is capable of predicting the dual-slope path-loss behavior is selected. Then, the most influential foliage and radio system parameters and their effects on the parameters of the aforementioned parametric model are determined through sensitivity analysis. In addition, allometric models for tree species are used to minimize the number of foliage parameters. Next, a multiple linear regression is performed to relate the parametric model parameters to the foliage and radio system parameters quantitatively. In what follows, details of the development of MiFAM are provided and an example of MiFAM applied to red maple trees is presented.

5.2 Michigan Foliage Attenuation Model

5.2.1 Parametric Model for Foliage Path-Loss

The dual-slope foliage path-loss as a function of distance has been reported in the literature; the results have been obtained mainly through experimental efforts [20, 25, 26]. The physics of wave attenuation in a highly scattering environment can be attributed to two phenomena: 1) attenuation due to absorption, and 2) attenuation along the direction of propagation due to scattering. As explained in the previous chapter, the initial attenuation rate at short propagation distances corresponds to the absorption and scattering of the coherent mean-field by foliage particles along the direction of wave propagation. On the other hand, scattering by foliage particles can provide power gain as well, by redirecting part of the incident power (either directly

from the transmitter or scattered from other particles) towards the receiver. This mechanism contributes to the so-called incoherent power at the receiver. After a certain distance in the random medium, the coherent power decays to insignificant levels and only the incoherent power resulting from scattering remains. In this region, which is usually far away from the transmitter, attenuation can only be attributed to absorption as it is expected that what is lost due to scattering can be regained through further scattering in an average sense. Therefore the attenuation rate of the dominant incoherent power is significantly different from that of the coherent power, giving rise to the dual-slope path-loss curve as a function of distance.

A simple parametric model capable of explaining such phenomenon is given by [15]

$$PL = -10\log_{10}\left\{(1-q)e^{-(\sigma_a+\sigma_s)d} + qe^{-\sigma_a d}\right\} \tag{5.1}$$

where PL stands for foliage path-loss (in dB) as a function of the propagation distance d (in meters) inside the foliage. σ_a and σ_s are power attenuation rates due to absorption and scattering, respectively, and q is a parameter related to the degree of scattering in the medium. The combination of σ_a, the absorption coefficient, and σ_s, the scattering coefficient, leads to the extinction coefficient which is the same as the attenuation rate of the coherent power. At short distances, i.e. for small d, the first term in (5.1) is dominant (q is usually a very small quantity), resulting in path-loss given by

$$PL \approx -10\log_{10}\left\{e^{-(\sigma_a+\sigma_s)d}\right\}. \tag{5.2}$$

This agrees with the observation that path-loss is dominated by the coherent power attenuation at short propagation distances. At large distances, i.e. for $d \gg 1$, (5.1) can be approximated by

$$PL \approx -10\log_{10}\left\{qe^{-\sigma_a d}\right\}, \tag{5.3}$$

indicating that the path-loss curve slope is only proportional to σ_a, or the attenuation

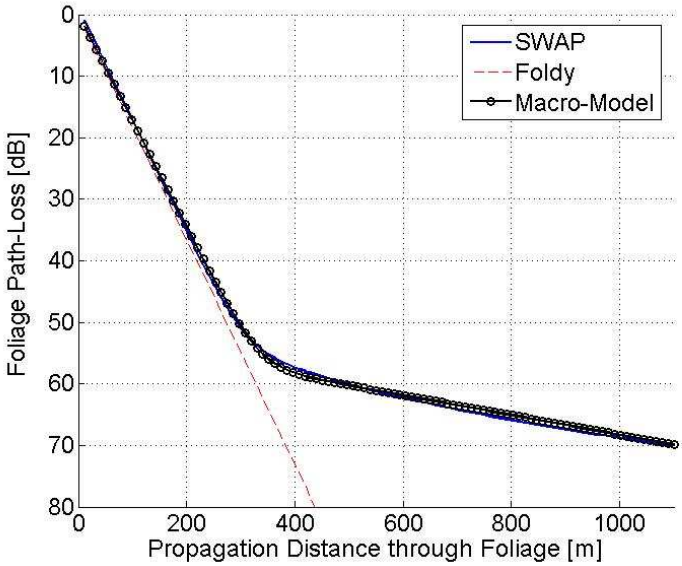

Figure 5.1: A 3-parameter macro-model explaining a foliage path-loss curve computed from the SWAP model.

is due only to absorption. In the direction of propagation the power lost due to scattering is further scattered back into that direction by other scatterers. From (5.3), one observes that q contributes to an offset in the path-loss value when the expression is evaluated for $d = 0$. Ishimaru interprets q as the fraction of total scattered power within the receiving angle of the receiver in an isotropic random medium [15]. An accurate physical meaning of q for more complicated media such as a forest, however, is not as straightforward. Figure 5.1 shows how well the 3-parameter parametric model can fit the path-loss curve computed from the SWAP model. Coherent power attenuation based on Foldy's approximation is also shown. By selecting proper values for σ_a, σ_s, and q, the 3-parameter model completely agrees with the SWAP model. It is worth mentioning that some other models with adjustable parameters, such as the Non-Zero Gradient model [22], may be adopted as well, although numerical examination shows inferior agreement with the simulation result of the SWAP model.

5.2.2 Model Parameters as Functions of Foliage & Radio System Parameters

In the previous section, a simple 3-parameter foliage path-loss model was shown to be adequate for capturing the path-loss behavior in a forest environment. It is obvious that with different foliage and radio system scenarios, the foliage path-loss curve varies, hence, the model parameters must change accordingly. Generally, the specific scenario can be described with a number of foliage and radio system parameters. Foliage parameters include the structural and forest stand parameters, as well as the vegetation dielectric parameters. The structural parameters which determine the tree structures include

- tree height (t_h)
- trunk diameter at breast height (dbh)
- crown-to-trunk ratio (ctr)
- branching angle (b_a)
- branch density (b_d)
- leaf density (l_d)
- cone angle (c_a, only for coniferous trees),

and the forest stand parameters are

- tree species
- tree number density (t_d).

The parameters that determine the dielectric constants of foliage particles and the underlying ground are

- wood moisture (m_w)
- leaf moisture (m_l)
- soil moisture (m_s).

The empirical dielectric mixing formulae reported in [106] are used to calculate the dielectric constants of vegetation and soil. The foliage parameters can be determined

either from the ground truth measurement of a desired site or simply from estimated values reported in literature for different forest stands. The radio system parameters are as follows:

- operating frequency (f)
- transmitter-receiver height (H)
- transmitter-receiver polarization (pol).

The purpose of macro-modeling is to relate the path-loss model parameters (σ_a, σ_s, q) to the foliage and radio system parameters. Considering the large number of foliage and system parameters, extensive sensitivity analysis is required to establish such relationships. Since path-loss is an average quantity resulting from the statistical average of many quantities, it is expected that the path-loss model parameters be a smooth function of the foliage and radio system parameters. That is, no singularities or resonance are expected for the functional forms chosen to relate the model parameters to the foliage and system parameters.

The most general relationship form or relating function may be written as

$$\mathbf{Y} = \mathbf{g}(\mathbf{X}) \tag{5.4}$$

where $\mathbf{Y}$, the vector of path-loss model parameters, is given by

$$\mathbf{Y} = \begin{pmatrix} \sigma_a \\ \sigma_s \\ q \end{pmatrix}, \tag{5.5}$$

$\mathbf{X}$, the input vector containing all pertinent foliage and system parameters, is given by

$$\mathbf{X}^t = [x^{(1)}, x^{(2)}, \cdots, x^{(k)}], \tag{5.6}$$

where the superscript $(j), j = 1, 2, \cdots, k$, stands for the j^{th} foliage/system parameter, and $\mathbf{g}$ is a multivariate vector function. In order to obtain the function $\mathbf{g}$, sensitivity analysis is carried out for each individual foliage and system parameter. First, a centroid value is assigned to each foliage and system parameter. Then, for the parameter under study, its value is varied within a certain range around its centroid, while other parameters remain at their respective centroid. Using this set of foliage and system parameter values, one runs the SWAP model to obtain a corresponding foliage path-loss curve, from which the three model parameters are retrieved by standard curve-fitting process. Repeating this previous step for different values of the parameter under study, one can obtain a number of data points relating each model parameter and the parameter under study. From these data points, the relationship between each model parameter and the parameter under study can be extracted through curve-fitting.

The most simple relationship between the model parameters and the foliage/system parameters is a linear function, i.e.

$$\mathbf{Y} \simeq \mathbf{Y_0} + \mathbf{A} \cdot \mathbf{X} \tag{5.7}$$

where $\mathbf{Y_0}$ corresponds to a constant term; $\mathbf{A}$ contains the linear coefficients, and is given by

$$\mathbf{A} = \begin{pmatrix} a_1^{(1)} & a_1^{(2)} & \cdots & a_1^{(k)} \\ a_2^{(1)} & a_2^{(2)} & \cdots & a_2^{(k)} \\ a_3^{(1)} & a_3^{(2)} & \cdots & a_3^{(k)} \end{pmatrix}.$$

$\mathbf{Y_0}$ and $\mathbf{A}$ can be obtained by first generating a number of data samples of $(\mathbf{X}, \mathbf{Y})$ from the SWAP model and then using standard multiple linear regression technique to retrieve the linear coefficients relating $\mathbf{X}$ and $\mathbf{Y}$. The combination of equations (5.1) and (5.7) essentially provides a macro-model for the foliage path-loss prediction, which

will be referred to as the Michigan Foliage Attenuation Model (MiFAM). Compared to Weissberger's empirical model where frequency is the only parameter for path-loss measurements, MiFAM is obviously much more accurate and general.

A subtle point in the construction of MiFAM is that not all the foliage/system parameters are continuous variables, e.g. the transmitter and receiver polarizations are discrete. For these parameters, they are not included in $\mathbf{X}$. Instead, different sets of $\mathbf{Y_0}$ and $\mathbf{A}$ are developed at different values of such parameters, e.g. the V-V and H-H polarizations. Some continuous variables may be treated similarly in order to simplify the macro-model. For example, although the transmitter or receiver height can vary continuously, the layered structure of the foliage makes its effect dependent on other parameters, such as tree height and crown-to-trunk ratio. A reasonable approximation is to discretize this parameter by placing the receiver or transmitter in the crown layer or the trunk layer. Other examples of parameters that can be discretized are the branch and leaf densities. These are continuous variables that are difficult to measure in practice. They are also discretized into different categories, e.g. less dense, dense, and denser, and separate sets of $\mathbf{Y_0}$ and $\mathbf{A}$ are provided, one for each category. It should also be mentioned that since the fractal trees forming the virtual forest environment are species-dependent, MiFAM is species-dependent as well.

The development of MiFAM requires a large number of simulations and amount of curve-fitting, which are by no means an easy task. However, once such a macro-model is obtained, it will greatly benefit many end users in terms of providing accurate path-loss model with significant time savings. In what follows, a detailed example of MiFAM for a common deciduous tree species is provided.

5.3 MiFAM for Red Maple Forest

Red maple, one of the most prevalent tree species in northern America, belongs to the deciduous tree category. Its structural architecture is well studied and the corresponding L-systems "DNA" file has been developed in the Radiation Laboratory at the University of Michigan. Based on the realistic-looking fractal tree models generated from such DNA file, and the well-developed SWAP path-loss model, the MiFAM macro-model can be obtained through the methodology described in the previous section. In this section, the development of MiFAM for red maple forest will be demonstrated. This macro-model targets the UHF (ultra-high frequency) band ($300 - 1100$ MHz). It is noted that a number of cell phone communication systems such as AMPS, GSM, and IS-95 [57] are specified to operate in this band.

5.3.1 Sensitivity Analysis

In this section, sensitivity analysis for the red maple tree is carried out in order to construct the foliage path-loss macro-model. The model provided in this section is for defoliated trees. Path-loss models for fully foliated trees can be developed in a similar manner with the inclusion of additional foliage parameters related to the leaves, such as leaf density and moisture. In this example, branch density is selected to be dense, the transmitter and receiver are placed in the crown layer and V-V polarization is chosen. Figure 5.2 shows computer-generated fractal red maple trees in the defoliated state with varying branch densities. Except for the leaf parameters, the remaining foliage/system parameters to be included in $\mathbf{X}$ and their centroid values are listed in Table 5.1.

Simulation results indicate that variations of the crown-to-trunk ratio parameter ctr, the branching angle b_a, and the soil moisture m_s have little effect on the model parameters σ_a, σ_s, and q. Therefore, they are excluded from the foliage/system pa-

Table 5.1: Foliage/system parameters and their centroid values to be used in the MiFAM model for red maple trees

tree density (m^{-2})	tree height (m)	trunk diameter (cm)
t_{d0}	t_{h0}	dbh_0
0.05	10	15
crown-to-trunk ratio	branching angle (deg.)	wood moisture (g/g)
ctr_0	b_{a0}	m_{w0}
4	22	0.5
soil moisture (cm^3/cm^3)	frequency (MHz)	
m_{s0}	f_0	
0.18	700	

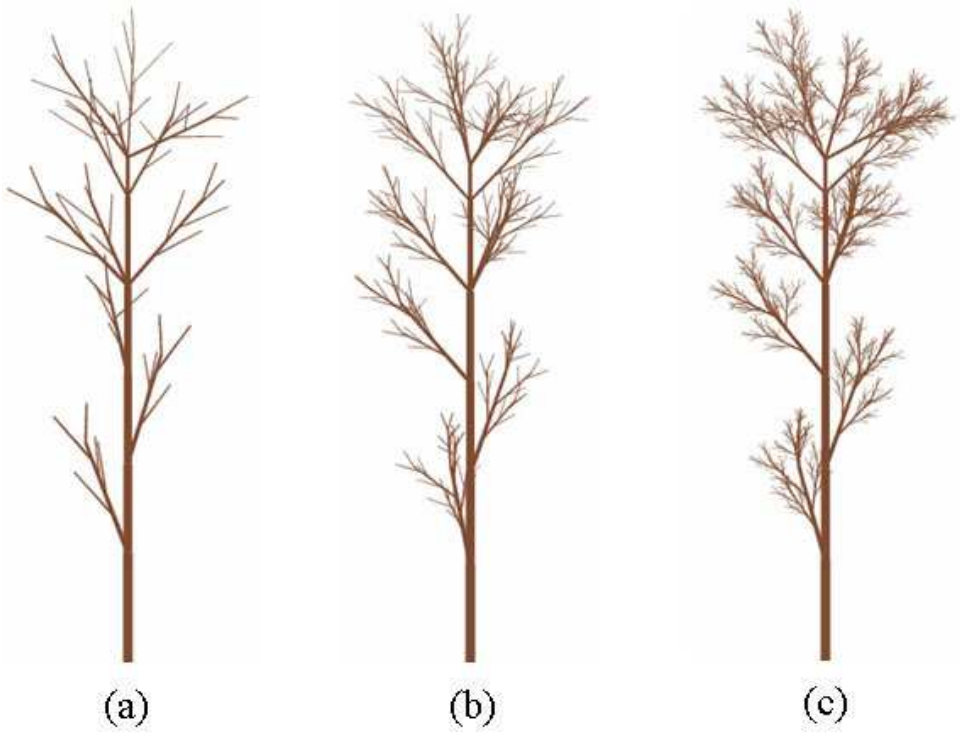

Figure 5.2: Fractal red maple trees with different branch densities, (a) less dense; (b) dense; (c) denser.

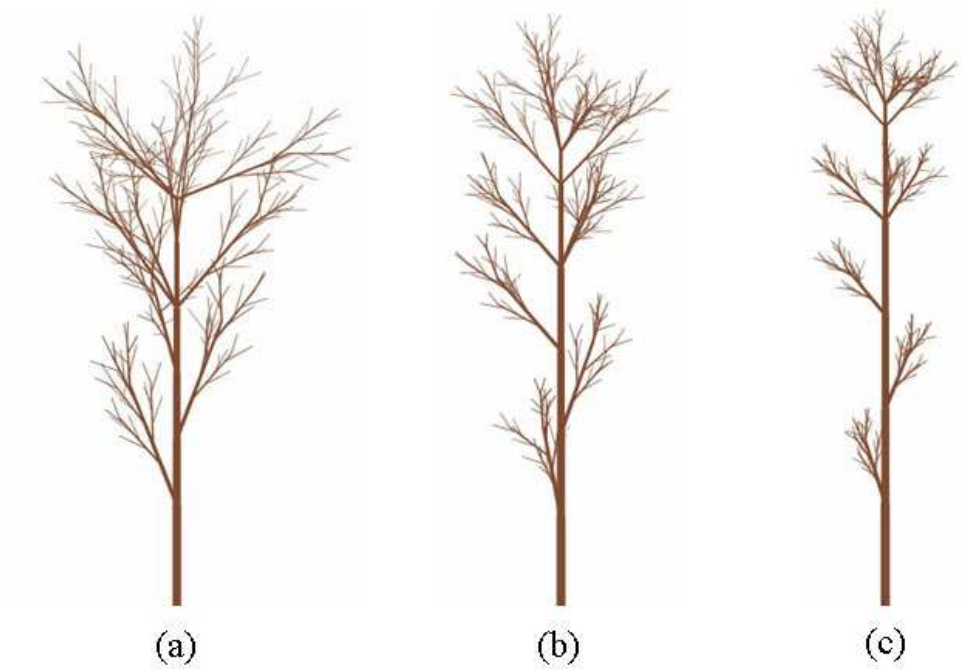

Figure 5.3: Fractal red maple trees corresponding to different tree densities, (a) 0.025 trees/m^2; (b) 0.05 trees/m^2; (c) 0.1 trees/m^2.

rameter vector $\mathbf{X}$. The remaining five parameters are of importance and are described in detail in what follows.

Tree Density

The foliage crowns of adjacent deciduous trees generally occupy the space in between the trees but do not extend past their immediate neighbor. In this case there is a simple relationship between the crown diameter (C_{dia}) and the tree density (t_d) given by

$$C_{dia} \simeq \sqrt{1/t_d}. \tag{5.8}$$

Figure 5.3 shows three fractal red maple trees corresponding to different tree densities, 0.025 trees/m^2, 0.05 trees/m^2, and 0.1 trees/m^2. The related crown diameters are about 6.3m, 4.5m, and 3.2m, respectively. The distinction of tree structures with various crown coverage is clearly observed.

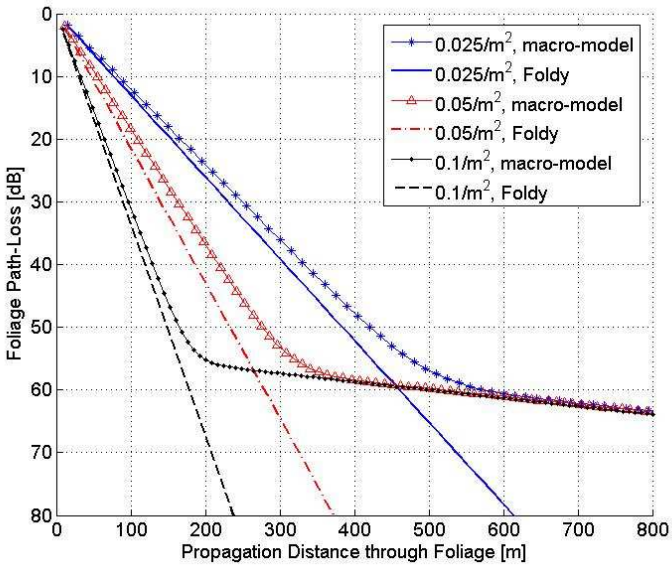

(a)

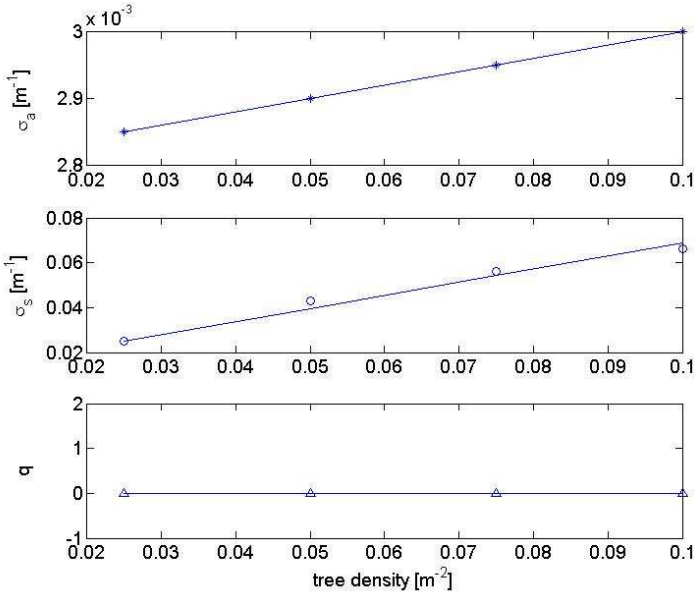

(b)

Figure 5.4: Simulation results for different tree densities of red maple forests, (a) foliage path-loss curves; (b) path-loss model parameters as functions of tree density.

Figure 5.4(a) plots three sets of foliage path-loss curves with respect to the different tree densities; as can be seen, the structural differences and tree number density significantly affect the foliage path-loss. Each set includes the total power path-loss curve calculated by the macro-model whose parameters are determined by curve-fitting the path-loss simulated from the SWAP model; the coherent power path-loss curve based on Foldy's approximation is included as a reference. Figure 5.4(b) plots the values of the three macro-model parameters σ_a, σ_s and q for the different tree density values. It is clearly observed that linear functions are sufficient to predict the behavior of σ_a, σ_s and q over a very wide range of tree density values.

Tree Height

Figure 5.5 shows three fractal red maple trees with different tree heights, 5m, 10m, and 15m. It is clear that shorter trees appear to have more branches since the same number of branches are confined into a smaller volume. As shown in Figure 5.6, both σ_a and σ_s decrease as the tree height increases. Again a linear relationship exists between each model parameter and the tree height.

Trunk Diameter

Figure 5.7 shows three fractal red maple trees with trunk diameters, 10 cm, 15 cm and 20 cm. The value of the trunk diameter sets the thickness of the branches in the tree but does not affect the branching architecture. Figure 5.8 provides the simulation results of foliage path-loss at different values of trunk diameter. It is observed that σ_a, σ_s and q are sensitive to the trunk diameter in a linear manner.

Wood Moisture

The wood moisture parameter describes the gravimetric water content in the wood of the tree trunk and branches. Therefore, it also determines the dielectric properties,

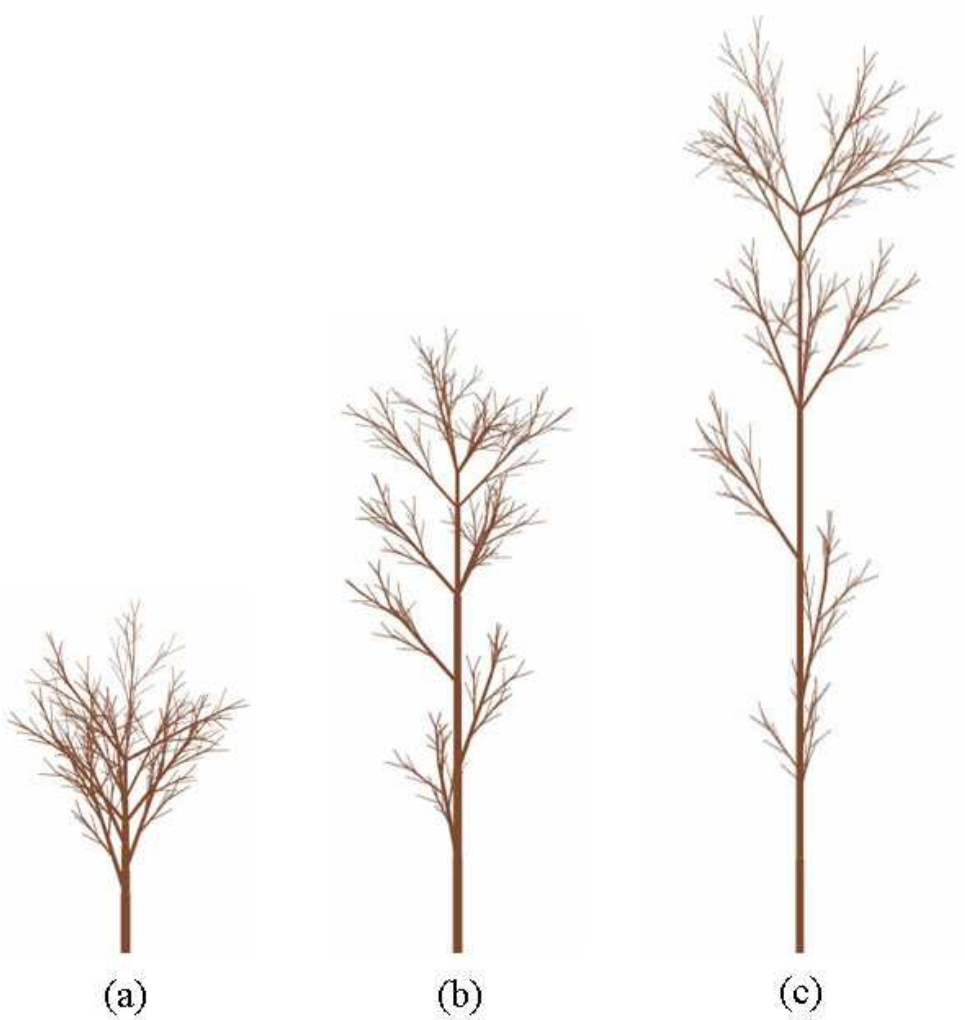

Figure 5.5: Fractal red maple trees with different tree heights, (a) 5m; (b) 10m; (c) 15m.

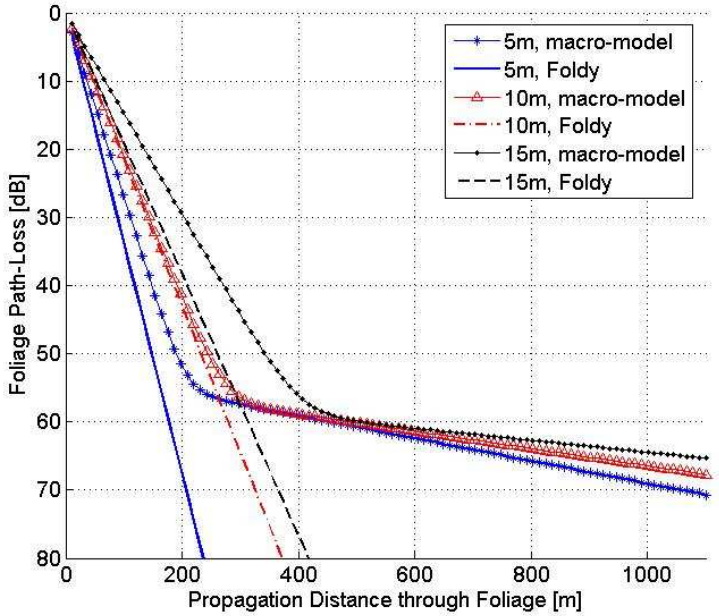

(a)

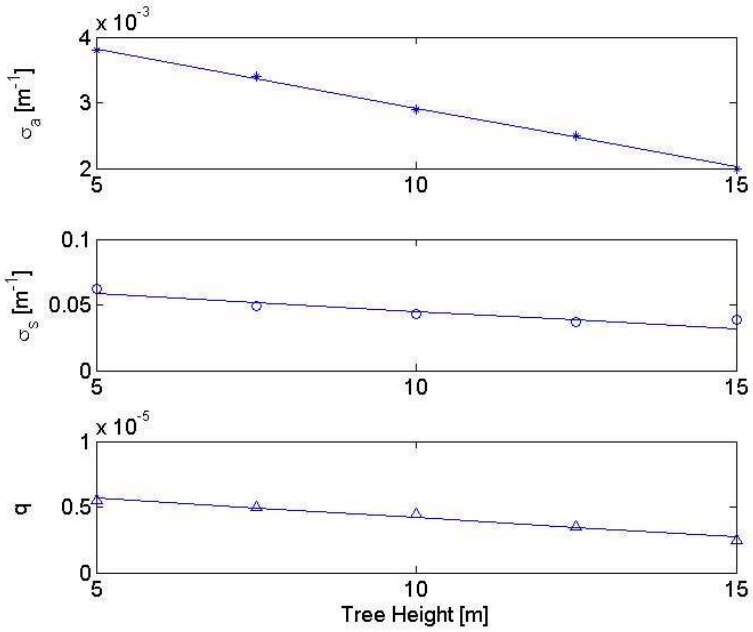

(b)

Figure 5.6: Simulation results for different tree heights of red maple forests, (a) foliage path-loss curves; (b) path-loss model parameters as functions of tree height.

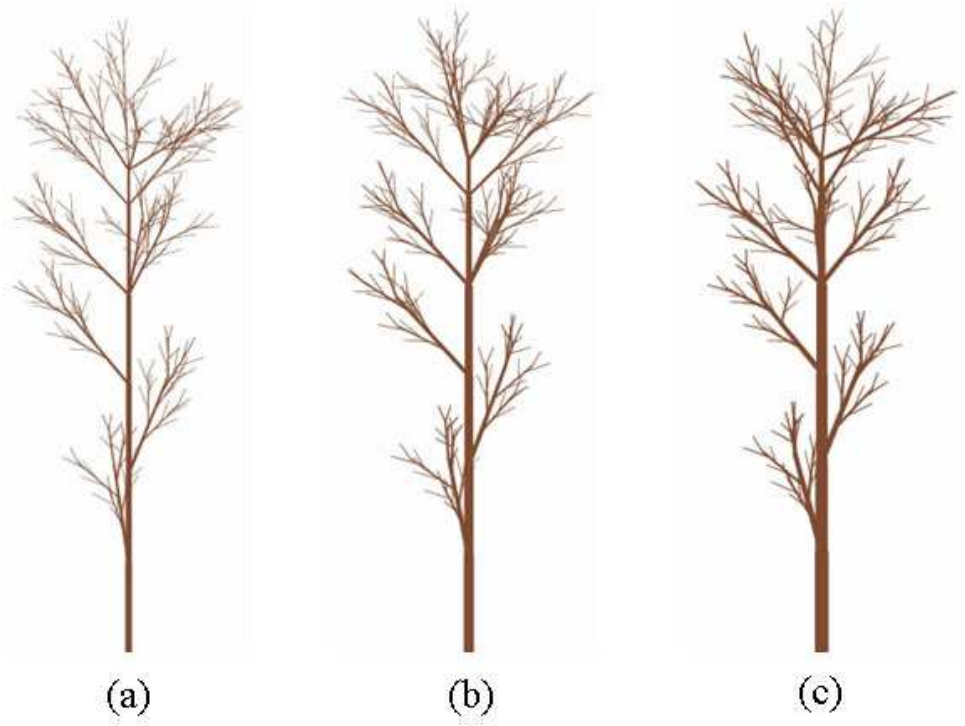

Figure 5.7: Fractal red maple trees with different trunk diameters, (a) 10 cm; (b) 15 cm; (c) 20 cm.

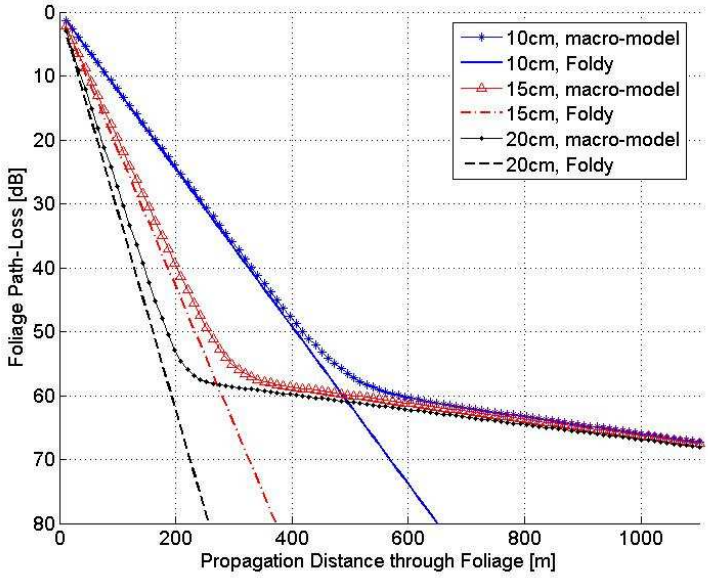

(a)

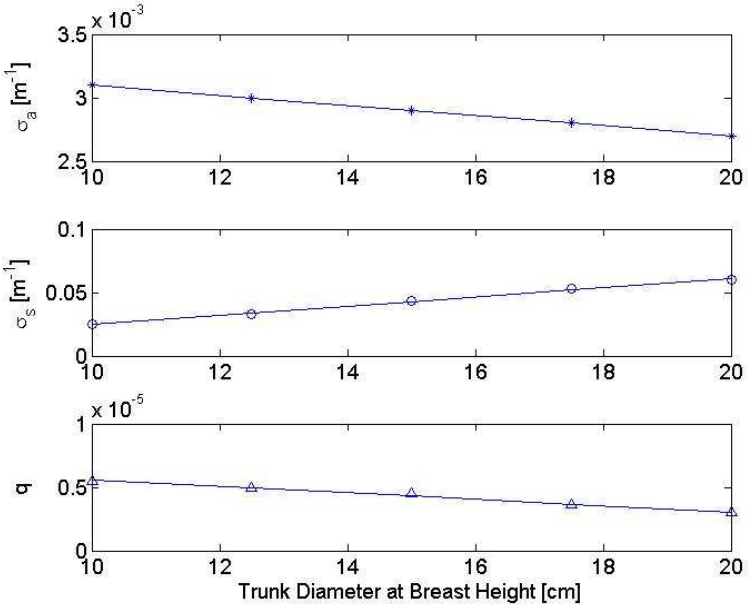

(b)

Figure 5.8: Simulation results for different tree trunk diameters of red maple forests, (a) foliage path-loss curves; (b) path-loss model parameters as functions of trunk diameter at breast height.

and affects the way the wood absorbs and scatters the propagating wave. Figure 5.9 provides the simulation results of foliage path-loss at different values of wood moisture. The linear relationships between model parameters and the wood moisture is clearly observed. Wood moisture is usually difficult to measure. A suggested value for the red maple trees is 0.5 grams of water per gram of wood.

Frequency

Frequency is an important factor because it affects the scattering and absorption behavior of foliage particles interacting with the propagating waves. The dielectric constants of the foliage particles as well as the soil ground are frequency-dependent, although such dependence is not considerable over a small range of frequencies. Figure 5.10 provides the simulation results of foliage path-loss at different UHF band frequencies. As seen in the figure, the three model parameters all vary linearly with the frequency.

5.3.2 Evaluation of MiFAM Coefficients

The above sensitivity analysis results for five important foliage/system parameters showed that simple linear relationships exist between each individual model parameter (σ_a, σ_s, and q) and those five foliage/system parameters. Therefore a standard multiple linear regression technique can be applied to obtain the matrices $\mathbf{A}$ and the vector $\mathbf{Y_0}$ in equation (5.7). The results are given by

$$\mathbf{A} = \begin{pmatrix} 0.002 & -1.8e\text{–}4 & -4.0e\text{–}5 & -0.001 & -1.5e\text{–}6 \\ 0.481 & -0.0024 & 0.0036 & 0.05 & 1.6e\text{–}5 \\ 1.95e\text{–}6 & -3.0e\text{–}7 & -2.56e\text{–}7 & -5.0e\text{–}6 & -3.0e\text{–}9 \end{pmatrix}, \tag{5.9}$$

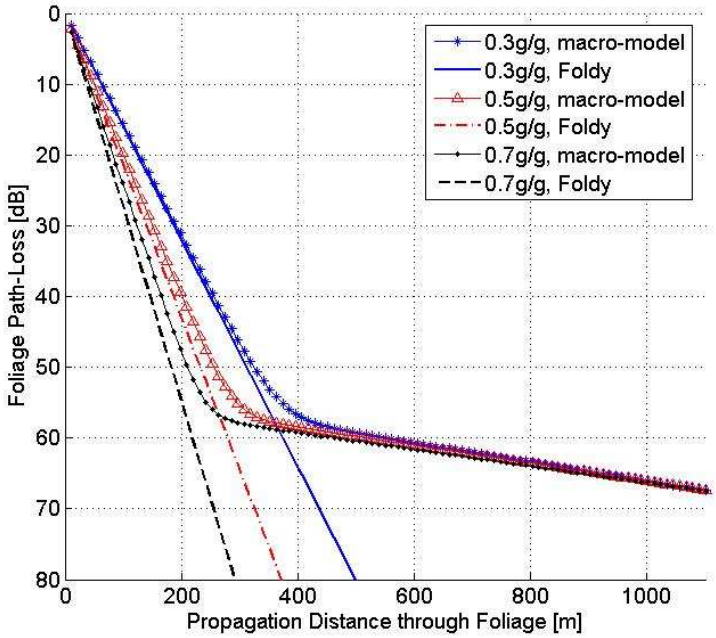

(a)

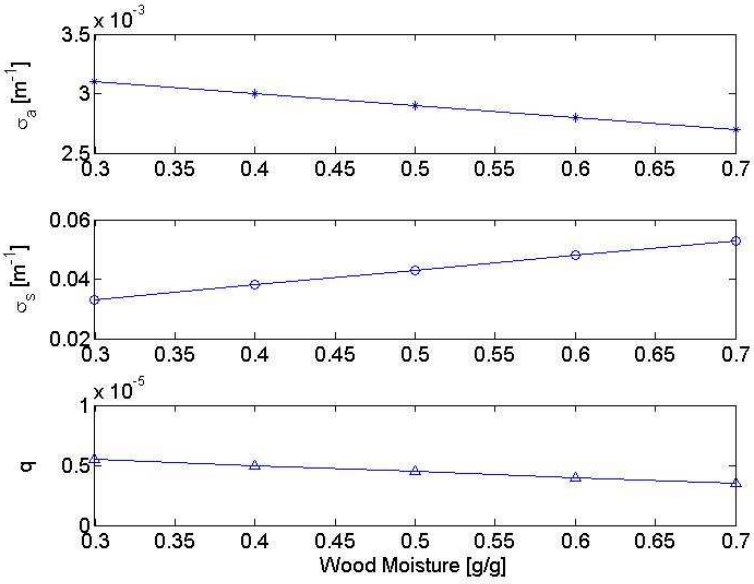

(b)

Figure 5.9: Simulation results for different wood moisture of red maple forests, (a) foliage path-loss curves; (b) path-loss model parameters as functions of wood moisture.

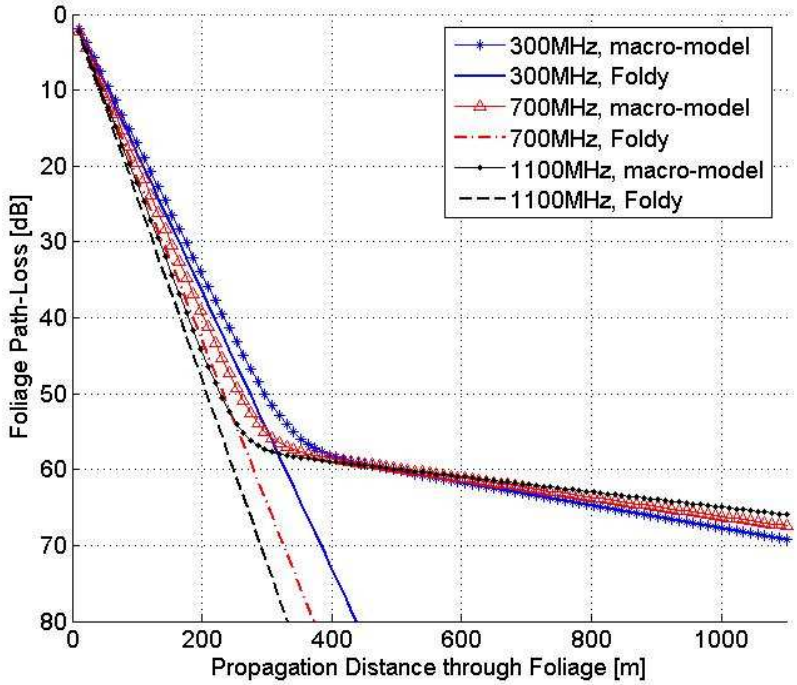

(a)

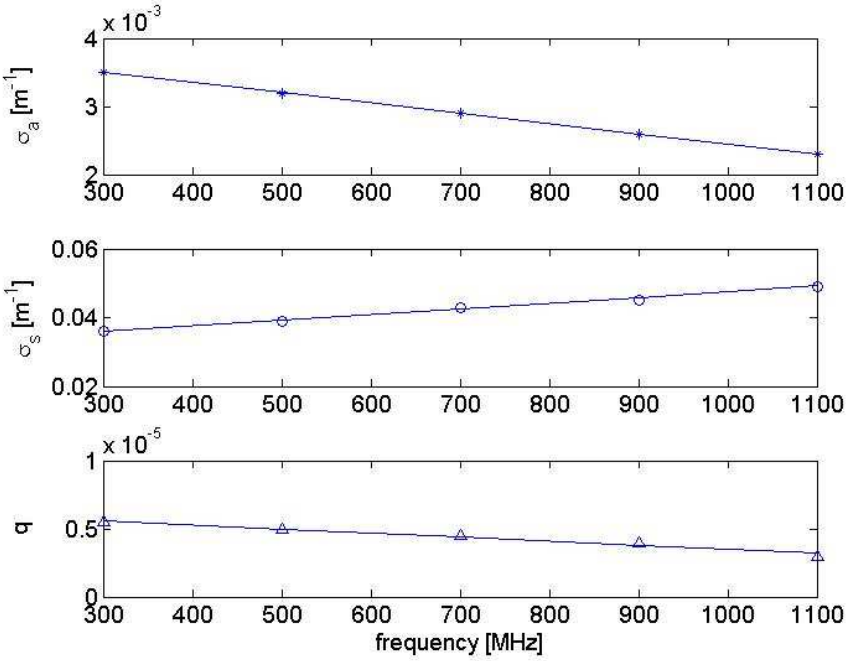

(b)

Figure 5.10: Simulation results for red maple forests at different frequencies, (a) foliage path-loss curves; (b) path-loss model parameters as functions of frequency.

and

$$\mathbf{Y_0} = \begin{pmatrix} 0.00675 \\ -0.0475 \\ 0.0000157 \end{pmatrix}. \tag{5.10}$$

Also the foliage/system parameter vector and its centroid value are given by

$$\mathbf{X} = \begin{pmatrix} t_d \\ t_h \\ dbh \\ m_w \\ f \end{pmatrix}, \quad \mathbf{X_0} = \begin{pmatrix} 0.05 \\ 10 \\ 15 \\ 0.5 \\ 700 \end{pmatrix}. \tag{5.11}$$

Figure 5.11 shows the fitting performance of the multiple linear regression for σ_a, σ_s, and q. The "*" markers represent data points with values of σ_a, σ_s, or q computed from both SWAP and MiFAM with the evaluated $\mathbf{A}$ and $\mathbf{Y_0}$. As shown in the figure, those "*" markers are concentrated around a diagonal line, indicating that the model parameters computed by MiFAM agree with the original values computed by SWAP quite well. This proves the successful evaluation of the MiFAM coefficients.

5.3.3 MiFAM Validation Against SWAP

Equations (5.1), (5.7), and (5.9)−(5.11) establish the complete MiFAM for foliage path-loss through red maple forests. Users can plug in the specific values of the five foliage/system parameters in their wave propagation scenarios and compute the foliage path-loss at certain propagation distances. As a validation of MiFAM, a number of sets of foliage/system parameters are chosen and they are used both in the SWAP model and the MiFAM. The resulting path-loss model parameters from SWAP and MiFAM are then compared against each other. Notice that the foliage/system parameters selected here are independent sets from those used in evaluating MiFAM

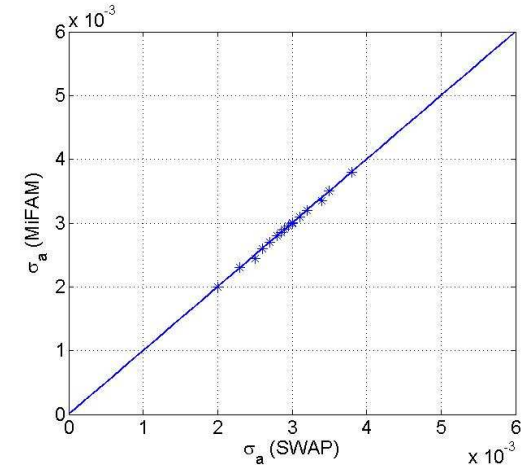

(a)

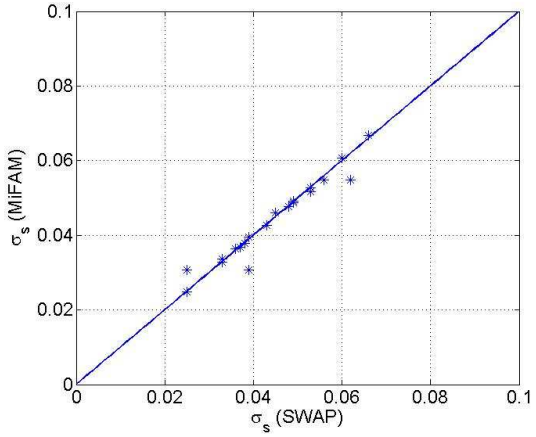

(b)

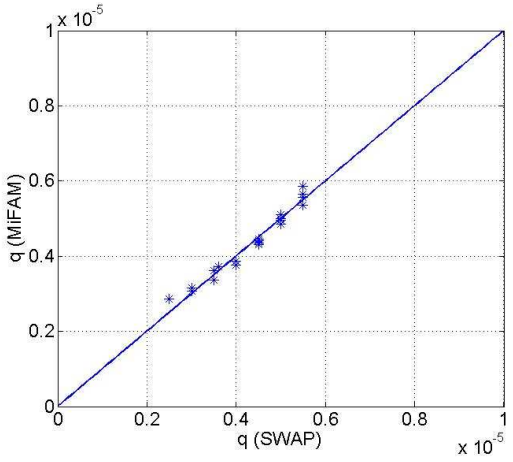

(c)

Figure 5.11: Results of multiple linear regression, (a) fitting performance for σ_a; (b) fitting performance for σ_s; (c) fitting performance for q.

coefficients. Figure 5.12 shows the simulation results, which is similar to Figure 5.11. Good agreement between MiFAM and SWAP model is observed, which provides a quantitative validation of the developed MiFAM for red maple forest.

5.4 Conclusions

In this chapter, a macro-modeling technique for foliage path-loss prediction is presented. It is based on sensitivity analysis of foliage and radio system parameters using the well-developed SWAP model. First, a simple mathematical expression with three model parameters is established to explain the dual-slope foliage path-loss as a function of propagation distance. Then each of these model parameters is related to a number of foliage and radio system parameters through the extensive sensitivity analysis and multiple linear regression. Once these relationships are obtained, the user can plug in their specific foliage/system parameters and compute the three model parameters from which the foliage path-loss curve is determined. This foliage path-loss macro-model is referred to as the Michigan Foliage Attenuation Model (MiFAM). The model is tree species and radio system dependent. An example of MiFAM for defoliated red maple forest is provided for certain transmitter-receiver polarization and over a certain frequency range. This MiFAM model is also validated against additional independent simulation results from the SWAP model. As a final comment, it is worth mentioning that because of the generality of the SWAP model on which it is based, the macro-model described in this chapter has no fundamental limitation in predicting the foliage path-loss for any radio system inside any arbitrary forest environment.

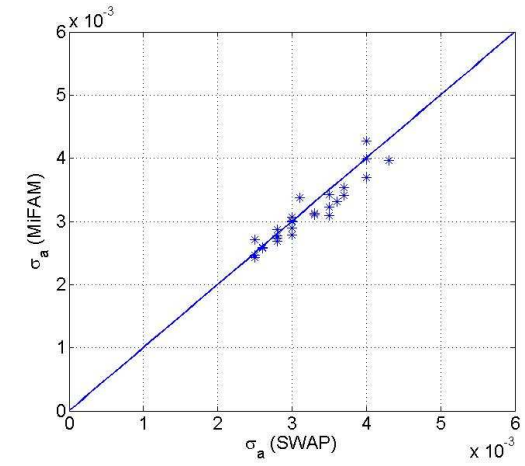

(a)

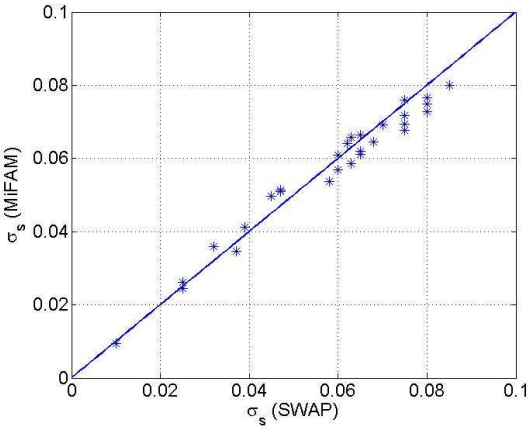

(b)

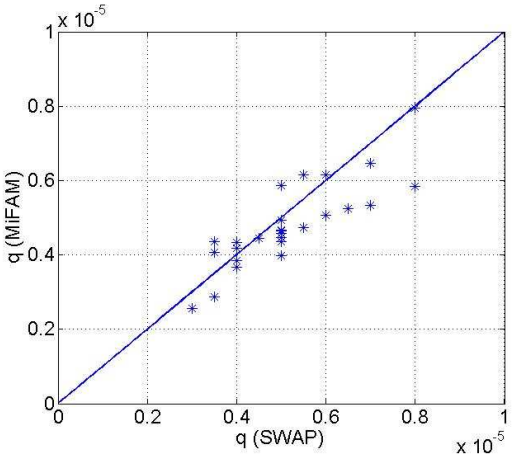

(c)

Figure 5.12: Validation of MiFAM against SWAP model, (a) comparison of σ_a; (b) comparison of σ_s; (c) comparison of q.

CHAPTER 6

PHASE CALIBRATION OF LARGE-REFLECTOR ARRAY USING LEO TARGETS

6.1 Introduction

Exploration of solar system has long been a human aspiration. With the advent of launch vehicles, communications, lightweight and compact electronics, remote sensing tools, and robotics this dream has become a reality over the past several decades. In this endeavor the space agencies' goal has always been to minimize mission cost and complexity while simultaneously increase functionality. Current plans for space exploration missions call for sending spacecraft farther and farther away from the earth. At the same time the demand for communication throughput has increased while the existing communication link between distant spacecrafts and earth ground stations are very weak. There is an urgent requirement for great enhancement of such a radio link. Enough effective isotropic radiated power (EIRP) must be provided for the wireless communication channel so that sufficient signal-to-noise ratio (SNR) can be achieved to ensure the desired communication capacity. Antenna arrays consisting of large reflector antennas have already been employed at ground stations to communicate with spacecraft during the missions, such as the Very Large Array (VLA) in New Mexico, U.S. [58]. However, their up-to-date usage is primarily limited to downlink

operation where phase coherence of signals at all array elements can be achieved by *a posteriori* signal processing using recorded data such as images transmitted back from a spacecraft. The uplink operation such as telemetry of navigation and mission command still relies on single large reflector antennas at ground stations. For example, the 70-m antenna of NASA (National Aeronautics and Space Administration) DSN (Deep Space Network) is the primary resort for emergency uplink contact with lost spacecraft. However, due to its aging effect and power as well as size limitation, it needs to be replaced or upgraded in the near future. Instead of building new colossus reflectors which is extremely expensive, arraying a number of smaller size reflector antennas would produce the same performance at a fraction of the cost [32], provided that their phase coherence can be assured in the uplink operation mode.

As mentioned earlier the downlink signal processing technique is not applicable to uplink arraying. In addition, the phase center of a large reflector antenna cannot be easily determined to the desired accuracy at the operation spectrum (X- and Ka-band). Therefore an external calibration using a calibration target is necessary. Due to the large size of array elements and their sparse distribution, the calibration target has to be located very distant from the array so that it appears in the main beams of all array elements. And it is desirable that the terrestrial environment does not cause severe interference with the calibration. Furthermore, Earth rotation and spacecraft movement mandates the calibration at all array attitudes. Considering all these requirements, one finds the existing low earth orbit (LEO) orbiters promising candidates for calibration targets, for their remoteness in respect to the surface of the earth, abundance, and their ability to supply multiple calibration opportunities at different array orientations. More importantly, they are free to use. Although launching new LEO micro-satellites becomes more and more affordable nowadays, it may still cost millions of dollars per launch. The trade-off of such a cost-free is that these existing targets generally do not have the resource to transmit particular

beacon signals for the array calibration purpose, in other words, they appear as passive targets. Therefore an active array calibration approach must be employed.

In this chapter a radar calibration method for a sparsely distributed large-reflector phased array is proposed. Such an approach is based on the concept of phase conjugation and calibrates the phase center and instrument phase shift altogether using a group of LEO orbiters as calibration targets. In what follows, the proposed architecture for an uplink phased array and the corresponding calibration method are presented in Section 6.2. Section 6.3 studies the array dynamics as a function of Earth spin and orbital movement. The optimal orbit and required number of in-orbit LEO calibration targets for providing frequent calibration opportunities is also investigated by employing an aerospace simulation software package STK (Satellite Tool Kit) [60]. In Section 6.4 an array gain performance analysis of the proposed array system in terms of the residual phase errors of array elements is presented using a statistical modeling approach. Finally in Section 6.5, concluding remarks and comments are provided.

6.2 Coherent Phased Array System

Figure 6.1 shows a simplified block diagram of the proposed array system. In this scheme, the array elements are capable of operating in both transmit and receive modes at the same frequency band. To calibrate the phase of the array elements, one antenna is used as a transmitter illuminating an in-orbit calibration target and all array elements are used as receivers. In this case the target behaves as the source for all receivers. To maintain the system coherence, a common phase-stable local oscillator (LO) and identical T/R (transmitter/receiver) amplifier modules are employed. Each T/R module is composed of two low-loss, high-power, and high-isolation SPDT (Single Pole Double Throw) switches which are connected to the input and output of

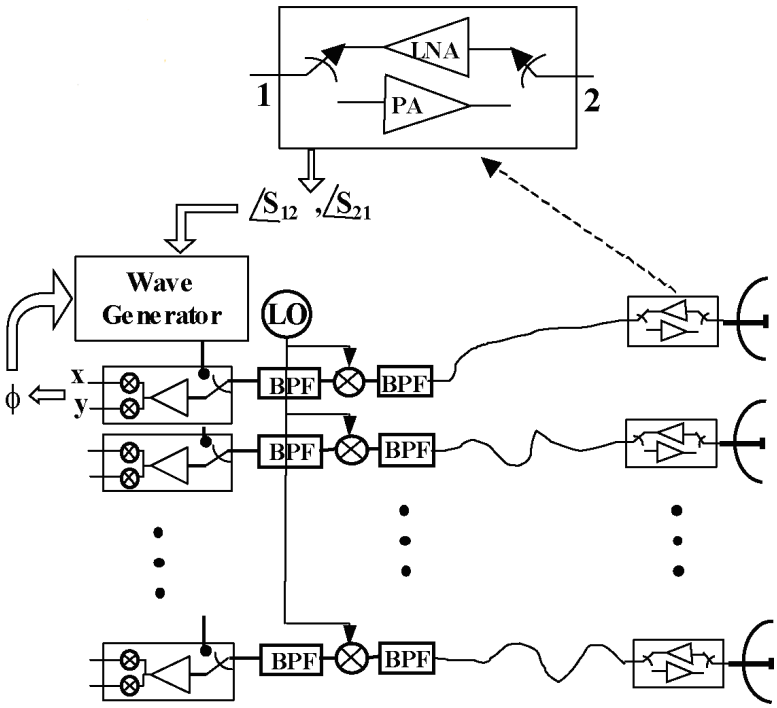

Figure 6.1: Simplified block diagram of proposed array system and calibration procedure.

a low noise amplifier (LNA) and a power amplifier (PA), as shown in Figure 6.1.

The received backscatter signals at each antenna are carried to a control room, and down-converted to an IF frequency in a mixer using the common LO signal. The outputs of all mixers are filtered, amplified, and coherently detected using quadrature receivers where the magnitude and phase of the signals are measured and stored. For array downlink operation (receive mode), phase compensation at each element is applied by subtracting the corresponding stored phase values from the received signals. For uplink operation (transmit mode), according to the concept of phase conjugation, the array can focus back at the source location once the array phase distribution in transmission is the negative of that of the received signals during the calibration. In practice, an IF signal with phase conjugation can be generated in a waveform generator, and then up-converted using the same mixer and LO. To accommodate this phase conjugation scheme, the components along the signal path of each array

element must be reciprocal (like the transmission lines) or commonly shared by all elements (like the LO). The transmission lines carrying signal from each antenna to the control room should be very low-loss and phase-stable. Because of their rigidity, low-loss property at high frequencies and relatively low transmission phase variation with temperature, metallic waveguides may be used. However, waveguides are dispersive and for certain signal bandwidth and transmission line length, a matched filter may be required to compensate for the frequency dispersion. Alternatively air-filled rigid coaxial lines or fiber optics may be selected instead. For active devices such as mixers and amplifiers, the phase shifts must be pre-characterized. For instance, if the amplifier T/R modules are not identical, then their transmission phase characteristics must be measured *a priori* and be used during phase conjugation processes. Basically a correction must be made so that the sum of the phases of S_{12} and S_{21} of all T/R modules become identical.

It is worth mentioning that the calibration procedure only aligns the carrier phase at each array element. The true-delay synchronization of modulating pulses at each element must also be taken into account. For example, as shown in Figure 6.2, pulse #1 and #2 are the modulating signals at two array elements. Although the phases of their carriers (the underlying sinusoidal curves) are perfectly aligned through calibration, the timing asynchronization of these two pulses causes information loss for $\Delta\tau$ duration out of the total pulse duration τ. Signal delay circuits are therefore needed to correct for the asynchronization $\Delta\tau$. Basically $\Delta\tau$ comes from the path-length difference between signals of different array element. With enough accuracy in the knowledge of such path-length differences, the effect of $\Delta\tau$ can be eliminated. For instance, through GPS [59] measurements of the antenna locations, the path-length differences from different antennas to the spacecraft can be determined within meter-level accuracy, corresponding to time delay of nanoseconds, which is generally insignificant for throughput of megabytes per second.

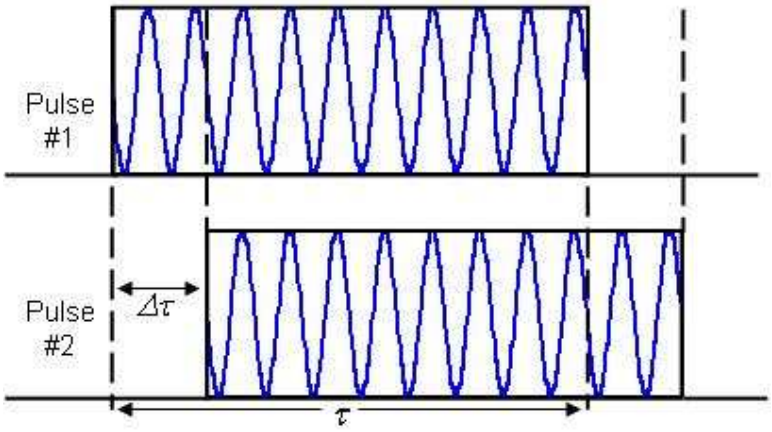

Figure 6.2: Pulse asynchronization between array elements.

In the calibration procedure described so far, the calibration target must be in the far-field of each element but can also be in the near-field region of the array. In most practical situations, array focusing is required at infinity (far-field), but in this case it is often impossible to place the calibration target in the far-field. For example the far-field distance of an array occupying an area of *1* km $\times$ *1* km at 7.2 GHz and 35 GHz is *48,000* km and *233,333* km respectively. As to be shown later, the gain drop for a near-field focused array may be compensated by employing an algorithm that adjusts the differences between near-field and far-field focusing. Therefore the appearance of LEO orbiting targets in the array near-field, generally several hundred to a few thousand kilometers above the earth, does not prevent them from being considered proper candidates of calibration targets. As mentioned earlier, Earth's rotation adds significant complexity to the operation of large uplink arrays since the array has to be calibrated for different antenna attitudes. This obviously raises the question of what are the best orbits and how many in-orbit calibration targets are needed to cover the required aspect angles. In the following section this issue is considered in more details, and the dynamics of the array with respect to the in-orbit calibration targets and a deep space communication probe is examined.

6.3 Array Dynamics and Calibration Using In-Orbit Targets

During a single overpass, an in-orbit target, depending upon its altitude and orbit inclination, is observable by the array at azimuth and elevation angles that may be quite different from those needed to point at a deep space spacecraft traveling in the plane of solar system. In fact during each overpass, an in-orbit target can produce a calibration opportunity for only one direction. Also the overall array phase stability dictates how often the array would require calibration and hence the number of in-orbit targets. In order to quantify the required orbits, the number of calibration targets, and the intervals required to fulfill the required calibrations, a realistic scenario is considered next.

To study the complex relative motion of the earth, calibration targets, and the deep space spacecraft, an aerospace software package, known as STK [60], is used throughout. With its powerful analytical engine, STK computes and provides visualization of various time-dependent information for satellites and other space objects, including orbit/trajectory ephemeris, acquisition times and angles, sensor coverage, etc. Using this software Figure 6.3 shows the pointing angles of the ground station antenna to the spacecraft and the range of the spacecraft during a half-day period. The elevation angle is defined to be the angle between the pointing direction and the plane tangential to the earth at the location of the ground station. The azimuth angle is defined in that tangential plane with 0° corresponding to the local North direction. In Figure 6.3, **R** represents the moment when the spacecraft is rising from horizon in view of the ground station antenna, **O** represents when the spacecraft is almost overhead of the ground station, and point **S** represents the spacecraft setting below the horizon. Figure 6.4 shows the 3D view of this tracking period. The spacecraft is orbiting in the ecliptic plane, which intersects the earth equator plane with an angle of 23.6° (the earth inclination angle). Due to the earth's spin, the ground station moves

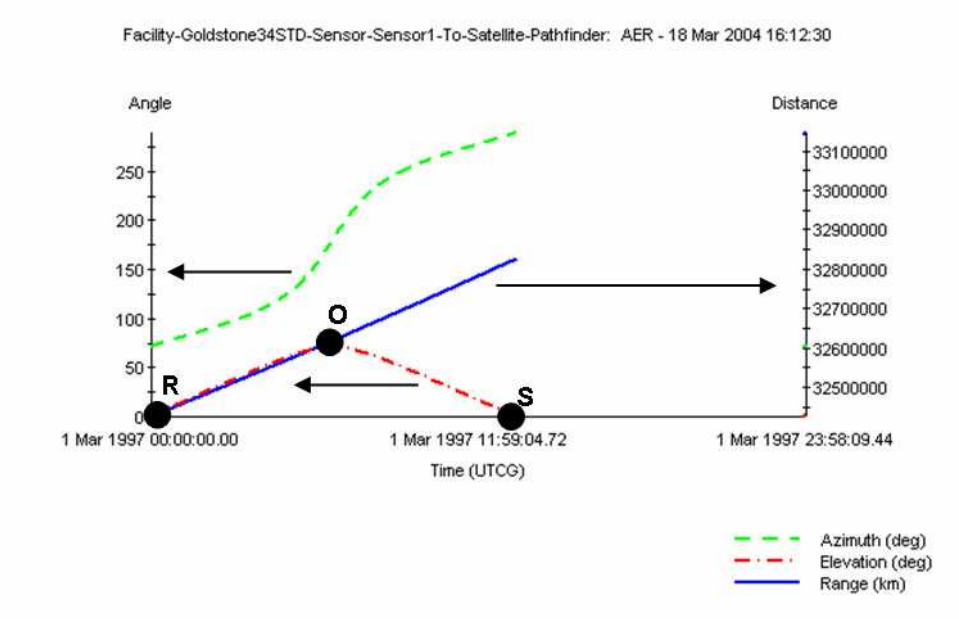

Figure 6.3: Pointing angles of the ground station antenna and the range of spacecraft from Earth versus time.

from point **R** to **O** then to **S**, and changes its pointing angles to track the spacecraft. The pointing vectors intersect a celestial sphere with some altitude (e.g. 500 km) above the earth surface. The intersecting points (including **R'**, **O'**, and **S'**) make up a projection curve on the celestial sphere surface. Ideally, one would like to place in-orbit calibration targets along this projection curve. However, without spending significant energy, maintaining such position is practically impossible. Therefore the array phase calibration needs to rely on system repeatability, in other words the locations of phase centers of the antennas for a given set of azimuth and elevation orientation angles remain the same as a function of time. Hence the calibration can be done *a priori* at different instances where the tracks of in-orbit targets such as a number of LEO satellites intersect the projection curve on the celestial sphere. The number and the orbits of the LEO satellites must be designed in such a way to ensure a complete and frequent intersection.

To examine the track crossing of a LEO satellite with the projection curve, the

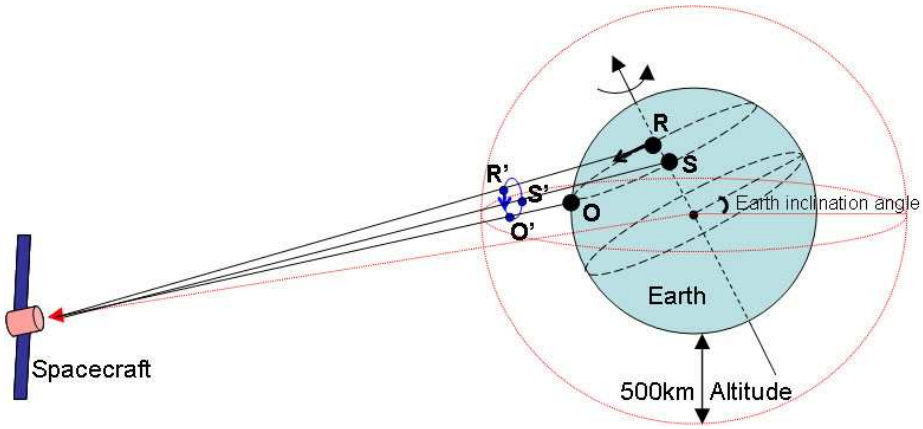

Figure 6.4: 3D view of the ground station tracking the spacecraft.

temporal azimuth and elevation angles of array pointing direction can be represented parametrically in the azimuth and elevation plane. The parametric plots of the array pointing direction to the spacecraft and to a LEO satellite on a circular orbit with altitude of 500 km and inclination angle of 68.5° are shown in Figure 6.5 for a one-day duration. The circle symbols on the dash-lines record the pointing angles to the LEO at a 60-second interval during the period when the antenna can "see" the LEO. And the intersection points A, B, C, D, E, and F provide six calibration opportunities.

For missions with long durations, calibration points over an area in the azimuth-elevation plane must be determined. In order to cover all pointing angles in a relatively short period of time, many LEO satellites at different planes, i.e. different inclination angles and RAAN (Right Ascension of Ascending Node), are required. By optimal design of the LEO satellites orbits, one can use the minimum number of LEO's to cover all points with a specified frequency. The parameters that can be manipulated in the optimization include the inclination angle, the altitude (for circular orbit) or apogee and perigee (for elliptical orbit), and number of satellites. As an example, the five parametric lines in Figure 6.6 shows the pointing angles of a California DSN array to a deep space spacecraft at five different days with an interval of a month (first day of March, April, May, June, and July in 1997). Observation points from

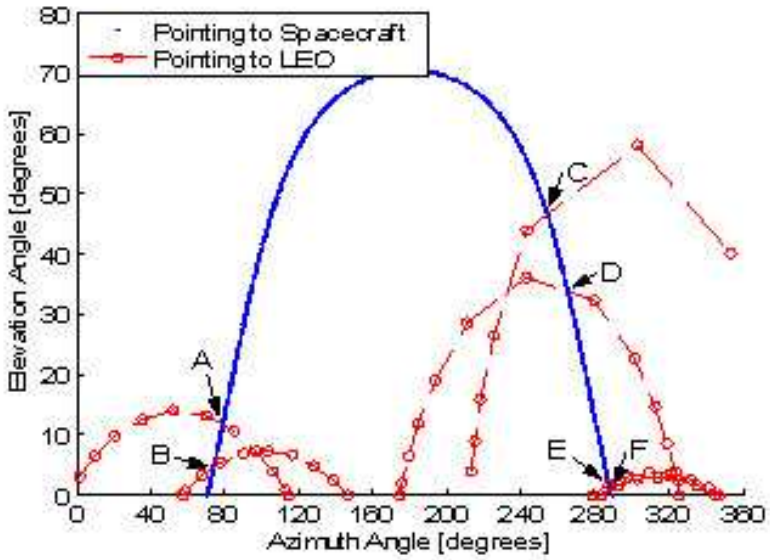

Figure 6.5: Antenna pointing angles to spacecraft and to a LEO satellite for one-day period.

the same array to LEO satellites must cover the area between the innermost and outmost lines. In the following, the LEO orbit is chosen as circular with an altitude of 2000 km. The altitude of 2000 km is chosen because the LEO moves slower and allows for enough time to mechanically steer the antennas between different calibration angles. Of course the signal-to-noise ratio (SNR) is another factor determining the altitude, as will be discussed later. Observation angles of the array 60 seconds apart for a single day will be displayed. Depending on the number of satellites and the required number of calibration points (required pointing angle resolution), the entire calibration may take more than a day. The pointing angle resolution is dictated by the array elements mechanical stability in maintaining antenna phase center as the antenna moves. First, 24 LEO satellites orbiting in a plane with RAAN = 0° and equally spaced are used. The simulation results for 30.6° and 37.5° plane inclination angles are shown in Figure 6.6(a) and 6.6(b), respectively, where the LEO targets in the plane of 30.6° inclination provide calibration opportunities (indicated by markers) covering most of the spacecraft tracking zone with relatively high resolution, except

for some low elevation points which can be covered by the LEO targets in the plane of 37.5° inclination. A combination of LEO targets at 30.6° and 37.5° inclination angle orbit planes can cover the pointing angles required to track the spacecraft during its whole mission. Notice that the apparent sparsity of calibration points at high elevation angles in Figure 6.6 is partially an artifact of displaying the LEO locations every 60 seconds. If we can reduce the unit time required for array calibration at each pointing angle, then more calibration points can be obtained.

So far we have not considered the timing sequence of the calibration targets. One problem that can occur is that two or more LEOs may appear over the desired spacecraft tracking zone simultaneously and the array can be pointed at only one of them. This is especially true when all the LEOs are put in the same orbit plane, as in the above simulations. To rectify this problem the number of orbiting planes can be increased while reducing the number of LEOs in each plane accordingly. Figure 6.7(a) shows the array observation angles in a one-day period by tracking 24 LEOs in 24 different orbital planes with equally spaced RAAN and 30.6° inclination angle (one LEO per each plane). Although in this scenario LEOs' appearances are spread over time, Figure 6.7(a) clearly shows that a full coverage of desired angle area cannot be accomplished in a single day calibration. Figure 6.7(b) shows the tracking angles for three consecutive days. Except low elevation angles, excellent coverage of the spacecraft-tracking zone is clearly observed over a three-day period. Notice that in Figure 7.5 the calibration points are connected sequentially to show better coverage of the tracking zone.

6.4 Phase Calibration Error and Array Gain Performance Analysis

In this section, the performance of the proposed calibration technique is evaluated in terms of the phase calibration residual errors and the array gain degradation caused

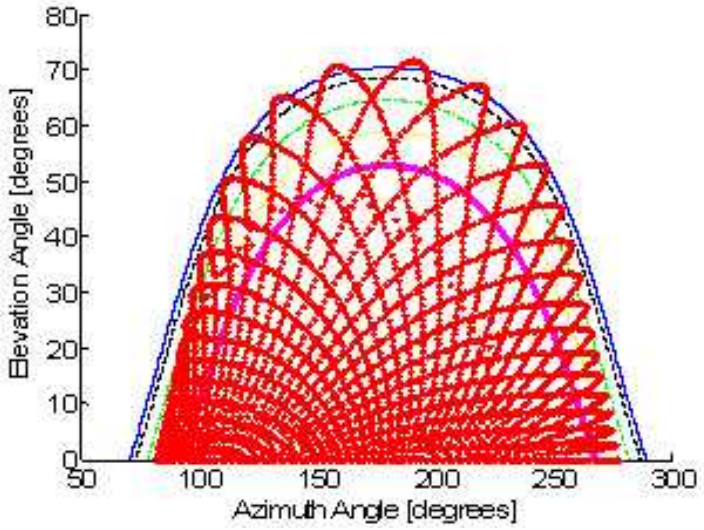

(a)

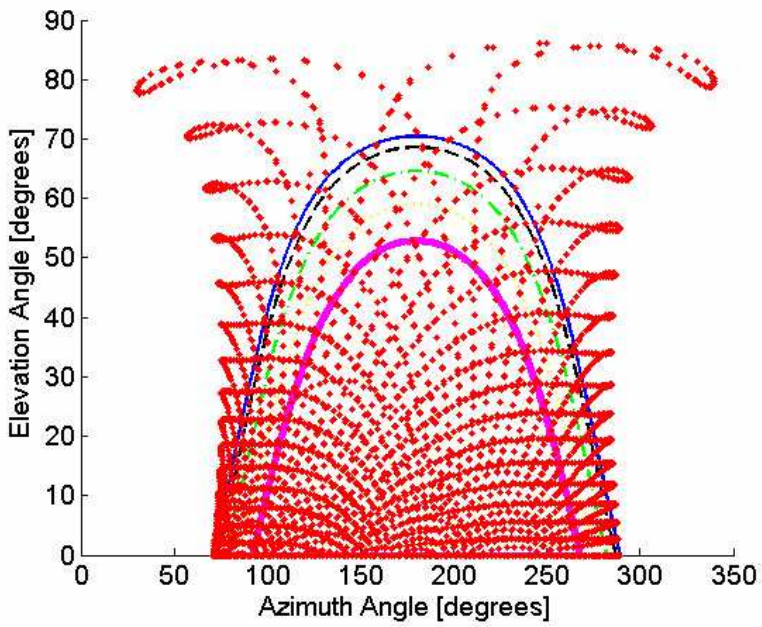

(b)

Figure 6.6: Pointing angle map for the spacecraft (whole mission, indicated by lines) and the calibration targets (one day, indicated by * markers): (a) LEO satellites in a 30.6° inclination plane; (b) LEO satellites in a 37.5° inclination plane.

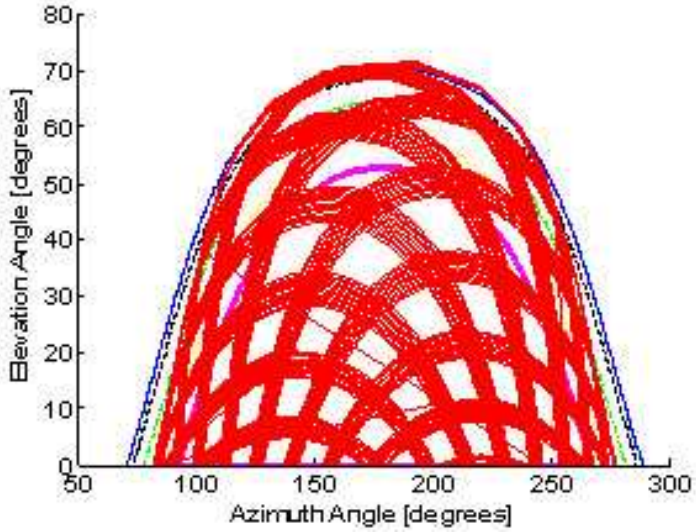

(a)

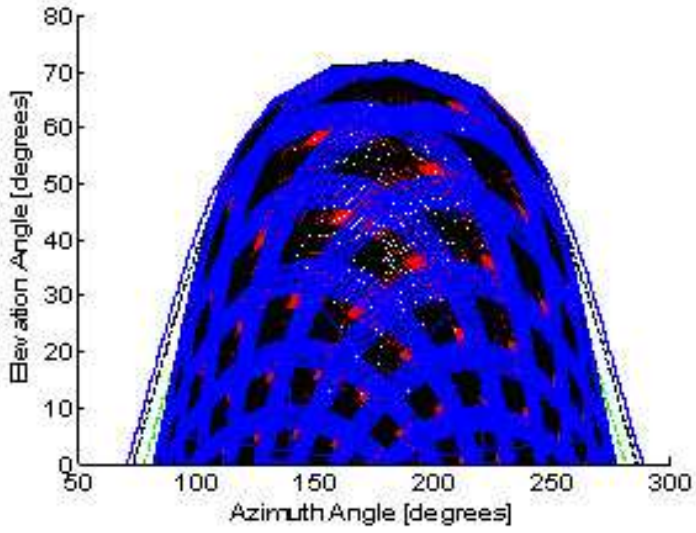

(b)

Figure 6.7: View angles of calibration points for 24 LEOs in 24 different orbital planes with equally spaced RAAN and 30.6° inclination: (a) in one-day period; (b) in three consecutive days.

by such errors. Basically there are two categories of phase calibration errors, namely the positioning errors and the signal phase errors. Positioning errors refers to the uncertainties of the location of calibration targets, array elements, and the spacecraft. Signal phase errors include the phase errors associated with the signals at each array element due to insufficient SNR, mechanical motion, and unstable phase reference distribution, etc. Since close-form solutions expressing these errors cannot be found, thus their effects on the calibration performance are studied through a Monte-Carlo simulation method.

6.4.1 Positioning Errors

As mentioned previously, the LEO calibration targets generally fall within the near-field of the array due to the very large physical extent of the array compared to wavelength. Therefore focusing on such targets does not produce the maximum array gain in the far-field where the deep space spacecraft is going to be. However it may be possible to compensate for the differences in signal paths, as shown in Figure 6.8. For simplicity, only two of the array elements are presented. Points **A** and **B** are the phase centers of the two elements. Assuming that the coordinates of **A** and **B**, and those of the calibration target (**C**) and the spacecraft (**D**) are known, the path difference between **AC** and **AD**, and that between **BC** and **BD** can be calculated and used for phase compensation. In practice, the exact locations are not available. The dash-dot circles in Figure 6.8 indicate the range of position uncertainty of the antenna, the target, and the spacecraft from their nominal locations. In fact, the positioning uncertainty of the spacecraft has a negligible effect, since the navigation tracking accuracy of the spacecraft is sufficiently high, e.g. within 10 nano-radians [61]. On the other hand, the calibration target, such as a LEO satellite, may not have a space navigation instrument, and therefore its position may not be known with the required accuracy. The physical positions of the antenna array elements

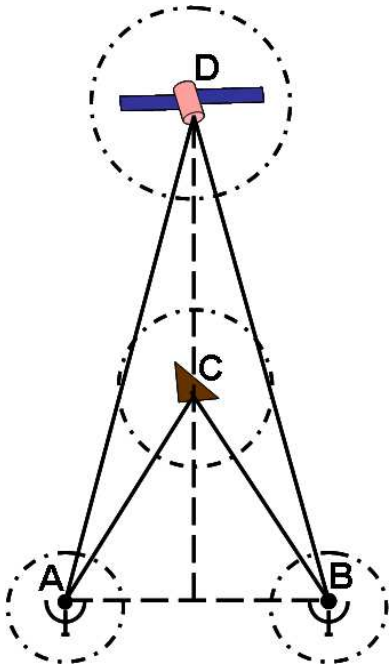

Figure 6.8: Phase compensation needed to correct for path length differences between the array elements to spacecraft and to the calibration target. The figure also shows the position uncertainties of the array elements, the calibration target, and the spacecraft.

can be determined to meter level accuracy, using the differential GPS technique [59]. However, the phase center of each antenna with large dimensions cannot be easily determined, especially at high frequency (X- or K- band). Nevertheless, the deviation of the phase center location from its nominal position is estimated to be less than several meters.

To investigate the effects of position uncertainties, a Monte-Carlo simulation is conducted for an 8×8 array at X-band (7.2 GHz). Each array element is chosen to be a 12m-diameter dish antenna and element spacing is assumed to be 72m. The array elements are placed on flat surface and the in-orbit target and the spacecraft are placed along the antenna boresight at 500 km and the 100,000 km respectively. First, the calibration target and the spacecraft are fixed at their nominal positions, and the position of each array element varies randomly according to a uniform distribution within a sphere centered at the nominal position of that element. The radius of the

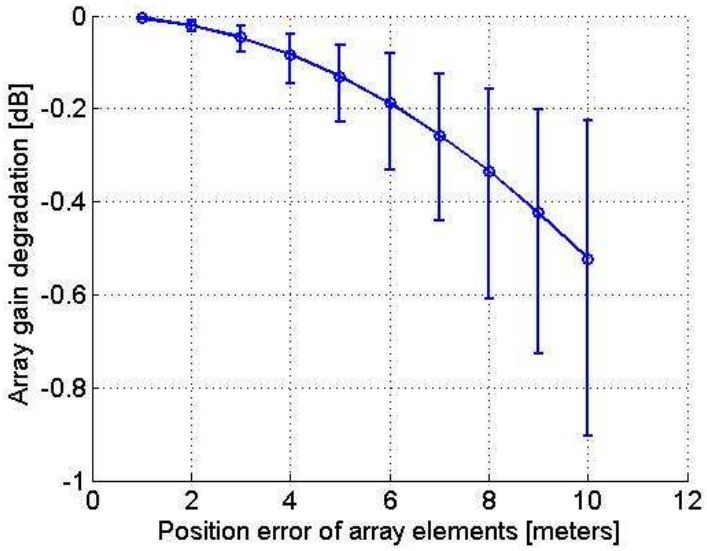

Figure 6.9: Array gain degradation versus the position error of array elements.

sphere is specified as the position deviation in meters. For each specific position deviation values, a Monte-Carlo simulation with 10000 realizations is carried out. For each realization, a random location is selected for antenna elements. After going through the proposed calibration procedure, the power received at the spacecraft is calculated and compared to its ideal value corresponding to a situation where all array elements are at their nominal positions. Figure 6.9 shows the degradation of the array gain versus the position deviation values of the array elements. The circle in Figure 6.9 indicates the mean degradation and the error bar specifies the range of the degradation. Gain degradation is observed to be very small in this case.

Next, the positions of the array elements and the spacecraft are fixed and the position of calibration target is varied within a sphere with a specified radius. Similar Monte-Carlo simulations are carried out. Figure 6.10 shows the array gain degradation as a function of calibration target position uncertainty radius. As the position error of the calibration target becomes larger, the array gain further deteriorates. For instance, for a 30m position uncertainty radius, which corresponds to a maximum

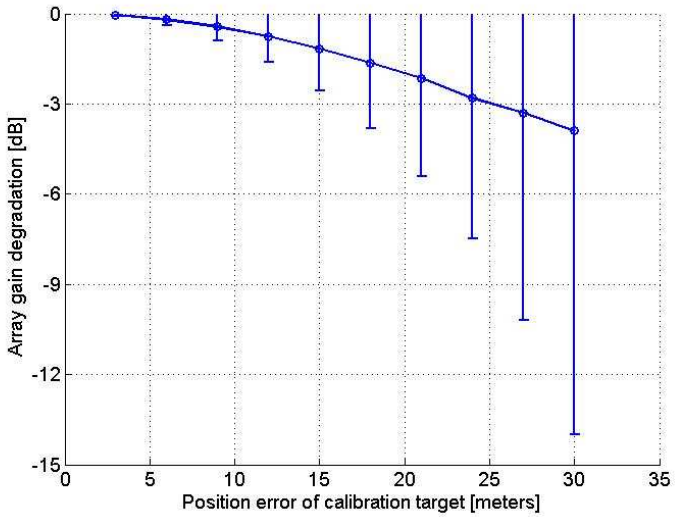

Figure 6.10: Array gain degradation versus the position error of calibration target.

angular deviation of 60 micro-radians, the array gain can suffer a maximum of 14 dB loss. Some angular measurement techniques, such as VLBI and differenced Doppler [61], is necessary to confine the positioning error of the calibration target within 15m (or 30 micro-radians) in order to limit the array gain degradation to less then a maximum of 3 dB. Another solution is to load a GPS receiver on board of the in-orbit satellite which carries the calibration target. This way, the target position can be measured to several meters accuracy. It is also worth mentioning that although the range of the gain degradation is relatively large, the mean degradation seems tolerable. Therefore some sort of statistical averaging will be helpful to improve the calibration performance. Of course this requires more calibration opportunities. From the above simulations, it is obvious that the positioning error of LEO calibration targets is the dominant factor in the calibration accuracy.

6.4.2 Signal Phase Errors

During the calibration process, besides the positioning errors, there are uncertainties associated with the phase of signals at each array elements. These errors

basically come from three sources: 1) phase measurement; 2) mechanical motions and thermal fluctuation; 3) signal propagation. Phase measurement error is directly related to the SNR, i.e. P_r/P_n. Here P_r, P_n are the signal and noise powers at the receiver respectively. Assuming a zero mean Gaussian noise, the knowledge of SNR is sufficient for determining the measured phase standard deviation which, in degrees, can be calculated from [63]

$$\sigma_\phi \approx \frac{57.3}{\sqrt{SNR}}. \tag{6.1}$$

The overall system SNR depends on the array system parameters and the target attributes. The starting point of calculating SNR is the radar equation given by

$$P_r = \frac{P_t A_{eff}^2 \sigma}{4\pi R^4 \lambda^2}. \tag{6.2}$$

where P_t is the transmit power, R is the target range to the radar, A_{eff} is the effective aperture of the antenna, σ is the target radar cross section (RCS), and λ is the wavelength. With P_t, A_{eff}, and λ fixed according to system standard, the only parameters to increase P_r, hence SNR, are R and σ. Smaller R renders larger P_r, however the integration time which affects SNR (as will be mentioned later) also becomes shorter. Therefore an optimal R value can be found. Meanwhile, the availability of the calibration targets at such range has to be considered. To improve the target RCS, retro-reflective structures such as corner reflectors, Luneburg lens, and Van Atta arrays may be employed [48]. Unlike a metallic sphere, the RCS of these structures is a function of incident angle, that is, only for a limited range of incident angles the RCS remains unchanged. This again could affect the integration time.

Noise power can also be easily computed from

$$P_n = KT_{sys}B_{eff} \tag{6.3}$$

where $K = 1.38 \times 10^{-23}$ is the Boltzmann's constant, $T_{sys} = T_{ant} + T_{rec}$ is overall system noise temperature including the antenna and receiver noise temperatures, and B_{eff} is the effective system bandwidth. The effective system bandwidth is defined as the smaller of the physical system bandwidth and the reciprocal of the coherent analog or digital integration time τ. In situations where SNR is poor (small target, long range, low transmit power, etc.) target response over many transmit pluses are averaged coherently to reduce the effect of noise. Equivalently this can be done by transmitting long pulses provided that the pulse duration does not exceed twice the travel time to the target ($\tau \leq 2R/c$). In practice, however, there is an upper bound for the integration time that is a function of system quality and measurement scenario. For a stationary scenario where both radar and target are fixed the upper limit for the integration time is determined by the radar system transmitter and local oscillator frequency stability. Over time periods of a few seconds or shorter the frequency drift of most stable sources can be approximated by a linear function of time, and may be represented

$$f_{drift} = \alpha t \tag{6.4}$$

where α is some constant specifying the rate of frequency drift. In this case the phase of the received signal is quadratic with time and therefore the upper bound for the integration time takes the following form

$$\tau \leq \frac{1}{\sqrt{2\alpha}}. \tag{6.5}$$

The integration time can be severely limited in two ways when the radar, target, or both are moving with respect to each other. First, the relative motion produces a Doppler shift, which if not account for, limits the integration time to $\tau \leq 1/(2f_d)$. Here $f_d = 2v/\lambda$ denotes the Doppler shift for a target having a radial velocity v with respect to the radar. In situation where the relative radial velocity of the target as

a function of time is known to within $\pm\delta v$, the integration time must be limited to $\tau \leq \lambda/(4\ \delta v)$. For example for an integration time of one second the radial velocity of the target must be known with an accuracy of 10^{-2} m/s at 7.2 GHz. In practice both Doppler shift and frequency drift exist and hence the combine effect must be considered, i.e. the upper bound for the integration time is given by

$$\tau \leq \frac{\sqrt{f_d^2 + 2\alpha} - f_d}{2\alpha}. \tag{6.6}$$

If the Doppler shift is known with an accuracy of $\pm\delta f_d$, the expression given by (6.6) can be used provided f_d is replaced with δf_d. Another limiting factor on the integration time for the non-stationary scenario is the temporal variation of the target backscatter. For physically large targets and at high frequencies the amplitude and phase of the target RCS varies very rapidly with the incidence angle that changes continuously as the target moves. For a target with a maximum dimension D_t a change in the aspect angle by an amount $\delta\theta = \lambda/(2D_t)$ can cause a significant change in the target RCS and as much as 180° phase shift in the backscatter field. This change of course depends significantly upon the shape and orientation of the target. For example the backscatter of a target with spherical symmetry (independent of its size) is insensitive to changes in the aspect angle. However most passive targets, such as space debris or in-orbit satellites, have complex geometries and sharp varying RCS patterns. Limiting the integration time to the first null of the RCS pattern, for a target at a distance R traveling with a tangential velocity u the integration time can be calculated from

$$\tau \leq \frac{R\lambda}{2D_t u}. \tag{6.7}$$

As an example, for $D_t = 5$m, $u = 555$ m/s, and $R = 500$ km, the maximum integration time is limited to $\tau = 2.7$s. An additional motion factor is wobbling of the target. In space most in-orbit objects have some undesirable wobbling motion, which can limit

the integration time by

$$\tau \leq \frac{\lambda}{2D_t f_w \theta_{max}} \tag{6.8}$$

where θ_{max} and f_w are, respectively, the maximum angular variation (with respect to radar look angle) and frequency of wobbling.

Once the effective system bandwidth is determined,the SNR at the output of each receiver can be determined. Figure 6.11 shows the received power normalized to noise power for a unit bandwidth for a monostatic radar system having a 12-m diameter reflector antenna with an aperture efficiency of 60% which transmits 3.6 kW power towards a calibration target with a nominal radar cross section 1 m^2 as a function of range. This figure provides P_r/KT at two operating frequencies at X-band (7.2 GHz) and Ka-band (35 GHz). In this simulation the overall receiver noise temperature of the receiver is assumed to be 60 Kelvin. As shown in Figure 6.11, for an in-orbit target at the altitude of 20,000 km (such as GPS satellite), the calculated P_r/KT is about 10.5 dB and 21.3 dB at X-band and Ka-band respectively. For an integration time of 1 ms, the SNR at X- and Ka-band are -19.5 dB and -8.7 dB respectively. According to (6.1), 1° phase measurement accuracy requires about 32 dB of SNR and -10 dB SNR can cause an exorbitant phase standard deviation (STD) of 180°. Here it should be pointed out that equation (6.1) for the phase standard deviation is only valid for relatively high SNR as it does not account for the fact that phase is measured modulus 2π. The most random case for phase probability distribution is a uniform distribution, which has a STD of about 104°. Therefore, unless the target range is reduced to within 3,000 km or the integration time is increased to at least 3 seconds, the phase measurement error would be greater than 10° for X-band operation.

Except for the phase measurement error, mechanical motion, thermal fluctuation, and signal propagation also introduce phase errors. As mentioned before, the uplink array operation relies on the application of the pre-stored phase calibration information obtained from in-orbit targets. Due to the time elapse between the calibration

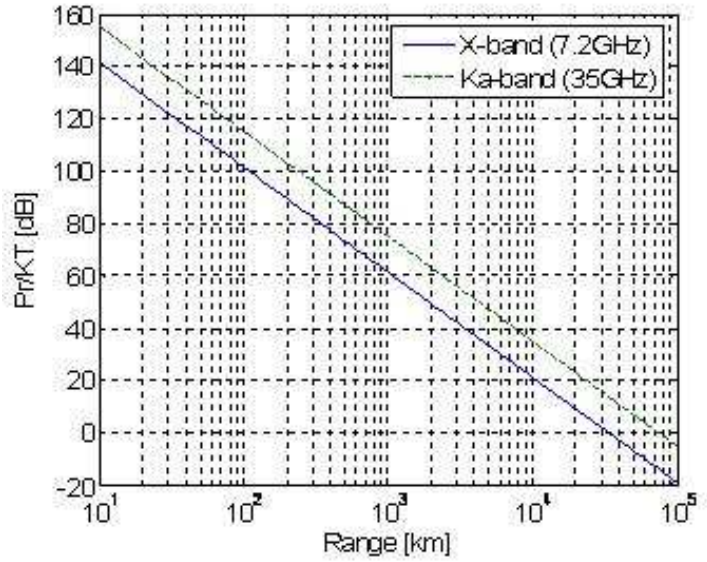

Figure 6.11: Received power over per unit bandwidth noise power versus range for a reflector antenna calibrating a target.

procedure and uplink communication, a number of environmental and systematic factors as well as residual calibration errors cause array phase uncertainties. For instance, the mechanical motion of the antenna structure, the wind and gravity effects may all change the phase center slightly, causing a certain amount of phase error. Similarly the dimensions and shape of the antennas may change with ambient temperature which could be different between the calibration and uplink operations. These changes may move the location of the array elements phase centers as well. In addition, the phase reference distribution could be unstable and fluctuates as a function of time. The devices along the signal path, such as mixers, filters, and amplifiers, etc., may have temporal variations. These changes can be easily corrected for by monitoring the phase of an injected tone slightly out of band. Also, the atmosphere, especially the troposphere, affects the signal phase distribution if the humidity and turbulence conditions vary across the array area. An estimation of such signal phase errors is given in [64, 65], and the typical values are listed in Table 7.1.

To quantify the effect of array phase distribution uncertainties, a Monte-Carlo

Table 6.1: Signal phase error budget table.

Signal Phase Error	**Typical Value**
1) Phase Measurement (at SNR = 32dB)	1°
2) Mechanical Motion & Thermal Fluctuation	
a) Feed Horn & BWG	2°
b) Mirror	3°
c) Reflector-Subreflector Structure	5°
3) Signal Propagation	
a) Phase Reference Distribution & BWG	2°
b) Mixers, Filters, Amplifier, etc.	7°
c) Troposphere & Ionosphere	7°

simulation is carried out for the same 8×8 array at X-band by giving the phase of each array element a random distribution and calculating the mean and standard deviation of the array gain degradation. Figure 6.12 shows the degradation of the array gain versus the standard deviation of a random phase error introduced to the phase of each array element. The phase error probability distribution is assumed to be a zero mean Gaussian random variable. In this simulation effects of positioning errors are ignored and 10000 Monte-Carlo realizations are conducted. As shown in Figure 6.12 the average array gain degradation is less than 3 dB for random phase errors with less than 40° standard deviation.

6.5 Conclusions

Array of large reflectors is studied for next generation deep space communication to enhance the radio link between ground stations and deep space spacecraft. Radar calibration technique using a number of LEO in-orbit calibration targets is proposed for determination of the array uplink phase distribution. The advantage of this technique lies in the fact that the calibration targets are in the far-field region of array elements and relatively a small number of them can supply frequent calibration opportunities for different array attitudes globally. In addition, such radar approach based

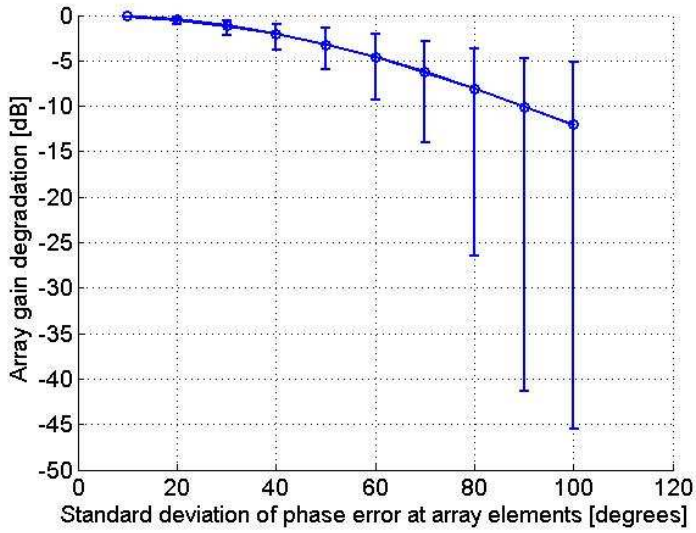

Figure 6.12: Degradation of array gain versus standard deviation of random phase errors introduced to each array element of an 8×8 array at X-band.

on the concept of phase conjugation makes the array operation easy and flexible. An overall system design and tracking scenarios are studied using STK software package to identify optimal calibration opportunities. A Monte-Carlo analysis on the array gain degradation due to random positioning of the array elements and the calibration target is conducted. This study indicates that array elements positioning errors have minimal effect on the array gain, while the calibration target positioning error can cause significant degradation. Similar study on the array gain degradation due to random signal phase errors is performed as well. This analysis shows that for phase errors within less than 40° gain degradation is not significant. The sources of signal phase errors are also clarified.

In order to avoid the calibration target positioning error, it is desired to use calibration targets in the far-field region of the whole array. Moon and the celestial radio emitter Quasar are two potential candidates. In the next two chapters, techniques based on using Moon and Quasar as array calibration targets will be introduced respectively. Notice that the signal phase error still exists. As a matter of fact, due to

the large distance of these far-field targets from the array, SNR is much reduced and may cause large phase measurement errors. Corresponding methods to overcome such a challenge will be presented. Other signal phase errors are independent of calibration schemes, therefore will not be repeated in the next two chapters.

CHAPTER 7

UPLINK CALIBRATION OF LARGE-REFLECTOR ARRAY USING LUNAR INSAR IMAGERY

7.1 Introduction

In the previous chapter, a radar calibration method, based on the concept of phase conjugation, is developed to obtain the proper phase distribution for array coherence. In this method LEO (low earth orbit) orbiters are selected as calibration targets due to their abundance in space and close range to the ground array. Through orbiting activity they are able to provide calibration opportunities for various array orientations. One issue about this method comes from the fact that both transmitter and receiver working at the same frequency band are required at each array element. The cost of building an array containing a large number of elements calls for an all-transmitter array, that is, each array element has only a transmitter and no receiver. Accordingly, the array calibration has to be conducted in an uplink mode.

Another issue lies in that LEO calibration targets fall within the array near-field. This necessitates a path-length difference correction to ensure the array focusing on the far-field instead of the near-field target. However, target positioning error can degrade the calibration performance, as shown in the previous chapter. The orbits of LEO targets tend to be unstable since they are often affected by local gravity field

variations and atmospheric drag effects. Existing tracking accuracy on these targets by NORAD (North American Aerospace Defense Command) is about 5 km [66], far beyond the threshold which can be tolerated. Installing GPS receivers on some new LEO targets would supply the required positioning accuracy, but launching these targets could be cost prohibitive. Equipping high-accuracy tracking facilities, such as a gigantic phased array radar, at the ground array site is another option, provided that the expense could be afforded. Alternatively, calibration targets in the array far-field can be used in which case it is not necessary to perform the path-length correction. However, the low SNR (signal-to-noise ratio) may become the major challenge for the calibration. For a 1 km $\times$ 1 km array operating at X-band (7.2 GHz) the far-field zone is at 48,000 km away. Compared to the LEO targets which are locate $\sim$1,000 km away, there is an extra free space path-loss of about 70 dB.

In this chapter, a new radar calibration method is proposed for the all-transmitter array where all array elements transmit simultaneously in the sense that the transmitted signals encounter the calibration target at the same time. Signals from different elements are modulated by different orthogonal PN (pseudo-noise) codes. Then the mixture of backscatter signals is received at a common receiver where matched filtering and phase detection are performed to provide the desired array phase calibration values. A natural celestial body, the Moon, is selected as a calibration target for its appearance in the array far-field. In addition, the large dimensions of Moon can cover the main beams of array elements and hence provide large backscatter signals to increase the signal-to-noise ratio (SNR). However, this cannot be easily achieved by treating the Moon as a point target like those LEO orbiters. Instead the footprint of a real-aperture ground antenna on the lunar surface is so large (hundreds of kilometers) that it is indeed a distributed target with unknown scattering phase center. In order to discover suitable "point targets" on the lunar surface for calibration, the planetary SAR (Synthetic Aperture Radar) imaging technique [68] can be

employed. For each array element, the relative motion between the Earth and Moon is able to form a very large synthetic antenna aperture that focuses at a set of small pixels on the lunar surface. Every pixel can be treated as a "point target". Each array element forms an image of these pixels based on their backscatter signals. The phase difference between images (backscatter signals) of the same pixel at different array elements is called an "interferogram". The system measuring and utilizing such interferograms is known as an interferometric SAR (InSAR) system. For the interest of this chapter, the interferogram is used to calibrate the phase distributions of the array. The number of pixels contributes as the number of independent calibration samples.

In what follows, section 7.2 explains how orthogonal PN-codes work for the all-transmitter array calibration. Then the details of the proposed calibration method via interferometric SAR (InSAR) imaging of Moon are described in section 7.3. Section 7.4 presents the phase difference (or interferogram) statistics between two array elements of an InSAR system analytically. In section 7.5, a 3D lunar random rough surface backscattering model is developed to simulate the interferogram statistics numerically under different scenarios. A practical example of calibration system parameters design is provided in section 7.6, and the effects of pixel SNR, undulation, and misregistration on the variance of interferogram are investigated. Section 7.7 draws the conclusions.

7.2 All-Transmitter Array Calibration

Figure 7.1 shows the simplified system block diagram of radar calibration for an all-transmitter array. A base-band radar pulse signal

$$A(t) = \begin{cases} 1 & 0 < t < \tau \\ 0 & otherwise \end{cases} \tag{7.1}$$

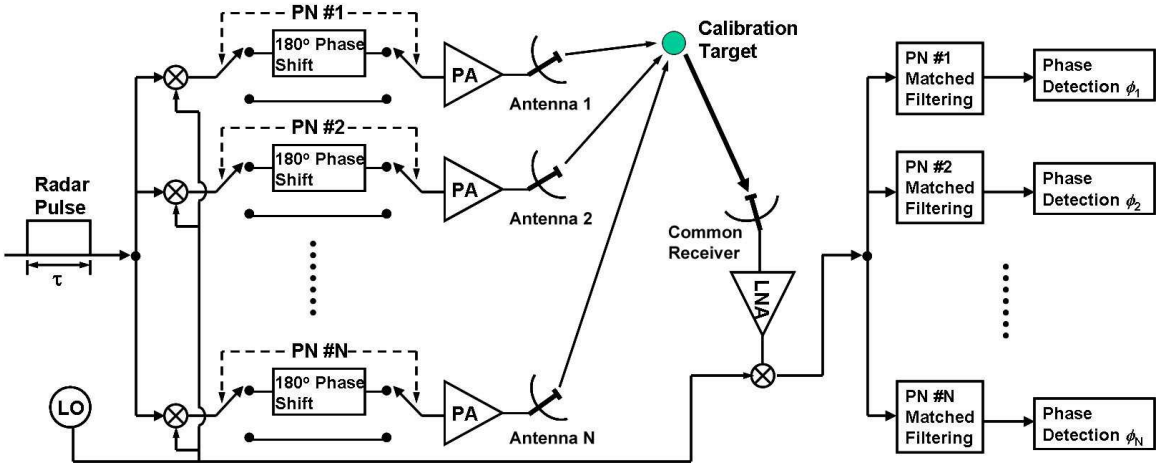

Figure 7.1: Simplified system block diagram of the all-transmitter array calibration.

(τ is the pulse duration) is up-converted to radio frequency (RF) at array element j (j = 1, 2, ..., N and N is the number of elements), by a carrier $\cos(\omega_c t)$ supplied from a common local oscillator (LO). The RF signal is then modulated by one of the N orthogonal PN-codes, $PN_j(m)$, using BPSK (binary phase shift keying), where m = 1, 2, ..., M. M is the chip length of the PN-codes, i.e. each PN-code contains a random sequence of M mixed +1's or −1's (chips). The modulated RF signal is then given by $p_j(t) \cdot \cos(\omega_c t)$, where

$$p_j(t) = \begin{cases} PN_j([t/\delta\tau] + 1) & 0 < t < \tau \\ 0 & otherwise \end{cases} \tag{7.2}$$

and $\delta\tau$ is the modulation duration for each chip. The operator [ ] takes the maximum integer less than the value inside. The signal is amplified and transmitted from the element antenna towards the calibration target which scatters the signal back to a common receiver. Considering the close spacing between array elements relative to the long range from the array to the calibration target, the aspect angles of incidence for all elements are almost the same, therefore a constant amplitude of backscatter from the calibration target, s, is assumed. The total received signal at the common

receiver is then given by

$$r(t) = \sum_{j=1}^{N} s \cdot p_j(t - t_j) \cdot \cos[\omega_c(t - t_j) + \theta_j] \tag{7.3}$$

where $t_j = d_j/c$ is the signal propagation time from the j^{th} element antenna to the calibration target and then to the common receiver, d_j is the corresponding path-length and c is speed of light. θ_j represents the phase shift due to instrument and atmosphere. In fact the phase value

$$\phi_j = \omega_c t_j - \theta_j \tag{7.4}$$

is exactly what is needed to calibrate the phase distribution of the array element. In order to detect ϕ_j , the received signal is first down-converted by the same carrier to

$$f(t) = \sum_{j=1}^{N} s \cdot p_j(t - t_j) \cdot \cos \phi_j \tag{7.5}$$

and then sent through a bank of matched filters $p_i^*(-t)$, $i = 1, 2, ..., N$. The matched filtering corresponds to a convolution operation in the time domain or a multiplication in the frequency domain. Therefore the Fourier transform of $u_i(t)$, the output signal of the i^{th} matched filter, is given by

$$U_i(\omega) = \sum_{j=1}^{N} s \cdot \cos \phi_j \cdot X_{ji}(\omega) \cdot e^{-j\omega t_j} \tag{7.6}$$

where

$$X_{ji}(\omega) = P_j(\omega) \cdot P_i^*(\omega). \tag{7.7}$$

$P_j(\omega)$, $P_i^*(\omega)$ are Fourier transforms of $p_j(t)$ and $p_i^*(-t)$ respectively, and the inverse Fourier transform of $X_{ji}(\omega)$ is a correlation operation in the time domain, given by

$$x_{ji}(t) = F^{-1}[X_{ji}(\omega)] = p_j(t) \otimes p_i^*(t) \tag{7.8}$$

where $F^{-1}[\ ]$ is the inverse Fourier transform operator and $\otimes$ stands for a correlation operator. Now the output signal $u_i(t)$ can be written as

$$\begin{aligned} u_i(t) &= F^{-1}[U_i(\omega)] = \sum_{j=1}^{N} s \cdot \cos(\phi_j) \cdot x_{ji}(t - t_j) \\ &= s \cdot \cos(\phi_i) \cdot x_{ii}(t - t_i) + \sum_{j \neq i}^{N} s \cdot \cos(\phi_j) \cdot x_{ji}(t - t_j). \end{aligned} \tag{7.9}$$

The PN-code has such a property that its autocorrelation function $x_{ii}(t)$ is similar to a triangle function which has a large peak at origin and very small amplitude elsewhere. The PN-codes chosen for different elements are orthogonal in the sense that their cross-correlation amplitudes are negligibly small compared to their auto-correlation peak amplitudes. Therefore one can detect the phase ϕ_i from $u_i(t_i)$ by setting $t = t_i$ in equation (7.9), where the autocorrelation $x_{ii}(0)$ term is the desired signal, cross-correlation $x_{ji}(t_i - t_j)$ terms contribute as noise, and the resulting SNR is approximately given by $g/(N-1)$. Here we introduce g as the "correlation gain" which is equal to the amplitude ratio of the autocorrelation peak of one PN-code to the average cross-correlation level between this PN-code and another PN-code. The larger the g is, the higher the SNR, and hence the more accurate phase detection.

The technique described so far assumes a stationary calibration target. For a moving in-orbit target, the transmitted signals from the various array elements need to impinge upon it at the same time to ensure a constant backscatter. This can be done through signal synchronization which adjusts the timing when radar pulses

are transmitted out of different array elements based on the path lengths from each element to the calibration target. Such synchronization is also necessary during uplink communication with deep-space targets. With the current NASA DSN timing standard [69], the accuracy of signal synchronization is at microsecond level, which is quite sufficient even for targets moving at a speed of thousands of kilometers per second.

One of the most commonly used PN-codes in communications is called the "maximal length sequence" (m-sequence) [67] whose chip length is $(2^k - 1)$ with k the number of shift registers for code generation. With a small number of shift registers, one can generate very long m-sequences. The peak-to-minimum ratio of the autocorrelation function is approximately equal to the chip length. The number of available m-sequences for a given k-stage shift registers is much less than $(2^k - 1)$ though. And the bound of the cross-correlation level of these m-sequences has no well-defined formula. Another type of PN-codes is the so-called "Gold" code [67]. It is obtained by combining a pair of m-sequences or their shifted versions. There are a total of $(2^k + 1)$ Gold codes available with k shift registers, and their cross-correlation level bound is well-defined as $(2^{k/2+1} + 1)$ for k even and $(2^{(k+1)/2} + 1)$ for k odd, with a little sacrifice on the autocorrelation performance. In the real implementation of the all-transmitter array calibration system, orthogonal PN-codes have to be carefully selected to ensure that both autocorrelation and cross-correlation meet the required criteria.

7.3 Lunar InSAR Imagery for Array Calibration

As mentioned earlier, the Moon is selected as the calibration target and the SAR imaging technique has to be employed to isolate the big antenna footprint on the lunar surface into many point-target-like small pixels. SAR is a coherent imaging system which makes use of the concept of synthetic aperture, that is, a large antenna

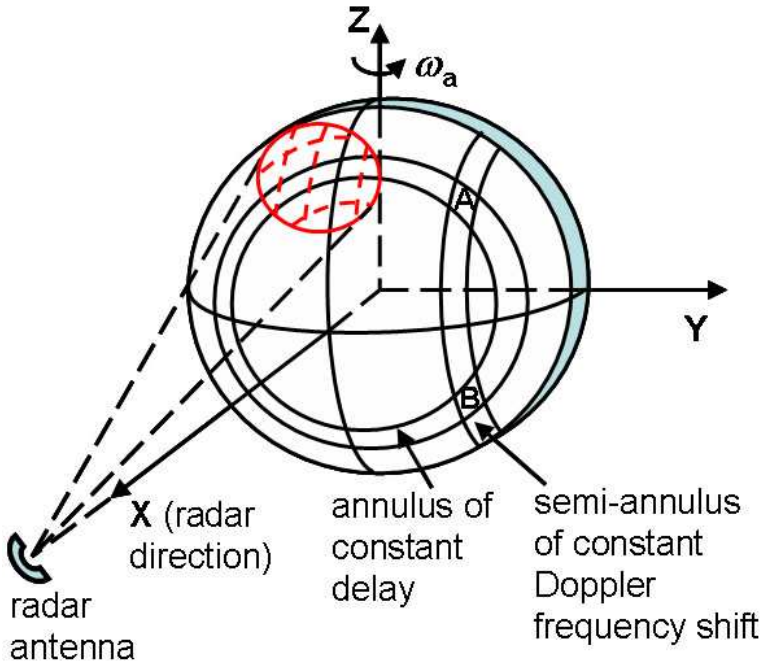

Figure 7.2: Earth-based SAR antenna taking images of lunar surface (adapted from [78]).

aperture is synthesized by recording the complex (both magnitude and phase) radar backscatter using a much smaller real antenna aperture at many spots along a path. An overview of SAR system characteristics and techniques can be found in many books [70, 71, 72, 73] and papers [74, 75, 76]. Utilizing the relative motion between the Earth and other celestial bodies to form the synthetic aperture, the planetary SAR imaging technique is also developed [77] using the delay-Doppler algorithm, similar to the range-Doppler algorithm in airborne SAR. Both Stacy [78] and Webb *et al.* [79] conducted radar imaging for the Moon and obtained high resolution lunar SAR images. Margot [80] took similar images at two NASA Goldstone DSN antennas to form an InSAR imaging system which provided lunar topography from the extracted interferograms. Next a brief review of the lunar SAR imaging technique is presented.

As shown in Figure 7.2, the x-axis is defined as the line of sight direction from Moon's center of mass (the origin) to the radar antenna on Earth. The z-axis is called the apparent rotation axis, which is a vector perpendicular to the x-axis and

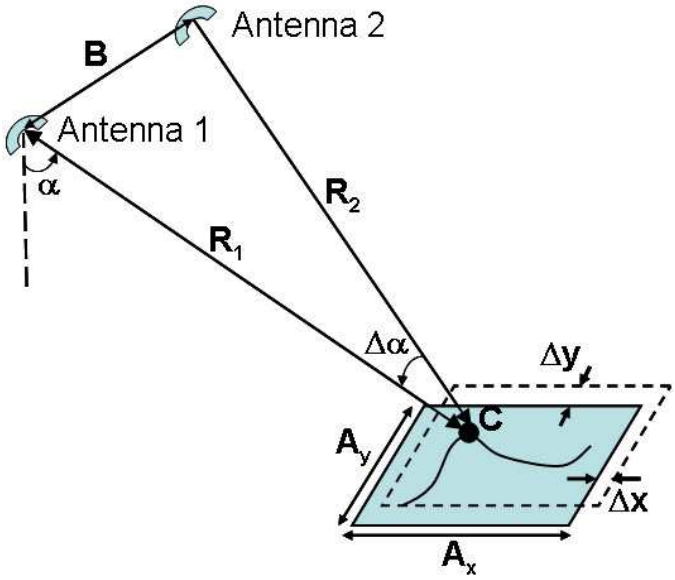

Figure 7.3: Interferometric SAR antennas taking images of a lunar surface pixel.

represents the direction of apparent angular velocity of the Moon, $\vec{\omega}_a$, as seen by the radar. The y-axis completes a right-handed coordinate system. Contours of equal range or constant delay form an annulus parallel to the y-z plane, while contours of equal Doppler shift form a semi-annulus parallel to the x-z plane. The latter is true because the line of sight velocity of any point on the lunar surface at a great distance from the radar on the Earth is given by

$$v_{los} \approx \vec{v} \cdot \hat{x} = (\vec{\omega}_a \times \vec{r}\,) \cdot \hat{x} = \vec{r} \cdot (\hat{x} \times \vec{\omega}_a) \propto r_y \tag{7.10}$$

where $\vec{r}$ is the vector from the origin to the surface point and r_y is its y-component. Therefore any surface points with the same r_y share the same Doppler shift. The two contours intersect and form two resolution pixels A and B which have the same delay and Doppler shift. Such north-south ambiguity can be avoided if the radar footprint on the lunar surface is confined to either the northern or the southern hemispheres, as shown in Figure 7.2.

By employing two array elements with SAR antennas on Earth to form an InSAR

imaging system, one can obtain two images (backscatter signals) for the same resolution pixel. As shown in Figure 7.3, the rectangle with solid sidelines represents a lunar surface pixel whose range and cross-range resolutions are A_x and A_y, respectively, and the equivalent scattering center is located at C. Both antenna 1 and 2 transmit and the mixed backscatter signals are received at antenna 1 (assuming element 1 is equipped with both transmitter and the common receiver). With orthogonal PN-codes used the two received signals can be extracted from their mixture. An interferometric operation on them results in a phase difference (interferogram). The two InSAR antennas have approximately same looking angle α to the pixel, due to the large slant ranges (R_1 and $R_2 \sim$ 300,000 km) and relatively small baseline (B $\sim$ 1 km). In other words, the angle between the line of sight directions from the two antennas to the pixel scattering center, $\Delta\alpha$, is very small. Therefore the backscatters of the pixel itself in response to incident waves from antenna 1 and 2 are almost the same, and their common phase can be canceled out through the interferometric operation. What is left in the interferogram is the phase difference term induced by path-length difference and instrument dissimilarity. This phase difference value is desired for phase calibrating the two elements, as mentioned before. Expressed mathematically, the two extracted received signals corresponding to elements 1 and 2 are given by

$$E_1 = P_1 + n_1 \tag{7.11}$$

and

$$E_2 = P_2 + n_2, \tag{7.12}$$

respectively, where P_1, P_2 are the echo signal from the imaged pixel given by

$$P_1 = K_1 \cdot \exp\left[j(\frac{2\pi R_1}{\lambda} + \theta_0)\right] \cdot S_1 \cdot \exp\left[j(\frac{2\pi R_1}{\lambda} + \theta_1)\right] \tag{7.13}$$

and

$$P_2 = K_2 \cdot \exp\left[j(\frac{2\pi R_1}{\lambda} + \theta_0)\right] \cdot S_2 \cdot \exp\left[j(\frac{2\pi R_2}{\lambda} + \theta_2)\right]. \tag{7.14}$$

K_1, K_2 are constants accounting for antenna gain, transmit power, and path-loss. θ_0, θ_1, and θ_2 are instrument phase shifts for element 1 receiving, transmitting, and element 2 transmitting, respectively. S_1, S_2 are complex scattering amplitudes of the pixel under the incidence from antenna 1 and antenna 2. n_1, n_2 are system noises inherent in the two received signals caused by both thermal and cross-correlation effects. λ is the wavelength at the operating frequency. Let us define the interferometric phase between the two received signals, i.e. the interferogram of the InSAR system, as

$$\phi = \arg\{E_1 \cdot E_2^*\}. \tag{7.15}$$

By multiplying (7.11) and conjugate of (7.12), one can obtain

$$E_1 \cdot E_2^* = P_1 \cdot P_2^* + P_1 \cdot n_2^* + n_1 \cdot P_2^* + n_1 \cdot n_2^* \tag{7.16}$$

where

$$P_1 \cdot P_2^* = K_1 K_2 \cdot |S_1 S_2| \cdot \exp(j\phi_0) \tag{7.17}$$

with the phase term

$$\phi_0 = \phi_{0c} + \arg\{S_1 S_2^*\} \tag{7.18}$$

and

$$\phi_{0c} = \frac{2\pi(R_1 - R_2)}{\lambda} + \theta_1 - \theta_2. \tag{7.19}$$

Phase coherence can be realized by compensating for ϕ_{0c} during uplink operation. Notice that the path-lengths R_1 and R_2 are based on the equivalent scattering center of the pixel, which may deviate from its geometric center. It has to be ensured that such deviation is insignificant.

In practice only the interferogram ϕ is measured. Assuming the system noises are small enough to be neglected in equation (7.16), ϕ is approximately equal to ϕ_0. Furthermore, since

$$S_1 \approx S_2, \tag{7.20}$$

then $\phi_0 \approx \phi_{0c}$ and hence $\phi \approx \phi_{0c}$. In other words, ϕ can be used as a substitute for ϕ_{0c} to phase calibrate the two elements. However, unlike ϕ_{0c} which is a deterministic value, ϕ is a random variable due to system noise and backscatter signal fading. The signal fading results from the random rough surface characteristics of the pixel. Therefore ϕ has a probability density function (PDF) centered at ϕ_{0c} with certain deviation. The narrower the deviation, the more accurately one can use a single measured ϕ value for calibration. In the next section, the PDF of ϕ is examined in detail and a number of factors affecting the variation of ϕ are discussed.

7.4 Interferometric Phase Statistics

The statistics of the phase difference between the backscatter signals of two SAR antennas (E_1 and E_2) from the same target has been analytically derived by many authors [81, 82, 83, 84], where the two signals under study are assumed to be zero-mean circular complex Gaussian random variables. This is a reasonable approximation according to [85], where the use of Rayleigh fading statistics is experimentally justified for many kinds of terrains. Let us define the complex correlation coefficient of E_1 and E_2 as

$$\gamma = \frac{\langle E_1 \cdot E_2^* \rangle}{\sqrt{\langle |E_1|^2 \rangle \cdot \langle |E_2|^2 \rangle}} \tag{7.21}$$

where the operator $\langle\ \rangle$ stands for expectation. Then the PDF of the interferogram is obtained by [83]

$$PDF(\phi) = \frac{1-|\gamma|^2}{2\pi}\frac{1}{1-\beta^2}\{1+\frac{\beta\cdot\cos^{-1}(-\beta)}{(1-\beta^2)^{1/2}}\}, \tag{7.22}$$

where

$$\beta = |\gamma|\cdot\cos(\phi-\bar{\phi}_0) \tag{7.23}$$

and

$$\bar{\phi}_0 = \arg\{\gamma\}. \tag{7.24}$$

$|\gamma|$, $\bar{\phi}_0$ are known as the degree of correlation and the coherent phase difference, respectively [83]. It is not difficult to prove that

$$\bar{\phi}_0 = \phi_{0c} + \arg\{\langle S_1\cdot S_2^*\rangle\}. \tag{7.25}$$

Under the assumption of equation (7.20), $\bar{\phi}_0 \approx \phi_{0c}$. Figure 7.4 plots the PDFs of ϕ with different values of $|\gamma|$, assuming $\bar{\phi}_0 = 0°$. $\bar{\phi}_0$ is the mode of the PDF, and ϕ concentrates around $\bar{\phi}_0$ with a certain deviation which decreases as $|\gamma|$ increases. Therefore, the accuracy of estimating $\bar{\phi}_0$ using a sample of ϕ can be improved by maximizing the degree of correlation.

Basically there are five types of decorrelation effects, namely thermal, baseline, misregistration, Doppler, and temporal decorrelations [81, 86, 87]. Thermal decorrelation results from system noise n_1, n_2. Even if P_1 and P_2 were perfectly correlated, E_1 and E_2 will still have a certain amount of decorrelation because n_1 and n_2 are uncorrelated. The other four decorrelations all refer to the decorrelation of P_1 and P_2, in that S_1 and S_2 are not exactly equal to each other. The slight difference of incidence angle, $\Delta\alpha$, will cause the so-called baseline decorrelation. In some cases, especially for repeat-pass InSAR, the pixels the two antennas focused on are not exactly the same

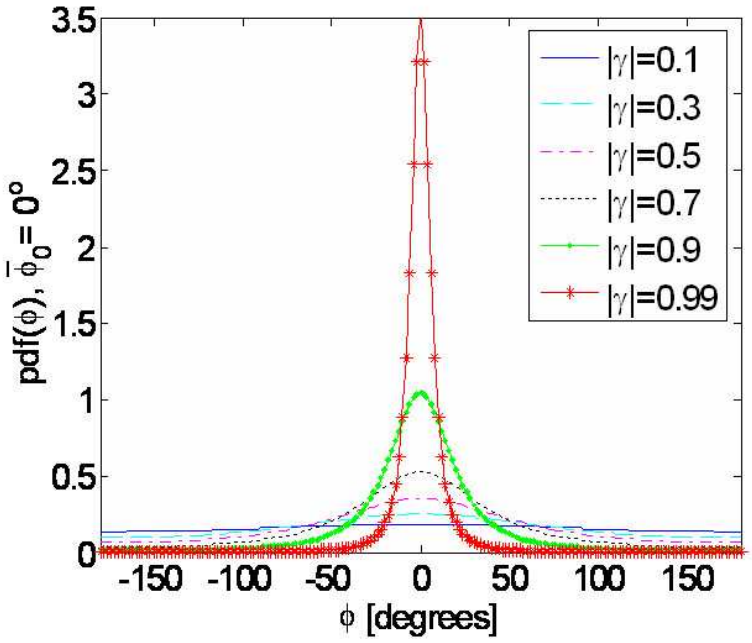

Figure 7.4: PDFs of an interferogram for fixed $\bar{\phi}_0 = 0°$ and different $|\gamma|$.

one, even after the image coregistration process [70]. As seen in Figure 7.3, the two pixels with solid-line and dash-line borders (pixel #1 and #2) have slight deviation Δx and Δy at the range and cross-range directions, respectively. In this case, the scattering amplitude of these two pixels, S_1 and S_2, are slightly different. This decorrelation between S_1 and S_2 results in so-called misregistration decorrelation. Doppler decorrelation happens due to the slightly different line of sight velocity, hence the Doppler frequency shift, as viewed by the two antennas. Usually this decorrelation effect can be avoided by compensating for the Doppler frequency shift difference using the available ephemeris information. The temporal decorrelation is only observed for repeat-pass InSAR, since the scatterers inside the same pixel may vary with time. An analytical expression for the relationships between the degree of correlation and the major three decorrelation effects, i.e. thermal, baseline, and misregistration, is developed in [86]. However, to relate these decorrelations with the variation of the interferogram ϕ around $\bar{\phi}_0$ requires a numerical simulation.

It is also worth mentioning that besides maximizing the degree of correlation, an alternative way of reducing the variance of the interferogram is to use multi-look (or multi-pixel) averaging. With N_s independent measurement samples of E_1 and E_2, the interferogram is given by a maximum likelihood estimator [70]

$$\hat{\phi} = \arg\left\{\sum_{i=1}^{N_s} E_{1i} \cdot E_{2i}^*\right\}. \tag{7.26}$$

Its PDF has been thoroughly studied in [82, 84], which still has a mode at $\bar{\phi}_0$ but with narrower deviation depending on both the degree of correlation and the number of independent looks.

7.5 3D Interferometric Scattering Model

The analytical analysis in [86] is based on some statistical assumptions such as the Rayleigh fading characteristics of the scattered signals and the white uniform scattering function. There is no specific scattering model involved. For InSAR imaging of the lunar surface, the fluctuation pattern of the terrain elevation, the dimensions of the imaged pixels, the realistic surface scattering mechanism, may all affect the above assumptions. What's more important, the analysis assumes locally constant terrain height over the whole pixel, and only results in a 2D scattering function. This assumption may also affect the phase computation of the received signals at radar antennas. Therefore a more realistic and accurate 3D terrain scattering model is necessary to evaluate the interferogram statistics and hence the array calibration performance. In this section such a model is developed.

7.5.1 Lunar Surface Properties

During the boom of lunar exploration in 1960s and 1970s, many lunar orbiter satellites were launched to study the lunar surface [88, 89, 90, 91, 92]. Meanwhile, Earth-based remote probing of the moon surface through infrared and microwave emission or radar techniques was also conducted [93]. From these studies, a great deal of the lunar surface properties, such as the lunar topography, surface roughness, the composition and dielectric constant of the lunar soil, were learned. The Moon surface is essentially a rocky sphere with a mean radius of $R_m \approx 1737.1$ km [96], but the dynamic range of the surface elevation can reach ± 8 km. It is covered by a gently rolling layer of powdery soil with scattered rocks, called the regolith. Studies on the regolith [90, 91, 94, 95] have found that it is an unconsolidated layer of several meters extent, with the effective dielectric constant ϵ_r around 2.5 to 3.0. As a natural terrain surface, the lunar surface obeys power-law spectra for its surface height correlation function [97], with an average rms slope of about several degrees. Such surfaces possess self-affine, or fractal, roughness properties, i.e. a roughness appearance independent of the scale of observation [35]. The Hurst exponent [98], H, controls the rms height and correlation length observed at a given scale L by

$$h_L = h_0 \cdot \left(\frac{L}{L_0} \right)^H \tag{7.27}$$

and

$$l_L = l_0 \cdot \frac{L}{L_0}, \tag{7.28}$$

where h_L, l_L and h_0, l_0 represent the rms height and correlation length observed at scale L and a reference scale L_0, respectively. Planetary surfaces generally have H ranging from 0.5 to 0.95 [35]. Smith *et al.* [99] applied the power-law spectrum function used by Goff and Jordan in their seafloor topography study [100] to characterize the lunar topography based on the Clementine altitude data [101], and achieved good

agreements. The 2D covariance function of the surface height is given by

$$c(\rho) = h^2 G_\nu(k_c\rho)/G_\nu(0) \tag{7.29}$$

where $G_\nu(x) = x^\nu K_\nu(x)$ and K_ν is the modified Bessel function of the second kind and order ν. h represents the rms height and k_c is some corner wave number determining the correlation length as $1/k_c$. The corresponding 2D power spectrum is then

$$P(k) = 4\pi\nu h^2 k_c^{-2} \left[\left(\frac{2\pi k}{k_c} \right)^2 + 1 \right]^{-(\nu+1)} \tag{7.30}$$

where k is the wave number in unit of m^{-1}. It is believed that there is a typo in the equation for $P(k)$ in [99]. In the case of $\nu = 0.5$, equations (7.29) and (7.30) reduce to those for an exponential surface with $c(\rho) \sim \exp(-k_c\rho)$. After processing the Clementine data, Smith *et al.* present the surface large-scale roughness (undulation) of the Moon in $30^\circ \times 25^\circ$ squares with stochastic parameters such as the rms height and correlation length. These parameters vary markedly over the lunar surface and are based on observation scales at about 10 to 100 km.

7.5.2 Generating a Lunar Surface Pixel

Based on the lunar surface properties described above, the elevation profile of a pixel on the Moon surface can be generated. Generally the InSAR imaging pixels have much smaller scales than the Clementine observation scales. In this case, equations (7.27) and (7.28) are used to adjust the rms height and correlation length according to the desired scale. Then equation (7.30) is adopted with some reasonable value of ν to generate the surface profile using the 2D spectral synthesis technique described by Saupe [102, 103]. As an example, let us consider a 640m $\times$ 640m pixel and divide it into a 64×64 grid, rendering a scale of $L = 10$ m. Assuming $L_0 = 10$ km, $h_0 = 1$ km,

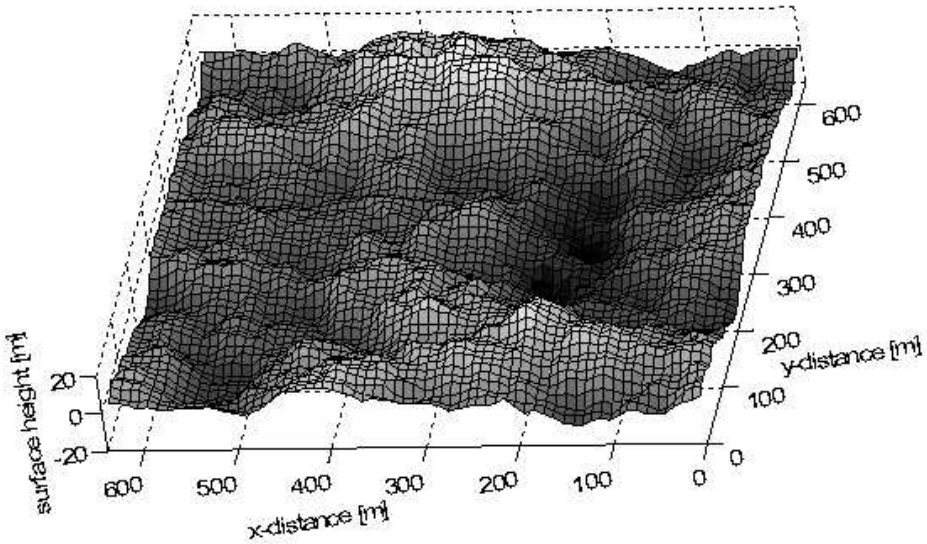

(a)

(b)

Figure 7.5: (a) surface elevation profile of a lunar pixel (640 × 640m) generated by the 3D random rough surface generator; (b) optical image of the lunar surface.

$H = 0.7$ and $l_0 = 100$ km, we get $h_L \approx 8$ m and $l_L = 100$ m (therefore $k_c = 0.01$ m^{-1} in (7.30)). According to [100], ν is just equal to the Hurst exponent H. A random sample of this surface profile is plotted in Figure 7.5(a). One can see its similarity with the optical image (shown in Figure 7.5(b)) taken by a lunar-orbiting satellite. The mosaics in Figure 7.5(a) making up the surface are formed by connecting the neighboring four surface height grids. Each mosaic actually contains two triangular sheets (sub-pixels), such as T_1 and T_2 shown in Figure 7.6, forming a rooftop-like geometry.

7.5.3 Scattering from a Lunar Surface Pixel

With the high-fidelity lunar surface pixel constructed, we are ready to set up a model to compute interferometric backscatter signals. As shown in Figure 7.6, the scattered fields from every single sub-pixel (triangular sheet) are coherently added at the receiver antenna. The path-lengths R_1 and R_2 are calculated from antenna 1 and 2 to the geometric center of each sub-pixel, and should take into account the elevations of the sub-pixels. T_x represents the dimensions of the sub-pixel. The backscatter function $s(x_i, y_i)$ of the i^{th} sub-pixel at (x_i, y_i) can be assumed the same for both antennas. In addition, $s(x_i, y_i)$ and $s(x_j, y_j)$ from two different sub-pixels (i^{th} and j^{th} sub-pixels) are assumed to be uncorrelated provided that the dimension of the sub-pixel contains several wavelengths. Values of misregistration errors Δx and Δy can be selected arbitrarily, but are generally around 0.05 $\times$ pixel dimension [86] based on the performance of the standard coregistration technique [104] in SAR image processing.

It is assumed that $s(x_i, y_i)$ is a complex Gaussian random variable with $\langle |s(x_i, y_i)|^2 \rangle = a_i \sigma_0$, where a_i is the area of the i^{th} sub-pixel. σ_0 is the average radar cross section per unit area for the sub-pixel and can be computed by standard rough surface scattering models, such as PO (Physical Optics) [105]. Basically, the sub-pixel is still a

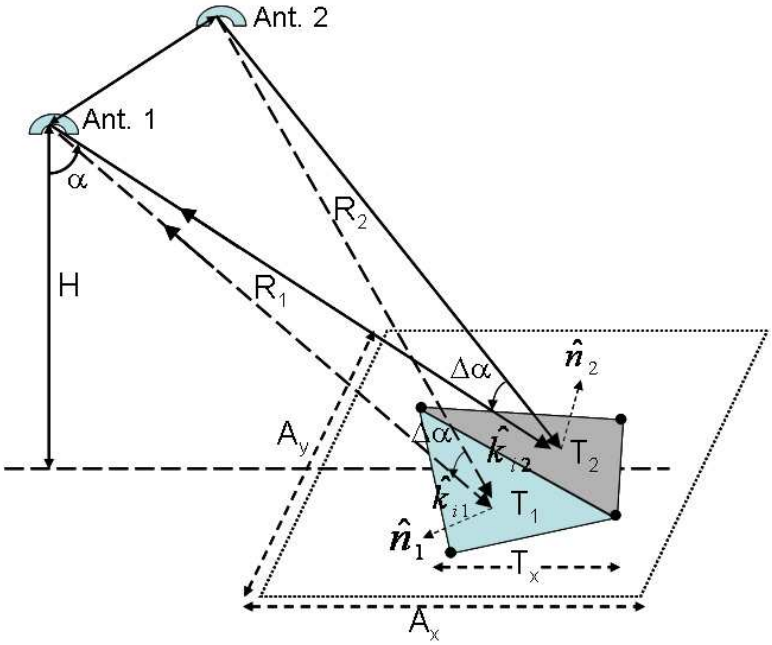

Figure 7.6: Backscatters of sub-pixels under the illumination of antenna 1 and 2, received at antenna 1.

rough surface, only with a much smaller scale of roughness. Power spectrum (7.30) is applicable, but an exponential surface correlation function is better in providing a closed-form expression. Figure 7.7 shows the σ_0 versus local incidence angle θ_i upon the sub-pixel. Both measurement data obtained by Hagfors [93] and computational results from a PO backscatter model with an exponential rough surface are presented. $\epsilon_r = 2.6$ is assumed, and the surface rms roughness and correlation length are selected to be 1 cm and 8 cm to achieve a good agreement. It has to be mentioned that the scattering models used here are based on a semi-infinite ground with a random rough surface. This approximation is reasonable although the lunar regolith is only several meters deep on average, because the frequency bands of interest are X-band and Ka-band whose wavelengths are centimeters or sub-centimeters. In addition, the scattering effects contributed by the individual rocks on top of or underneath the ground [93] are accounted for in our model through the surface roughness and the equivalent dielectric constant of the regolith.

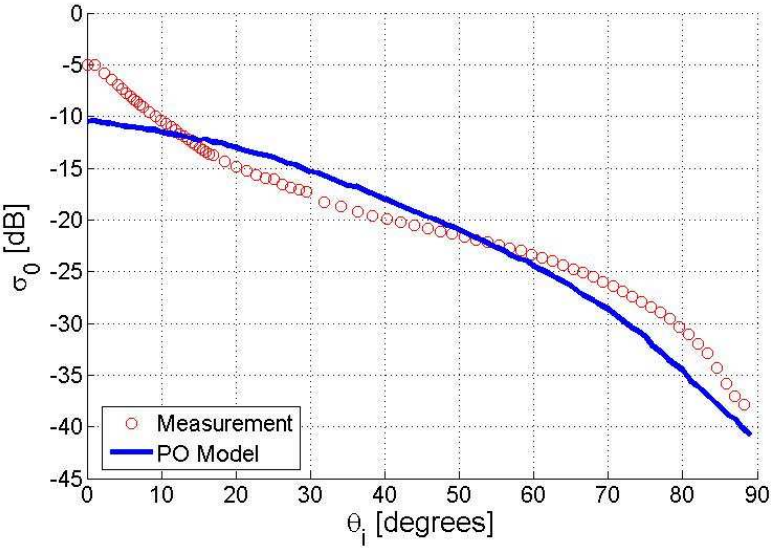

Figure 7.7: Comparison between measurement and model prediction for backscatter RCS of lunar surface.

In order to compute σ_0 of the i^{th} sub-pixel, the local incident angle must be determined. This is given by $\theta_i^L = \pi - \cos^{-1}(\hat{k}_i \cdot \hat{n})$, where the superscript "L" stands for local, $\hat{k}_i$ is the direction of the incident wave, and $\hat{n}$ is the outward vector normal to the sub-pixel. θ_i^L should be in the range of $[0,\ \pi/2]$ and if $\theta_i^L > \pi/2$, the backscattering contribution from that sub-pixel is neglected due to shadowing.

Once σ_0 is computed for the i^{th} sub-pixel, a random sample of $s(x_i, y_i)$ can be generated, where both its real and imaginary parts are random numbers drawn from a zero-mean Gaussian distribution with standard deviation $\sigma_0/\sqrt{2}$. After considering the antenna pattern and path-length, the backscatter signal at the receiver antenna contributed by the i^{th} sub-pixel can be calculated. Coherently summing up the contributions from all sub-pixels, the total scattered signals P_1 and P_2 are obtained. The system noises n_1 and n_2 are then generated randomly from zero-mean Gaussian distributions with their variances corresponding to the specified noise powers. By adding P's and n's, the received signals E_1 and E_2 can be computed. An independent sample of the interferogram can then be generated using equation (7.15). Repeating

the above process for a number of realizations, many samples of interferogram can be obtained and the histogram of the interferogram can be plotted to estimate the phase difference required for calibrating the two array elements, and to evaluate the accuracy of the estimation.

7.5.4 Monte-Carlo Simulation of Interferogram

An example of Monte-Carlo simulation computing the interferogram statistics based on the above algorithm is presented as follows. DSN X-band uplink frequency f = 7.2 GHz, and the lunar surface $\epsilon_r = 2.6$ are assumed. Let us first generate a similar pixel as in Figure 7.5(a), i.e. a 640m × 640m pixel with 64 × 128 sub-pixels (triangular sheets). The generated pixel is then imprinted on top of the underlying lunar sphere, with its center located at a spot of interest, e.g. 45° elevation (from the xy-plane) and 0° azimuth (from the +x-axis) angles based on the coordinates shown in Figure 7.2. Two Earth-based antennas are located on the +x-axis with 300m spacing. The distance from the Moon to the middle point between the two antennas is set to be 3.8×10^8 m. As to the receiver signal-to-noise ratio (SNR), let us use the same value as in [80] which is about 21.5 dB per unit surface area, since the backscatter power is directly proportional to the pixel area. The interferogram computation is carried out for 1000 realizations and the histogram is plotted in Figure 7.8. A bell-shape PDF similar to those in Figure 7.4 is observed. The MLE (maximum likelihood estimator) of the mode of this distribution, i.e. the estimated coherent phase difference $\hat{\bar{\phi}}_0$, is 13.34°. Since no instrument phase difference between the two antennas has been introduced in the simulation, $\hat{\bar{\phi}}_0$ accounts for path-length difference only. Using the geometric center point of the pixel to compute the path-length, the corresponding phase difference ϕ_{0c} is about 13.33°. This agrees very well with the simulation result, indicating that the equivalent scattering center of the pixel is very close to its geometric center. The standard deviation from the estimated mode $\hat{\bar{\phi}}_0$ is

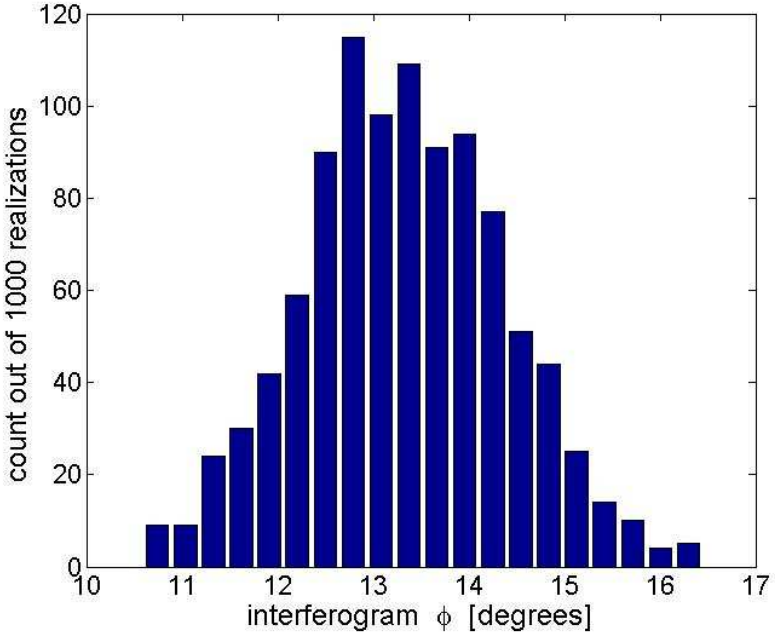

Figure 7.8: Histogram of interferogram based on 1000 realizations.

very small, about 1.05°, since the relatively short baseline and small pixel size result in negligible baseline decorrelation, pixel misregistration is neglected in the simulation, and the SNR is very high, about 34.6 dB. Recall that the phase measurement error due to thermal noise is related to SNR as [63]

$$\epsilon_\phi \simeq \frac{57.3^\circ}{\sqrt{SNR}}. \tag{7.31}$$

Therefore, under the conditions in this simulation, a very accurate estimate of the correct value for array phase calibration can be obtained by measuring a single sample of the interferogram.

7.6 InSAR Calibration System Parameters Design

7.6.1 Signal-to-Noise Ratio

The simulation result presented in the previous section is overly optimistic since an extremely high SNR is assumed by using the DSN 70-m reflector antenna as the transmitter with a peak transmit power of 350 kW and 34-m reflector antenna as receiver. It is not practically feasible to form a ground array of hundreds of such big reflectors. In fact the original proposal [33, 65] was to use 12-m reflectors with a peak transmit power of 3.6 kW. Obviously the SNR in the latter case is much lower for the same size pixel. The expression for SNR in the SAR imaging process is given by [80]

$$SNR = \frac{P_t G_t}{4\pi R^2} \sigma_0 A_{scatt} \frac{A_r}{4\pi R^2} \frac{1}{kTB} \frac{\tau_p}{\delta\tau} f_p t_{coh} \tag{7.32}$$

where

P_t peak transmitter power;

G_t transmitter antenna gain;

R distance to the Moon;

σ_0 average backscatter cross section per unit area of the lunar surface;

A_{scatt} area of the lunar surface imaged pixel;

A_r effective area of the receiver antenna;

k Boltzmann's constant ($= 1.38 \times 10^{-23}$);

T sum of the receiver system temperature and the noise temperature of the Moon;

B bandwidth of the receiving system;

τ_p uncompressed pulse width;

$\delta\tau$ compressed pulse width;

f_p pulse repetition frequency;

t_{coh} coherent processing interval.

The factor $\tau_p/\delta\tau$ results from the pulse compression technique [106] which is routinely employed in radar imaging. The uncompressed pulse is divided into many much narrower compressed pulses that are phase modulated according to a specific PN-sequence (similar to those described in section 7.2). The compressed pulse width corresponds to the range resolution

$$r_g = c \cdot \frac{\delta\tau}{2}. \tag{7.33}$$

The cross-range resolution is given by [80]

$$r_{az} = \frac{\lambda}{2\omega_a}\delta\nu = \frac{\lambda}{2\omega_a \cdot t_{coh}} \tag{7.34}$$

where ω_a is the apparent angular velocity of the Moon, $\delta\nu$ is the Doppler spectral resolution and equal to the inverse of the time interval over which radar returns are collected coherently. The pixel area is the product of range and cross-range resolutions, i.e.

$$A_{scatt} = r_g \cdot r_{az}. \tag{7.35}$$

Substituting (7.33-7.35) into (7.32), and taking into account the fact that for an optimal receiver $B \cdot \delta\tau \approx 1$, one obtains

$$SNR = \frac{P_t G_t A_r}{(4\pi R^2)^2}\sigma_0 f_p \tau_p \frac{c\lambda\delta\tau}{4\omega_a kT}. \tag{7.36}$$

A number of parameters in (7.36) are fixed such as R ($\approx 3.8\times10^8$ m), ω_a ($\approx 10^{-6}$ rad/s), and T ($= T_{sys} + T_{Moon} \approx 60 + 200 = 260$ K). $P_t = 3.6$ kW is available although 20 kW peak transmit power is more favorable. Using 12-m reflectors at 7.2 GHz with 64% efficiency, $G_t \approx 57$ dB. One existing 34-m reflector (assuming 64% efficiency as well) can serve as the common receiver giving effective $A_r \approx 580$ m^2. The average scattering cross section per unit area, σ_0, can be read from Figure 7.7

with the incidence angle computed as that between the direction from the transmit antenna to the pixel geometric center and local normal at the center of the pixel. It is obvious that areas under near normal incidence provide stronger backscatter, but the north-south ambiguity explained in section 7.3 prohibits the imaging of such areas. Nevertheless a value of 15 dB can be assumed for σ_0 by keeping the incidence angle around 30°. The radar duty cycle $f_p\tau_p$ has to be chosen, e.g. 10%, such that it allows interleaving of transmit and receive signals in order to avoid interference.

It seems from equation (7.36) that high SNR favors large $\delta\tau$ or r_g. This is actually an artifact resulting from the fact that cross-correlations between received signals from different array elements have not been considered yet. Assuming N elements use orthogonal PN-codes of length M chips ($M = 2^k - 1 = \tau_p/\delta\tau$), the SNR including cross-correlation is approximately given by

$$SNR \approx \frac{S}{kTB + S(N-1)/g} \tag{7.37}$$

where S stands for the desired signal from one element and according to (7.36)

$$S = \frac{P_t G_t A_r}{(4\pi R^2)^2}\sigma_0 f_p \tau_p \frac{c\lambda}{4\omega_a}. \tag{7.38}$$

kTB is the thermal noise, and $S(N-1)/g$ gives the cross-correlations from other elements as noises. g is the correlation gain mentioned in section II, and usually there is a positive correlation between g and M. For example, the bound of cross-correlations between Gold colds is $2^{(k+1)/2} - 1$ with k odd, therefore the correlation gain is $(2^k - 1)/(2^{(k+1)/2} - 1) \approx \sqrt{M/2}$. And assuming cross-correlation signals from the $(N-1)$ elements are independent, the total cross-correlation noise power is $S(N-1)/g$. Substituting (7.38) into (7.37) and noticing that $B = 1/\delta\tau$, one obtains

$$SNR \approx \left\{ \frac{kT(4\pi R^2)^2 4\omega_a}{P_t G_t A_r \sigma_0 f_p \tau_p c\lambda\delta\tau} + (N-1)/g \right\}^{-1} \tag{7.39}$$

where $\delta\tau$ contributes oppositely to the two components inside the braces (notice that g is related to M which is inversely proportional to $\delta\tau$). For a single pixel, maximum SNR is achieved for an optimal value of $\delta\tau$. With multi-pixel averaging, the random thermal noise power is effectively reduced by an approximate factor of $1/N_s$ (N_s is the number of pixels for averaging), while the cross-correlation noise is deterministic and remains unchanged. Therefore priority must be given to minimizing the cross-correlation level, which can be done by maximizing the chip length M. However $\delta\tau$ cannot be too small, or multi-pixel averaging will not sufficiently reduce the thermal noise power for reasonable values of N_s. Setting the SNR due to thermal noise to the order of -3 dB, and using the pre-assigned parameter values provided under (7.36), one obtains $\delta\tau \approx 0.5$ μs according to equation (7.36). This corresponds to a range resolution of $r_g \approx 75$m. On the other hand, the pulse repetition frequency f_p is dictated by the need to avoid range and Doppler ambiguities. The successive pulses are separated by a duration greater than the roundtrip light-travel time corresponding to a lunar hemisphere (i.e. $2R_m/c \approx 11.6$ ms). And the Nyquist sampling criterion requires f_p to be greater than the total Doppler bandwidth (zero-Doppler-offset [106] receiver assumed) of the illuminated area, in this case the antenna footprint of the 34-m reflector. With some safety margin, f_p is set to 31 Hz and the corresponding pulse repetition period is $T_p = 1/f_p \approx 32$ ms, an integer multiple of 4 ms which is chosen as τ_p, giving a radar duty cycle about 12%. Now the chip length M is about 8000 and Gold codes of 8191 chips long can be employed.

The number of array elements allowed in the system is then determined by the required signal to cross-correlation ratio $g/(N-1)$ and the correlation gain g, similar to that in a CDMA (code division multiple access) system. The worst scenario happens when the cross-correlation has a 90° phase shift from the desired signal so that the phase error ϵ_ϕ is maximized, as shown in Figure 7.9. In order to keep ϵ_ϕ (in degrees) below a certain threshold, e.g. 3°, the signal to cross-correlation ratio (in

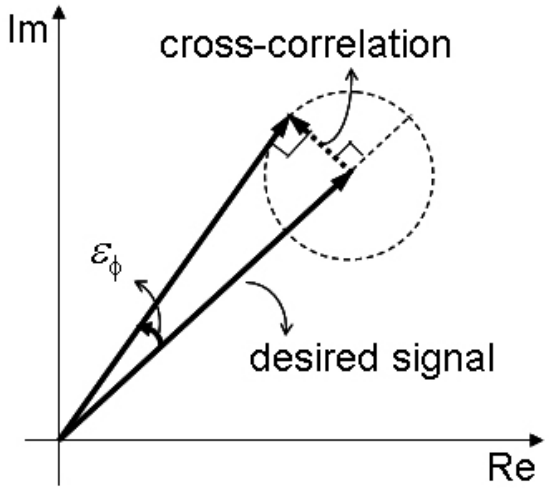

Figure 7.9: Phase error caused by cross-correlation.

power) has to be greater than 400, according to equation (7.31). Suppose a 36 dB correlation gain is available, the system capacity is approximately 11 array elements. It is also worth mentioning that although r_{az} seems irrelevant in equation (7.39), t_{coh} needs to be small, since the revolution of the Moon around the Earth requires the Earth antennas to rotate and track the imaging site on the Moon, but the array calibration has to be carried out for each fixed antenna orientation. A cross-range resolution of 5 km corresponds to about 4 seconds of observation time during which the Moon moves only about 4 km and the Earth antennas can track it without changing their attitude. Too big of a cross-range resolution is not desirable either, due to its decorrelation effect on the backscatter signals of different array elements.

According to the above system parameter design, a simulation example is presented as follows. A lunar surface pixel of size 80m $\times$ 5120m (8 grids $\times$ 512 grids) and the same surface roughness characteristics as were described in section 7.5.2 is generated at the location of 30° elevation, 0° azimuth. The rms height and correlation length are selected as 8m and 100m, respectively. The array elements under study are still located at their previous locations and there are 9 more elements contributing cross-correlation noise. Other system parameters take the values provided

Table 7.1: Effects of SNR on interferogram statistics (number of multiple pixels based on a 20.5 km × 20.5 km footprint)

Pixel Size (m)	single pixel SNR (dB)
80 × 5120	-2.4
$\hat{\overline{\phi}}_0$ (deg.): single pixel	STD (deg.): single pixel
9.0	81
$\hat{\overline{\phi}}_0$ (deg.): multi-pixel	STD (deg.): multi-pixel
12.5	3

under equation (7.36). 1000 realizations are generated to compute the interferogram statistics. To examine the multi-pixel averaging effect on thermal noise, 256 × 4 pixels inside a 20.5 km × 20.5 km illumination area are generated and the maximum likelihood estimator from equation (7.26) is used to calculate the interferogram. Simulation results are presented in Table 7.1, and notice that ϕ_{0c} is about 6.7°. As expected, the SNR for a single pixel is about -2.4 dB and thermal noise in this case dominates, causing a variation of more than 80° for the estimated interferogram. After averaging 1024 pixels, thermal noise is much reduced and only brings about 3° uncertainty on the interferogram estimation. However, the estimated inteferogram is about 6° away from ϕ_{0c}. This bias is a result of the cross-correlation noise in the worst case, i.e. 3° error for each of the two backscatter signals.

7.6.2 Surface Undulation

Surface undulation and roughness of the pixel are also likely to affect the interferogram statistics. It is trivial to show that an increase of the small scale roughness will increase the backscatter power, and hence the SNR, which will reduce the interferogram variance. The simulation conducted here is focused on the effect of different large scale undulation levels. The more abrupt the surface undulation, the more uncertain the equivalent phase center of the pixel will be, and hence the more spread of the interferogram. However a counter effect exists as well since the more abrupt

Table 7.2: Effects of surface undulation on interferogram statistics

rms Height (m)	$\hat{\bar{\phi}}_0$ (deg.)	STD (deg.)
8	12.5	3
80	12.5	5
800	12.5	4

surface tends to have more surface area which causes more backscatter. Similar simulations are carried out for pixels with a large scale rms height of 8m, 80m, and 800m while keeping the same correlation length of 100m. 1024 pixels are averaged for each simulation. The results are presented in Table 7.2, which shows that the surface undulation level has little effect on the interferogram distribution. This conclusion is reasonable since the ground antennas are so far away from the pixel that the details of the pixel surface may not be sensed. Therefore the surface undulation is not a concern when selecting imaging sites on the lunar surface.

7.6.3 Image Misregistration

So far, the pixel misregistration has been assumed to equal zero. The misregistration error is introduced and its effect on interferograms is examined in the following simulations. Two 80m $\times$ 5120m pixels are generated with shifts in location (Δx and Δy in Figure 7.3) set to 0×0, 1×64, and 2×128 grids, respectively (1 grid corresponds to 10m). Basically the pixel misregistrations are about 0, 0.125, and 0.25 pixel size, respectively. Results are presented in Table 7.3, where 1024-pixel averaging is still performed. The significant effect of pixel misregistration is observed. Although the MLE estimate remains relatively constant at the expected value, the standard deviation of the interferogram increases dramatically as the pixel shifts get larger due to signal decorrelation. A 0.125 pixel size misregistration renders a standard deviation of more than 50°, which is unacceptable for calibration purposes. With 0.05 pixel coregistration accuracy routinely available in InSAR imaging process [86], and

Table 7.3: Effects of pixel misregistration on interferogram statistics

Pixel Shifts (grids)	$\hat{\bar{\phi}}_0$ (deg.)	STD (deg.)
0×0	12.5	3
1×64	13.1	54
2×128	13.6	76

with more pixels for averaging, the variation in the estimated interferogram can be reduced to a specifically required value. Nevertheless, the pixel image misregistration error has to be minimized as much as possible during InSAR process, e.g. imaging sites with sharp features may be preferable due to their easy recognition for image coregistration.

7.7 Conclusions

In this paper an all-transmitter array phase calibration method is proposed for a ground array of large reflectors based on using different orthogonal PN-codes for transmit signal modulation at different array elements. Since it falls in the array far-field and does not have the positioning errors of LEO satellites, the Moon is selected as a calibration target. Lunar InSAR imagery has proven to be a promising technique that can be employed to perform uplink phase calibration. Although the long distance to the Moon causes huge signal path-loss and provides very low SNR for a single pixel, a large number of pixels inside the antenna footprint can be combined for multi-pixel averaging to reduce the phase difference estimation error. System parameters design is illustrated through an example where the pixel size is determined by a specified single pixel SNR, and the number of array elements allowed in the system is dictated by the correlation performance of the PN-codes used. A high-fidelity 3D lunar surface profile and scattering model is developed and used in conjunction with the Monte-Carlo technique to simulate the interferogram statistics. It is found that the pixel

surface undulation has marginal effect while the pixel misregistration effect is critical. One final comment on the proposed calibration technique pertains to the available calibration opportunities for different array orientations. With only a single orbit, the calibration opportunities provided by the Moon may be limited. Nevertheless, at the available opportunities, the lunar InSAR imagery technique is still a better option than using LEO calibration targets due to the extremely large positioning errors of the LEO targets.

CHAPTER 8

VLBI: DOWNLINK INFRASTRUCTURE FOR UPLINK CALIBRATION?

8.1 Introduction

The motivation for investigating VLBI (Very Long Baseline Interferometry) [107, 108] as a phase-calibration technique for large-reflector uplink ground arrays is to utilize existing infrastructures and techniques. The VLBI infrastructure is made up of an array of large reflector antennas (the VLBI receivers) operating in downlink mode. By modification of this existing facility, the array might be used as an uplink array. Even in the cases where building a new uplink array infrastructure is of interest, techniques used in VLBI may be helpful to phase calibrate the new array. For example, VLBI has extremely accurate positioning capability (better than GPS) that may be employed to determine the phase center of array element antennas. Another interesting point is that the VLBI receivers receive signals from celestial radiation sources, such as Quasars, which are so distant away that they essentially serve as far-field calibration targets. These Quasars are also abundant in the sky, occurring about every 4° of azimuth or declination, and are advantageous to the near-field LEO (low earth orbit) targets and the single-orbit target, Moon. The only disadvantage of the Quasars as calibration targets lies in the fact that they are so faraway that the signal arriving at VLBI receivers is essentially noise-like, causing very low signal-to-

noise ratio (SNR). Cross-correlation technique can be applied, in conjunction with extended observation (integration) time, to overcome such a problem.

In this chapter, the VLBI technique is reviewed, and then three different methods based on VLBI are proposed and their feasibilities studied. It has to be mentioned that the Very Large Array (VLA) [58] facilities, although constructed for different purpose, are similar to VLBI in terms of the cross-correlation processing. They are basically downlink arrays which receive signals from spacecraft and adjust the signal phases at different array elements in order to combine them coherently. The major distinction between VLBI and VLA is that VLBI emphasizes in measuring the time delay among signals at each receiver, while VLA is focused on cohering the phases. Although time delay and phase are highly correlated by nature, some additional techniques such as bandwidth synthesis have to be employed by VLBI to extract delay out of phase measurements. In addition, VLBI includes a significant part of theoretical modeling to derive the desired quantities from the measured delays. Since the interest of the uplink array calibration is mainly the signal phases, VLA is certainly considered a promising candidate for this purpose. However the review of VLA is not presented in this chapter since the VLA technique is a category of VLBI.

8.2 VLBI Review

VLBI is an interferometer operating at radio frequencies that makes use of Earth-based receivers separated by intercontinental distances observing a radio source in space. Analyses of the VLBI experiment data can measure relative positions of points on the Earth's surface at centimeter level and the angles between celestial objects at nanoradian level currently. If the receivers are separated by distances on the order of 1 km, i.e. they are located at the same area such as the BWG (Beam Waveguide) antennas at Goldstone, California, such arrangement is known as CEI (Connected

Element Interferometer) [107]. CEI experiments have the advantage that the receiver stations share a common frequency and time standard, and the experiment data analyses are performed in real time. However, its capability of measuring angular change is much weaker than VLBI since the angular change resolution is inversely proportional to the baseline distance.

Figure 8.1 shows the schematic diagram of a VLBI experiment. Two receiver antennas, separated by a baseline vector $\vec{B}$, detect the incoming wave front propagating along unit vector $\hat{k}$ from the same faraway radio source. There is a time delay between the arrival of the two signals at the receiver detectors, due to the separate locations of receiver antennas, the differences in the atmospheric paths, and the slightly different clock references for the two receivers. In order to extract such delay information, the received signals are sampled, digitized, and recorded into video tapes which are then taken to the SPC (Signal Processing Center). For CEI, recording signals in video tapes is not necessary, instead the signals from different receivers are sent to SPC via microwave transmission lines or fiber optics. A cross-correlation analysis is then performed on these recorded data and the so-called "observables" are generated which includes phase delay τ_p , group delay τ_g , and phase delay rate $\dot{\tau}_p$. The detailed signal processing procedure is described in [109, 108]. A brief derivation is presented as follows.

For simplicity let us first consider a monochromatic radio source in the absence of background and receiver noises. Suppose the received signals at the feed points of the two antennas can be represented as

$$V_1(\omega, t) = A_1 \cos(\omega t) \tag{8.1}$$

and

$$V_2(\omega, t) = A_2 \cos[\omega(t - \tau_g)] \tag{8.2}$$

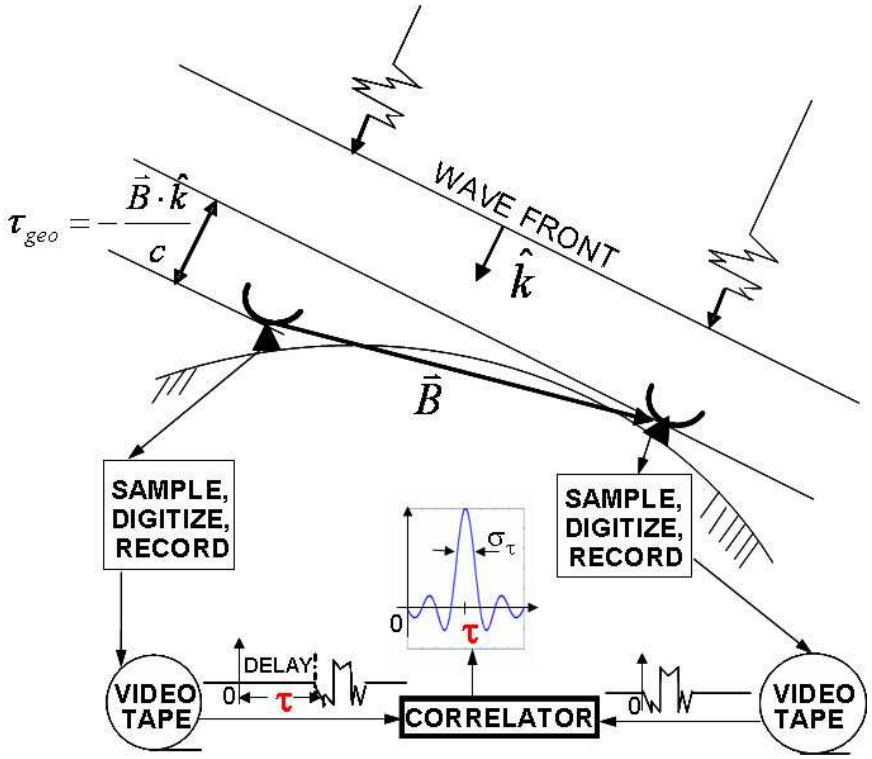

Figure 8.1: Schematic diagram of VLBI experiment.

where A_1, A_2 represent the signal strengths and τ_g represents the time delay (group delay). These signals are down converted to video band after superheterodyne processes and are given by

$$V_{1L}(\omega, t) = B_1 \cos[(\omega - \omega_{LO1})t + \theta_1] \tag{8.3}$$

and

$$V_{2L}(\omega, t) = B_2 \cos[(\omega - \omega_{LO2})t - \omega\tau_g + \theta_2] \tag{8.4}$$

where B_1, B_2 represent the strength of the video band signals, ω_{LO1}, ω_{LO2} represent the sum of local oscillator frequencies in the superheterodyne processes, and θ_1, θ_2 represent the sum of all instrument phase shifts caused by mixers, amplifiers, filters, cables, etc. The cross-correlation process between V_{1L}, V_{2L} consists of shifting V_{2L} in the time axis by *a priori* value τ_m that approximates the expected group delay

τ_g, multiplying the resulting signal by V_{1L}, and integrating (or low-pass filtering) the product. From (8.3) and (8.4), the cross-correlation function is given by

$$R(\omega,t,\tau_m) = \frac{1}{\Delta t}\int_{t-\Delta t/2}^{t+\Delta t/2} V_{1L}(\omega,t)\cdot V_{1L}(\omega,t+\tau_m)dt = \frac{1}{\Delta t}\int_{t-\Delta t/2}^{t+\Delta t/2}\frac{B_1B_2}{2}\cdot \left\{\begin{array}{l}\cos[(\omega_{_{LO2}}-\omega_{_{LO1}})t-(\omega-\omega_{_{LO2}})\tau_m+\omega\tau_g+\theta_1-\theta_2]+\\ \cos[(2\omega-\omega_{_{LO2}}-\omega_{_{LO1}})t+(\omega-\omega_{_{LO2}})\tau_m-\omega\tau_g+\theta_1+\theta_2]\end{array}\right\}dt \tag{8.5}$$

where Δt is the time interval of the integration. To filter out the high frequency term (the second term in the braces) in (8.5), $\Delta t \gg \pi/(\omega-\omega_{_{LO}})$ is required, where $\omega_{_{LO}}$ can be either $\omega_{_{LO1}}$ or $\omega_{_{LO2}}$ since the two frequencies are very close to each other. And because $\omega_{_{LO1}}-\omega_{_{LO2}}$ is approximately zero, the low frequency term (the first term in the braces) in (8.5) is slowly varying during the integration interval and can be evaluated by mid-point approximation, which results in

$$R(\omega,t,\tau_m) \approx \frac{B_1B_2}{2}\cos[\phi(\omega,t,\tau_m)] \tag{8.6}$$

with the phase function $\phi(\omega,t,\tau_m)$ given by

$$\phi(\omega,t,\tau_m) = \cos[(\omega_{_{LO2}}-\omega_{_{LO1}})t-(\omega-\omega_{_{LO2}})\tau_m+\omega\tau_g+\theta_1-\theta_2]. \tag{8.7}$$

In reality, the radio source signal received by VLBI receivers has broadband spectrum and can be approximated with a constant spectral density over the band of interest. In this case, the cross-correlation function is given by [109]

$$R(\omega,t,\tau_m) = D(\Delta\tau)\cos[\phi(\omega,t,\tau_m)] \tag{8.8}$$

where the amplitude function is given by

$$D(\Delta\tau) = KW\frac{\sin(\pi W\Delta\tau)}{\pi W\Delta\tau}. \tag{8.9}$$

K is a constant, W is the bandwidth of the video spectrum channel recorded at the receiver antennas, and

$$\Delta\tau = \tau_g - \tau_m. \tag{8.10}$$

There are two ways to determine the group delay τ_g from the cross-correlation function, namely from its amplitude function $D(\Delta\tau)$ or its phase function $\phi(\omega, t, \tau_m)$. The accuracy of determining τ_g from the amplitude function depends on the channel bandwidth W and the curve-fitting process. As shown in Figure 8.2, the ideal normalized amplitude function (shown as thick line) is a "sinc" function with its peak at $\Delta\tau = 0$ and first nulls at $\Delta\tau = \pm 1/W$. In practice, the value of the *a priori* τ_m, and hence the value of $\Delta\tau$, is varied. The corresponding cross-correlation function is then calculated and its amplitude value is recorded. These discrete values are plotted as those dots shown in Figure 8.2, which are fitted into a "sinc" function by standard least-square-error technique. The interpolated value of τ_m corresponding to the peak of this "sinc" function is therefore obtained as τ_g, according to (8.10). Typically this approach can estimate the delay with an accuracy of [63]

$$\sigma_{\Delta\tau} = \sigma_{\tau_g} \approx 0.005/W \sim 0.05/W. \tag{8.11}$$

For a typical VLBI receiver channel bandwidth of 2MHz, this accuracy is about 2.5 $\sim$ 25 nanoseconds, which is not sufficient for phase calibration at X-band or higher frequencies. For example, at 7.2 GHz the wave period is only about 0.14 nanosecond, and one wave period corresponds to 360° in phase. A higher accuracy in picosecond level is therefore needed, which would require recording the signal on a channel with

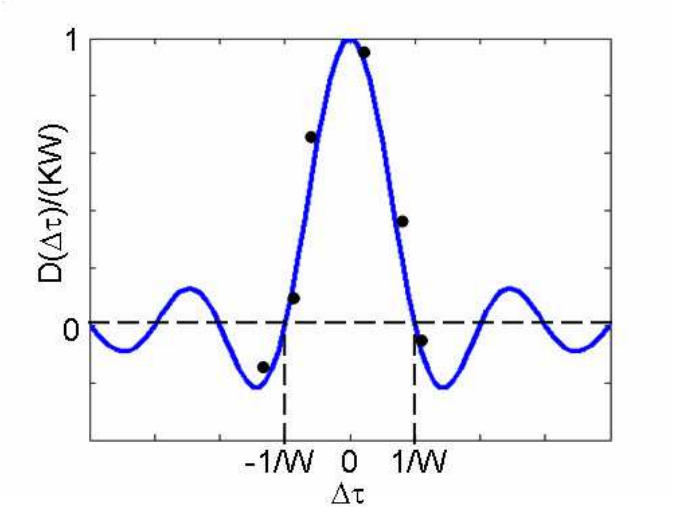

Figure 8.2: Illustration of the delay estimation accuracy using amplitude function.

much wider bandwidth, e.g 2 GHz. This is difficult to realize due to the requirement of ultra-wide band circuitry, extremely high signal sampling rate, and enormous data recording and computation capability.

Instead, an alternative way of using the phase function to determine the delay is routinely used in VLBI. In this approach, several channels with narrow bandwidths (e.g. 2 MHz). The phase values of the signal cross-correlation at each channel and at different moment are detected. These values are then fitted into a bilinear function, given by

$$\phi(\omega, t, \tau_m) = \tau_p \cdot \omega_0 + (\tau_g - \tau_m) \cdot (\omega - \omega_0) + \dot{\tau}_p \cdot \omega_0 \cdot (t - t_0) \tag{8.12}$$

where ω_0 stands for the center frequency of the first channel and t_0 the first moment to measure the radio signal from the source. The *a priori* value τ_m here is a best guess with the help of a preliminary amplitude function study. From this bilinear function, desired observables can be extracted out, such as the phase delay

$$\tau_p = \phi(\omega_0, t_0, \tau_m)/\omega_0, \tag{8.13}$$

the group delay

$$\tau_g = \tau_m + \frac{d\phi(\omega, t, \tau_m)}{d\omega}, \tag{8.14}$$

and the phase delay rate

$$\dot{\tau}_p = \frac{1}{\omega_0}\frac{d\phi(\omega, t, \tau_m)}{dt}. \tag{8.15}$$

The way to determine τ_g by equation (8.14) is the so-called bandwidth synthesis technique [110] in VLBI. As shown in (8.14), the estimation accuracy of τ_g depends on the measurement accuracy of the phase of the cross-correlation function and the total spanned frequency bandwidth, i.e. the separation between the lowest and highest frequency channels. While the total spanned bandwidth is limited by receiver hardware, e.g. the dispersiveness of wideband channels needs be taken into account, the phase measurement accuracy depends on the SNR of the cross-correlated signals. The current Goldstone CEI is capable of measuring τ_g at very high accuracy, e.g. 2$\sim$6 picoseconds using 34-m diameter BWG reflector antennas [111].

The last step in VLBI is to construct a physical model to interpret the measured delay observables. Such a model involves an unusually broad cross section of physics and can be divided into three components: the geometric delay model, the instrument delay model, and the atmospheric delay model [107]. Each component contains some parameters for estimation. Typically, *a priori* values of those model parameters are supplied first. Then the observables from measuring many different radio sources are processed to extract refined model parameters through a multi-parameter least-squares estimation algorithm. Problems with resolving ambiguities in the signal phase over large distances usually preclude the direct use of the phase delay observable τ_p. Therefore, the VLBI models are usually applicable to group delay τ_g and phase delay rate $\dot{\tau}_p$.

8.3 Uplink Array Calibration Using Baseline

One of the most powerful abilities of VLBI is its positioning capability. Using the group delay measurement results, in conjunction with an accurate physical model, the baseline vector between the two VLBI receivers can be determined very accurately which essentially provides an accurate reference position. For uplink array calibration, it is desired to determine the phase centers of array antennas based on this reference position. However the phase center of a large reflector antenna is generally a virtual point that cannot be located. In this case an RF probe technique can be employed where a non-invasive RF probe is placed at a grid of points on a near-field plane of the antenna to measure the electric fields. With these field information and the known positions of the corresponding points, the far-field radiation pattern of the antenna can be obtained through a Fourier transform operation [112]. This far-field pattern can be used for array calibration in such a way that it will be adjusted (by varying the phase of the transmitted signal from the antenna) until the radiated field at the desired place, e.g. at the spacecraft, is in phase for each array element.

The current standard VLBI positioning accuracy is at the centimeter level, however, great endeavors are being made to push that into millimeter range. This millimeter level accuracy is in fact what is needed for our uplink array calibration at X-band or higher frequencies. Next an example of baseline estimation using the state-of-the-art Goldstone CEI facility is presented in order to examine the possibility of achieving sub-centimeter accuracy and hence the feasibility of using baseline vector for array calibration. A recent two-receiver CEI measurement achieved picosecond-level accuracy in the group delay at X-band, which corresponds to millimeter-level accuracy in signal path-length [111]. It is hoped that the baseline vector estimation based on such a delay measurement can also reach the same accuracy. Basically there are six model parameters including the baseline vector (X, Y, Z), the difference of the zenith troposphere extent above each antenna, and the two linear coefficients of the receiver

clock offset drift are considered to have effects on τ_g. Other model parameters are assumed to be insignificant for the CEI case where the two receiver antennas are separated at only 0.5km level. The group delay consists of three components: the geometric delay, the receiver clock offset, and the tropospheric delay, represented by τ_{geo}, τ_c, and τ_{tr}, respectively.

First, the clock model is considered. Although CEI has the advantage of common frequency and time standards, the FODA (Fiber Optics Distribution Assembly) which delivers the frequency references brings in some additional delay. In addition, some differences in the geometric signal paths at the two receiver antennas are modeled as if they were "clocklike". By setting one station clock as the reference, the relative clock offset of the other station can be modeled as

$$\tau_c = \tau_{c1} + \tau_{c2}(t - t_0) + \tau_{c3}(t - t_0)^2. \tag{8.16}$$

Usually, only the linear portion of this model is needed unless the lack of synchronization of clocks between stations is too large.

Next, the geometric delay model is presented. Figure 8.3 shows the generalized geometric structure of a receiver antenna. **BE** is an axis fixed to Earth surface. **BA** rotates around **BE** to vary the azimuth angle of the antenna pointing. At the same time, **BA** serves as the second rotation axis around which **AD** rotates to change the elevation angle of the antenna pointing. The antenna is fixed to the point **D**. Since axis **BE** is fixed to the Earth surface, any point along this axis can be selected as the terminating point of the baseline vector. The point **B** is chosen here. The distance from **B** to the wave front plane **W** which contains point **A** is equal to L, which causes a delay L/c (c is the speed of light) for the wave to propagates from plane **W** to point **P**. Any delay along the axis **AD** up to the position of the feed (either inside the dish or buried underground) is absorbed into the clock model, since such a delay is

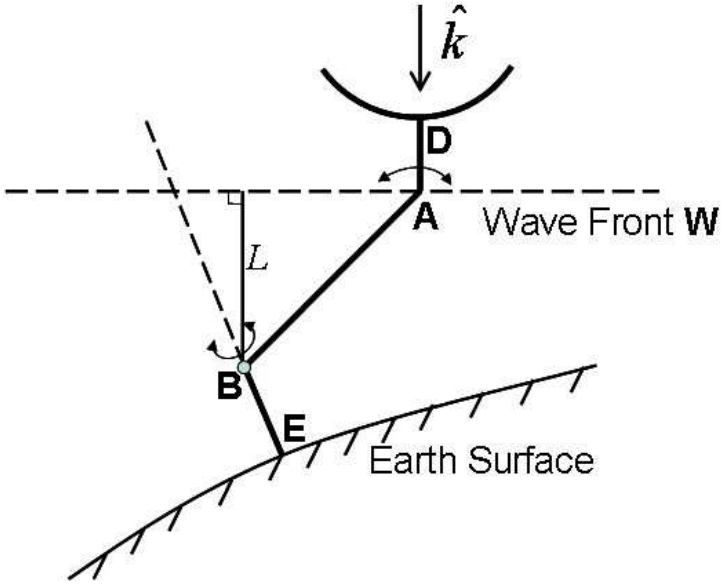

Figure 8.3: Generalized geometric structure of an antenna station.

independent of the antenna orientation and therefore indistinguishable from a clock offset. However, in reality gravity loading of the flexible dish structure changes the antenna's focal length and therefore affects such delay as antenna orientation varies. Some empirical formulations are used to account for such systematic error delay [107]. By considering all these facts, the geometric delay can be modeled as

$$\tau_{geo} = -\frac{\vec{B} \cdot \hat{k}}{c} - \frac{L_1 - L_2}{c} + (\tau_{sr1} - \tau_{sr2}) \tag{8.17}$$

where the subscripts "1" and "2" refer to antennas 1 and 2 as in Figure 8.1.

The last component of the delay model is the tropospheric delay. Troposphere exists at the lower few tens of kilometers of Earth's atmosphere. Radio signals passing through troposphere experience delay, bending, and attenuation relative to an equivalent path through a vacuum. The excess path delay caused by troposphere is

$$\tau_{tr}^{i} = \int_{S_i} (n-1) dS \tag{8.18}$$

where i refers to the antenna number 1 or 2, n is the index of refraction, and S_i represents the signal path through troposphere arriving at antenna i. Therefore the total tropospheric delay model for a given baseline is $\tau_{tr} = \tau_{tr}^1 - \tau_{tr}^2$. The tropospheric delay has two components, the dry and wet components, which correspond to the contributions from the dry air constituents and the water vapor. The zenith dry and wet delays due to the presence of troposphere are represented as Z_d and Z_w , in meters. And the so-called "mapping functions", $M_d(E)$ and $M_w(E)$, relate delays at an arbitrary elevation angle E to the zenith delay as

$$\tau_{tr}^i(E) = M_d(E) \cdot Z_d^i + M_w(E) \cdot Z_w^i. \tag{8.19}$$

The Goldstone CEI experiment was conducted at cold winter night when the air was assumed dry. Therefore, the tropospheric delay between two antenna stations can be modeled as

$$\tau_{tr}(E) = M_d(E) \cdot \Delta Z_d \tag{8.20}$$

where ΔZ_d is a model parameter representing the difference of zenith troposphere delays above the two antenna stations. The mapping functions are discussed in more detail in [107].

Accuracy of modeling any of the above three components directly affects the estimation accuracy of the model parameters in this component, and in other components as well. For example, the simplicity of a linear clock offset model and the mapping function of the troposphere delay model can result in inaccuracy of the estimation of baseline vectors at the centimeter or sub-centimeter level [107]. As another example, the empirical formulations used to account for system error delay caused by gravity loading of the large reflector are not very accurate, and the coefficients in such formulations have 5% error [107]. One more concern in the recent Goldstone CEI experiment is that the positions of the radio sources (Quasars) are pre-determined

from a reference frame constructed by previous VLBI measurements, which tend to have similar errors. Altogether, there are many challenges in achieving millimeter-level accuracy on baseline estimation by VLBI. And these challenges have not been fully addressed yet.

8.4 Uplink Array Calibration Using Group Delay

With the possibility of using the estimated baseline from VLBI for uplink array phase calibration closed for the time being, the direct use of the measured group delay is considered. In fact the delay maps to the phase by a multiplication of the operating angular frequency. Figure 8.4 proposes such a scheme where for each array element, the antenna is shared by the transmitter, and a VLBI receiver. When the antennas are connected to the VLBI receivers, the delay which consists of the group delay and the receiver instrument delay is measured, i.e.

$$\tau_g^{A\to R} = (\tau_{a1} + \tau_{r1}) - (\tau_{a2} + \tau_{r2}). \tag{8.21}$$

Similarly, when the transmitters connect to the VLBI receivers, the measured delay includes the instrument delay of both transmitter and receiver, given by

$$\tau_g^{T\to R} = (\tau_{t1} + \tau_{r1}) - (\tau_{t2} + \tau_{r2}). \tag{8.22}$$

Therefore the delay calibration value for uplink array operation where the transmitters are connected to the antennas can be obtained by

$$\Delta\tau = (\tau_{t1} + \tau_{a1}) - (\tau_{t2} + \tau_{a2}) = \tau_g^{A\to R} - \tau_g^{T\to R} + 2(\tau_{t1} - \tau_{t2}). \tag{8.23}$$

It is assumed that the instrument delay difference between the array element circuitries (excluding antennas) can be pre-characterized.

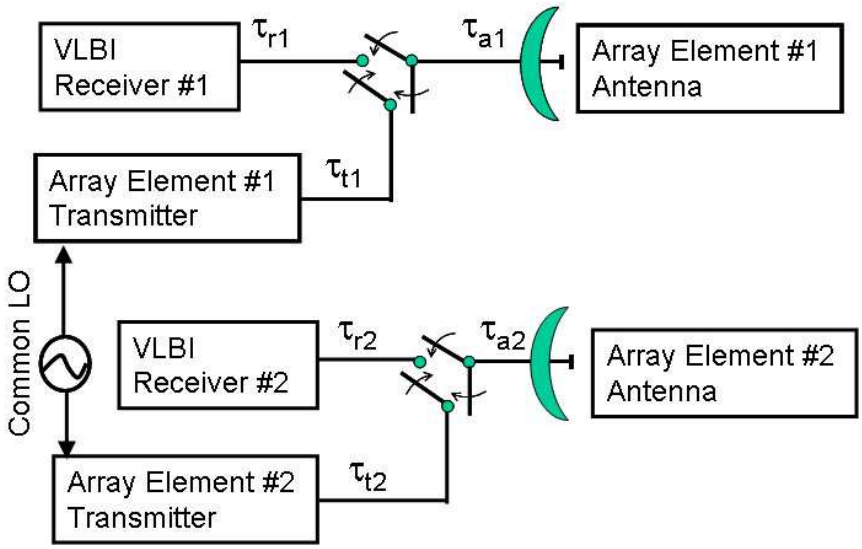

Figure 8.4: Uplink array calibration using group delay measured by VLBI receivers.

In order to examine the performance of such a calibration technique, an example of evaluating the measurement accuracy of τ_g is presented as follows. As mentioned earlier, the Quasars are so faraway that their radiated signals arriving at the VLBI receivers are like noise. Therefore the received signal power is given by

$$P_{ri} = KT_{ai}W, \tag{8.24}$$

similar to the noise power

$$P_{ni} = KT_{si}W. \tag{8.25}$$

Here $K = 1.38 \times 10^{-23}$ is the Boltzmann's constant and T_{ai} and T_{si} stands for the effective radio source temperature at the receiver antenna and the receiver system noise temperature (in Kelvin). The subscript $i = 1$ or 2, corresponds to the two VLBI receivers. T_{ai} can be calculated as

$$T_{ai} = \frac{1}{2}J \times 10^{-26}A_{ri}\eta_i/K \tag{8.26}$$

where J is the power flux from the radio source in Jansky ($= 10^{-26}$ watt/m^2/Hz), A_{ri} stands for the receiver antenna apertures, and η_i represents the antenna efficiencies at the two VLBI receivers. The factor $\frac{1}{2}$ accounts for antenna polarization loss. Assuming $J = 1$ Jansky which is true for many radio emitters, $A_{ri} = 12$ m, and $\eta_i = 64\%$, one can calculate T_{ai} to be less than 0.05 Kelvin, much less than a usual system noise temperature, 30 Kelvin. This is why the signal cross-correlation and extended integration (observation) time are necessary in VLBI to improve SNR. Suppose a single channel bandwidth W, the minimum sampling rate is then $2W$. With an observation time $\mathcal{T}_{obs}$, the effective signal processing gain is

$$g = 2W \cdot \mathcal{T}_{obs}. \tag{8.27}$$

The signal and noise powers out of the correlator are then given by $g(KT_{a1}W) \cdot (KT_{a2}W)$ and $(KT_{s1}W) \cdot (KT_{s2}W)$, respectively. Therefore the SNR can be computed as

$$SNR = \frac{2W \cdot \mathcal{T}_{obs} \cdot T_{a1}T_{a2}}{T_{s1}T_{s2}}. \tag{8.28}$$

Assuming a 2MHz channel bandwidth and 150 seconds observation time, one obtains a SNR value of about 460, i.e. more than 26 dB. Using the phase measurement accuracy formula [63], the phase of the cross-correlation function can be as accurate as

$$\sigma_\phi \approx \frac{57.3}{\sqrt{460}} = 2.7^\circ. \tag{8.29}$$

The accuracy of delay measurement using bandwidth synthesis is given by [63]

$$\sigma_{\tau_g} = \frac{\sigma_{\Delta\phi}}{\Delta\omega} = \frac{\sqrt{2}\sigma_\phi}{2\pi B_s} \tag{8.30}$$

where $\Delta\phi$ is the difference between the phase values obtained at the lowest and highest channels, B_s is the total spanned bandwidth. With the commonly used B_s, 500 MHz,

the highest accuracy of τ_g that can be achieved in the above VLBI system is about 21 picoseconds.

The requirement of the uplink array calibration at X-band on the delay accuracy is about 3 picoseconds. Therefore the 21 picoseconds accuracy provided in the above example is not sufficient. Either of the antenna aperture, the single channel bandwidth, the total spanned bandwidth, or the observation time, or the combination of some or all of them, must be increased. In fact, as mentioned earlier, the Goldstone CEI with 34-m antennas can achieve the required accuracy. However, there are still some issues about the proposed technique. First of all, the bandwidth synthesis in VLBI employs many separate channels resulting in a total spanned bandwidth of hundreds of megahertz. This is therefore a wideband system. Correspondingly the element transmitters connecting to the VLBI receivers have to provide the same bandwidth. It obviously brings up a challenge of characterizing the instrument delay for such a wideband system. In addition, there should be no dispersive devices allowed in the system due to the wideband spectrum. The most important concern lies in the fact that in this scheme the uplink array transmits in the same spectrum as the VLBI downlink. This may result in severe interference problem.

8.5 Uplink Array Calibration Using Phase Function

In this section a different calibration technique is proposed to overcome the challenges encountered in the previous section. In this approach, the spectrum of VLBI channels are not used. Instead the uplink array operates in its own frequency channels. The bandwidth synthesis used in VLBI is discarded, since the phase measurement of a single channel can be directly used for array calibration instead of the group delay. In fact, equation (8.29) shows very small phase error of the single channel measurement. This way the problems caused by wideband operation in the previous

technique are eliminated. The only concern left would be the requirement of operating at the same frequency channel in both uplink and downlink modes. If that can be justified, an even simpler scheme compared to Figure 8.4 can be adopted, based on the concept of phase conjugation. Figure 8.5 illustrates such a scheme. This scheme is very similar to that shown in chapter 6. The only distinction regards to the phase detection circuitry. While in Figure 6.1 the received signal phase at each array element is measured independently and sent to the wave generator for determining the phase calibration values applied to the uplink signals, the cross-correlator in Figure 8.5 directly collects all the received signals from array elements and computes the cross-correlation functions pairwise. The phases of these cross-correlation functions are in fact what is needed for phase calibrating the uplink array, and are sent to the wave generator to align the phases of the uplink signals. Such a cross-correlation and phase-alignment technique is indeed employed in the Very Large Array (VLA) as well. As mentioned earlier, another advantage of this calibration approach is that the Quasars, as calibration targets, fall in the array far-field zone, and they are abundant in the sky.

8.6 Conclusions

In this chapter, the possibility of using the existing VLBI/VLA infrastructures and techniques for the uplink array calibration is examined. The principle of VLBI technology is reviewed and three relevant calibration techniques are proposed. The first one is to make use of the VLBI positioning capability to determine the phase centers of the uplink array elements. This would not be successful due to the insufficient positioning accuracy. The second one takes advantage of the downlink group delay measured by VLBI and converts it into the proper usage for uplink array calibration. The major problem of this approach is that the uplink array has to work at the same wideband spectrum as that in VLBI, which is not feasible. The last method

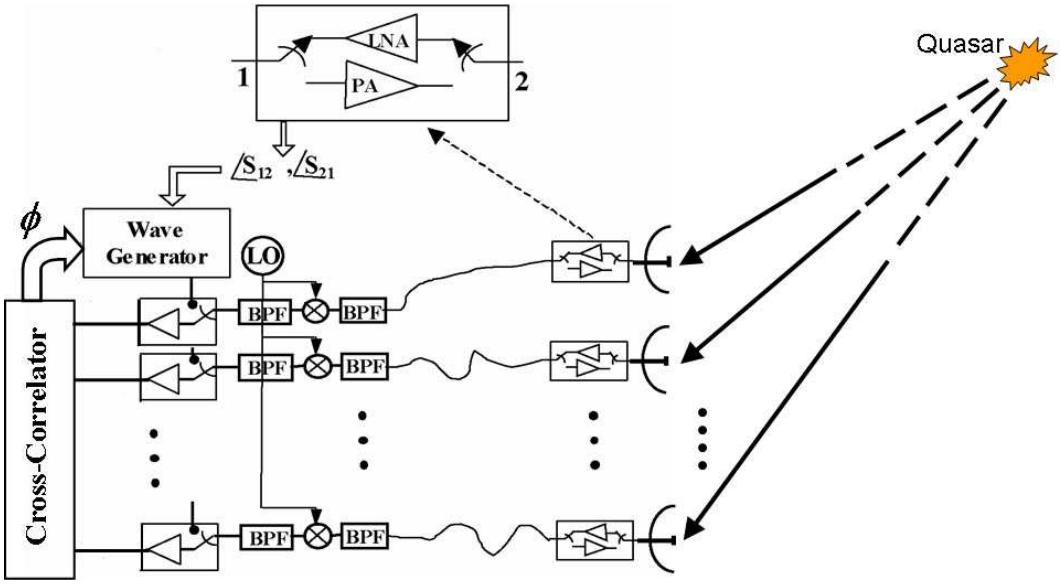

Figure 8.5: Uplink array calibration based on downlink cross-correlation and concept of phase conjugation.

does not use the existing VLBI infrastructures, instead it applies the cross-correlation technique in VLBI to a new uplink array calibration system. Since this technique essentially operates in a downlink mode, it requires a downlink circuitry in the system in addition to the uplink array. An example of such a downlink-uplink system based on the concept of phase conjugation is presented. Compared to the one described in Chapter 6, this new approach has the advantage of using array far-field targets for calibration. It has to be mentioned that if an uplink-mode-only array system is desired, this last approach also fails since it relies on downlink cross-correlation.

CHAPTER 9

Conclusions & Future Work

9.1 Conclusions

This dissertation includes two main parts. Each provides solutions for important applications in terrestrial or space wireless communications, namely, wave propagation through foliage and uplink ground array phase calibration. A physics-based modeling methodology is adopted throughout, in order to develop high fidelity wave propagation models for these applications. The emphases of the work for the two different applications, however, are not the same. While the solution for the foliage application lies in improving an existing single-scattering wave theory model by introducing more accurate and time-efficient algorithms and modeling procedures, the work for the array application develops a number of original calibration schemes.

In Chapter 2, the existing FCSM (fractal-based coherent scattering model) is reviewed for the application of foliage wave propagation. This model begins by generating a realistic-looking forested environment using fractal geometry. It then uses Foldy's approximation to estimate the propagation constant of the effective forest medium. Subsequently, the distorted Born approximation (DBA) method is applied, where the coherent mean-field is attenuated by the effective medium before hitting individual particles in the foliage. The scattered field from each particle is then co-

herently added at the receiver, after being attenuated by the effective medium as well. The limitations of such a model are pointed out and indicate the need for improvement. The major challenges are: 1) Foldy's approximation assumes a sparse medium where scatterers are independent and no mutual coupling occurs; 2) DBA is essentially a single-scattering approach, and the multiple-scattering effects must be considered at high frequency or for large propagation distances; 3) FCSM is too computationally intensive to be applied for large distance wave propagation in foliage; 4) FCSM is too complicated to be directly used by wireless communication system designers. The approach described in Chapter 3 overcomes the first challenge by including the mutual coupling among highly clustered scatterers, such as pine needle clusters, in Foldy's approximation. Both a full-wave MoM (Method of Moments) model and an approximate macro-model are employed to compute the scattering from a cluster of pine needles at millimeter-wave frequency. The approximate macro-model is computationally much less intensive than the MoM model. Comparison of the results of these models to the single-scattering results suggests that the attenuation rate of the effective forest medium is significantly overestimated if mutual coupling among needles is neglected at high frequency. In order to verify this simulation conclusion, an outdoor measurement is conducted for a pine tree stand at Ka-band (35 GHz). In this experiment 84 independent spatial samples of transmitted signal through the pine stand were collected to obtain the foliage path-loss statistics. The measurement results confirm the previous hypothesis obtained by simulation. By including multiple-scattering (i.e. mutual coupling) of clustered needles in FCSM, much better agreement is obtained for both the mean and standard deviation of the foliage path-loss.

A solution corresponding to the second and third limitations of FCSM is discussed in Chapter 4. The so-called SWAP (Statistical WAve Propagation) model for foliage path-loss estimation assumes the forest is statistically homogeneous along the direc-

tion of wave propagation, and the potentially large distance between the transmitter and receiver in the forest is divided into many statistically similar blocks of finite dimension. FCSM is then employed as a foundation and applied to a representative block of the forest. The statistical input-output field relationship including field attenuation and regeneration (due to scattering) for the representative block is computed by a Monte-Carlo simulation. These pre-computed statistical quantities of the forest are then applied to all blocks using a network theory. The overall received power, and hence the path-loss, is estimated by following the coherent and incoherent power through all the forest blocks. Compared to a brute force approach the computation time is significantly reduced while the prediction accuracy is maintained. This model is successfully validated both qualitatively through simulation results of foliage path-loss in a red pine stand, and quantitatively by comparing its predictions against independent propagation measurements in a pecan orchard.

Chapter 5 develops a foliage path-loss prediction macro-model, MiFAM (Michigan Foliage Attenuation Model), which is based on the SWAP model. This model has the advantages of empirical models which feature simple mathematical formulations and hence easy implementation. Additionally, it overcomes the restriction of empirical models and is more generally applicable. First, it is observed that besides the propagation distance the foliage path-loss is also a function of three other parameters. Such path-loss parameters in turn vary with the foliage parameters, such as tree hight, trunk diameter, tree density, branch density, wood moisture content, etc., as well as the radio system parameters, such as frequency and antenna height. Numerous SWAP simulations are carried out while varying the foliage and system parameters around their centroid values. Then a polynomial function curve-fitting process is conducted for the three path-loss parameters as a function of each of the foliage and system parameters. This results in a multivariate polynomial function for each of the three path-loss parameters, which jointly determine the foliage path-loss.

Therefore, MiFAM takes into account all the foliage and system conditions with an easy-to-use formulation. In this way both accuracy and simplicity are simultaneously achieved in the complicated and difficult task of foliage path-loss prediction. In this dissertation, MiFAM is successfully applied to two typical tree species, namely, the deciduous red maple and the coniferous red pine. There is no essential limit, however, to what kind of foliage MiFAM may be applied.

In the application of uplink array calibration, a phased array of many modest-size reflector antennas is employed to drastically improve the uplink effective isotropic radiated power (EIRP) of a ground station. Three potential schemes are proposed corresponding to different calibration targets they tend to use. In Chapter 6 a radar calibration procedure for the array phase distribution is presented using a number of low earth orbit (LEO) targets. The concept of phase conjugation is adopted for such a one-transmit-all-receive system where each array element is required to work both uplink and downlink. Design of optimal orbit and the number of LEO calibration targets is investigated in order to provide the frequent calibration opportunities needed as the array tracks a spacecraft. Array far-field focusing based on the near-field LEO targets through path-length compensation is also described and an analysis of array gain degradation based on the position error of the array elements and in-orbit targets is developed. It is shown that errors in the in-orbit targets' positions significantly degrade the far-field array gain while the errors in array elements' positions are not important. A similar analysis shows that phase errors caused by thermal noise, system instability, and atmospheric effects are insignificant factors in array gain degradation.

In order to eliminate the calibration target position error, Chapter 7 and Chapter 8 seek alternative candidates in the array far-field, namely, the Earth's natural orbiter, Moon, and celestial radio emitters, Quasars. In Chapter 7, a technique using lunar InSAR (Interferometric SAR) imaging to phase calibrate the ground array is studied. As a distributed radar target, Moon cannot be directly used like a point target

for calibration. The planetary SAR (Synthetic Aperture Radar) imaging technique is employed to isolate the whole antenna footprint on the lunar surface into many small pixels. Each array element can form a SAR image of a same pixel and the phase differences (interferograms) among these images can be used to perform phase calibration. An all-transmit-one-receive system scheme is adopted to reduce the unit cost of the array element due to the absence of a receiver. As a result, orthogonal PN (pseudo noise) codes have to be employed for different array elements to distinguish their signals at a common receiver. In order to evaluate the deviation of measured samples of phase differences from the desired values, a high-fidelity 3D lunar surface profile and scattering model is developed. Practical design of the calibration system parameters is illustrated through a real example. Simulation results are presented to show that the effects of image SNR (signal-to-noise ratio) and image misregistration are very important, while the surface undulation of the imaged pixels is insignificant.

The idea of using Quasars as calibration targets is inspired by the existing VLBI (Very Long Baseline Interferometry) technology. It would be beneficial if the existing VLBI facilities or the technique used by VLBI can be used for uplink array calibration. The only obstacle lies in the fact that VLBI is essentially a downlink technique. Directly using VLBI to determine the phase center of each array element antenna is proved to be infeasible due to insufficient positioning accuracy. Therefore some system modification is necessary in order to perform uplink phase calibration via the downlink VLBI facilities. There are two viable ways to do so. In the first approach, both the uplink array and the downlink VLBI share the same reflector antennas. The delay from the antenna feed to the far-field target is reciprocal and hence its uplink value can be obtained from the downlink calibration using VLBI. This approach assumes the instrument delays of the uplink array elements can be pre-determined through other measurement or calibration techniques. The second approach is based on the concept of phase conjugation. In this approach, the existing VLBI facilities are not

necessarily required. Only the cross-correlation technique used by VLBI (or VLA) is borrowed. This scheme is similar to that in Chapter 6, with the far-field active targets (Quasars) replacing the near-field passive targets (LEOs). An additional advantage is the abundance of Quasars which supplies sufficient opportunities to calibrate the uplink array at various attitudes.

9.2 Future Work

Future work involves further improvement of the SWAP (and hence MiFAM) model, validation of the MiFAM model, and experimental development of the uplink array calibration system. The details in each area are as follows.

1. **Multiple-scattering inside a single forest block needs to be accounted for in the SWAP model.**

   FCSM, which is applied to a typical block of forest in the SWAP model, is a single-scattering model, therefore multiple-scattering between scatterers inside this block is neglected. Consequently, the estimated wave propagation behavior within a single block is based on a single-scattering scenario. Although partial multiple-scattering is included through the network cascading approach described in Chapter 4, it only corresponds to multiple-scattering between scatterers inside different forest blocks. To complete the multiple-scattering SWAP model, new algorithms need be developed to take the multiple-scattering within a single block into account.

2. **MiFAM needs experimental validation.**

   MiFAM is simple-to-use and expected to be fairly accurate since it is based on simulation results of the well-developed SWAP foliage path-loss model. However, it would be more conclusive if MiFAM could be validated by a number of path-loss experiments conducted in various foliage environments. Measure-

ment data reported in the literature may not serve well due to incomplete ground truth or unsuitable foliage conditions. In this case new, carefully designed measurement systems need to be developed.

3. **The uplink array calibration schemes need to be tested using existing ground facilities.**

   The array calibration work in this dissertation is mainly conceptual and theoretical. The proposed calibration system schemes must be experimentally evaluated using some prototype array such as the 34-m BWG reflector antennas at Goldstone, CA. In particular, the schemes based on lunar InSAR imagery and VLBI are worth investigating in a concept-proof experiment. Before designing the hardware for such an experiment, however, there is additional theoretical work which is necessary. This work includes the PN-code selection and SAR image processing software for the lunar InSAR case, and the cross-correlation and phase detection algorithms for the VLBI case.

APPENDIX

Appendix A

A Faster Algorithm for Calculating the Scattered Field from a Pine Needle Cluster

At low frequencies where multiple-scattering is insignificant, scattering from a pine needle cluster, as shown in Figure 3.1, can be approximated as the coherent summation of the scattered fields from individual needles. A concise expression for such a far-field scattered field is obtained in terms of the polarizability tensor of a dielectric cylinder [50, 41], based on the low-frequency Raleigh scattering approximation. However this closed-form formulation is valid only in the local coordinates of a single needle. Therefore the traditional method of computing the needle cluster scattering involves transforming the incident field from the global cluster coordinates into the individual local needle coordinates, calculating the scattered field from each needle, then transforming back to the global coordinates for coherent addition. This method is inherently inefficient since the multiple coordinate transformations result in a computational slowdown. When processing thousands of needles in foliage, this slowdown dominates the run-time of the computer algorithm. In order to improve on the speed and efficiency of such an algorithm, it would be desirable to directly compute the scattering from a single needle in the global coordinates. It turns out that by a modification of the polarizability tensor this can be achieved.

In the local needle coordinates, as shown in Figure A.1, where the needle is oriented along the z-axis, the far-field scattered field from a very thin dielectric finite cylinder

(approximation of a pine needle) can be calculated as

$$\bar{E}_s = -\frac{e^{jk_0 r}}{4\pi r} A k_0^2 \left\{ \hat{k}_s \times \hat{k}_s \times \left[\overline{\overline{P}} \cdot \bar{E}_i \right] \right\} l \, \mathrm{sinc}(U) \tag{A.1}$$

where A is the area of the transverse cross section of the cylinder and l the length. r is the distance from the center of the needle to the receiver, k_0 is the free space wave number, $\bar{E}_i$ represents the incident field, $\hat{k}_s$ is the propagation unit vector to the observation position (coordinate origin is at center of cylinder), and $\overline{\overline{P}}$ is the polarizability tensor which can be expressed as

$$\overline{\overline{P}} = \begin{pmatrix} P_{xx} & 0 & 0 \\ 0 & P_{yy} & 0 \\ 0 & 0 & P_{zz} \end{pmatrix}. \tag{A.2}$$

For a right circular cylinder with relative dielectric constant ϵ_r , $P_{xx} = P_{yy} = 2(\epsilon_r - 1)/(\epsilon_r + 1)$, and $P_{zz} = \epsilon_r - 1$. The "sinc" function is given by

$$\mathrm{sinc}(U) = \frac{\sin(\pi U)}{\pi U}, \tag{A.3}$$

where

$$U = \frac{k_0 l}{2} (\hat{k}_s - \hat{k}_i) \cdot \hat{z}. \tag{A.4}$$

$\hat{k}_i$ is the propagation direction of the incident plane wave, and $\mathrm{sinc}(U)$ is a result of approximating a finite cylinder based on an infinite one. Such an approximation is valid when the length to radius ratio of the cylinder is large.

The above computations are performed in the needle local coordinates. In the cluster global coordinates, the needle is oriented (θ_t, ϕ_t), as shown in Figure A.2. Therefore, all vector quantities in the global coordinates must be first transformed into the local coordinates, via a coordinate transformation matrix $\overline{\overline{T}}$ from equation

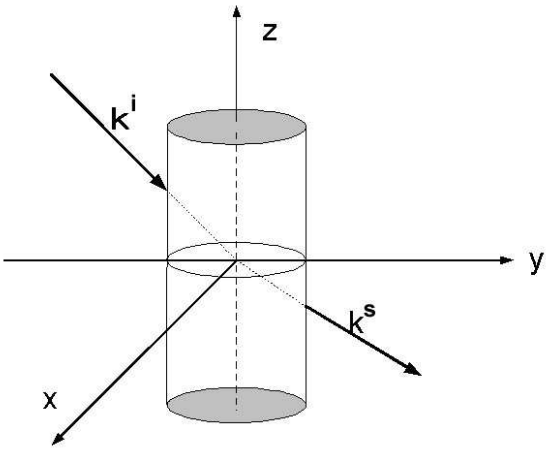

Figure A.1: Needle cylinder scattering in the local coordinates of the needle.

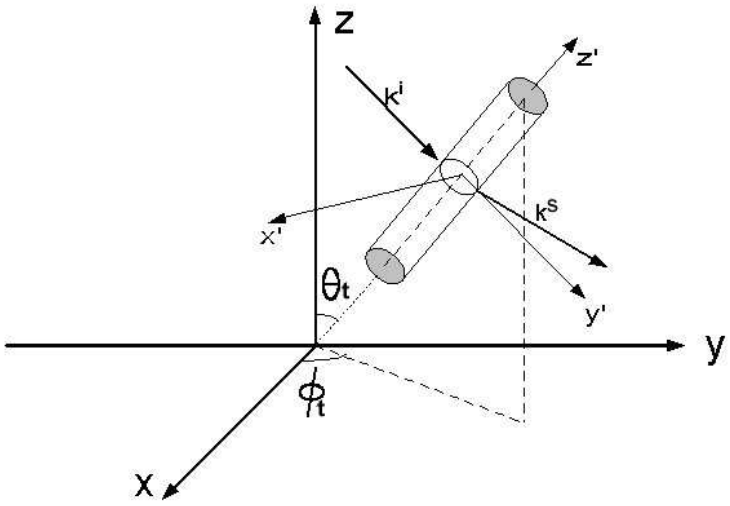

Figure A.2: Needle cylinder scattering in the global coordinates of the needle cluster.

(3.27), as

$$\hat{k}_s = \overline{\overline{T}} \cdot \hat{k}_s^g \tag{A.5}$$

$$\hat{k}_i = \overline{\overline{T}} \cdot \hat{k}_i^g \tag{A.6}$$

$$\bar{E}_i = \overline{\overline{T}} \cdot \bar{E}_i^g, \tag{A.7}$$

where the superscript "g" indicates global coordinates. After calculating $\bar{E}_s$ in local coordinates, it is then transformed back to global coordinates by

$$\bar{E}_s^g = \overline{\overline{T}}^{-1} \cdot \bar{E}_s. \tag{A.8}$$

Notice that each transformation will take 12 multiplications and at least 3 transformations are needed for each needle (it is not necessary to transform $\hat{k}_s$ and $\hat{k}_i$ for calculating U since U is a scalar and can be calculated directly in global coordinates).

After carefully examining equation (A.1), it is obvious that instead of transforming $\hat{k}_s$, $\hat{k}_i$ and $\bar{E}_i$ into local coordinates, it is much simpler to transform the local $\overline{\overline{P}}$ to global coordinates and then directly calculate the scattered field in global coordinates, i.e.,

$$\bar{E}_s^g = -\frac{e^{jk_0 r}}{4\pi r} A k_0^2 \left\{ \hat{k}_s^g \times \hat{k}_s^g \times \left[\overline{\overline{P}}^g \cdot \bar{E}_i^g \right] \right\} l \, \mathrm{sinc}(U) \tag{A.9}$$

Here, U is given by

$$U = \frac{k_0 l}{2} (\hat{k}_s^g - \hat{k}_i^g) \cdot \hat{l}, \tag{A.10}$$

where unit vector $\hat{l}$ represents the global orientation of the needle. The global polarizability tensor $\overline{\overline{P}}^g$ can be computed as

$$\overline{\overline{P}}^g = \overline{\overline{T}}^{-1} \cdot \overline{\overline{P}} \cdot \overline{\overline{T}}. \tag{A.11}$$

This can be proved by substituting (A.11) into (A.9) and performing a $\overline{\overline{T}}$ transformation on both sides, which will give the same expression as (A.1). Now the coordinate

transformations are encapsulated in the polarizability tensor and one can expand (A.11) to take advantage of the symmetric properties of the tensor. Specifically, $\overline{\overline{P}}^g$ can be written as

$$\overline{\overline{P}}^g = \begin{pmatrix} P^g_{xx} & P^g_{xy} & P^g_{xz} \\ P^g_{yx} & P^g_{yy} & P^g_{yz} \\ P^g_{zx} & P^g_{zy} & P^g_{zz} \end{pmatrix}, \tag{A.12}$$

where

$$P^g_{xx} = \frac{1}{\epsilon_r + 1}\left[2 + (\epsilon_r - 1)\sin^2\theta_t \cos^2\phi_t\right] \tag{A.13}$$

$$P^g_{yy} = \frac{1}{\epsilon_r + 1}\left[2 + (\epsilon_r - 1)\sin^2\theta_t \sin^2\phi_t\right] \tag{A.14}$$

$$P^g_{zz} = \frac{1}{\epsilon_r + 1}\left[2 + (\epsilon_r - 1)\cos^2\theta_t\right] \tag{A.15}$$

$$P^g_{xy} = P^g_{yx} = \frac{\epsilon_r - 1}{\epsilon_r + 1}\sin^2\theta_t \sin\phi_t \cos^2\phi_t \tag{A.16}$$

$$P^g_{xz} = P^g_{zx} = \frac{\epsilon_r - 1}{\epsilon_r + 1}\sin\theta_t \cos\theta_t \cos\phi_t \tag{A.17}$$

$$P^g_{yz} = P^g_{zy} = \frac{\epsilon_r - 1}{\epsilon_r + 1}\sin\theta_t \cos\theta_t \sin\phi_t. \tag{A.18}$$

Notice that only 14 multiplications are required to calculate $\overline{\overline{P}}^g$, taking the off-diagonal symmetry into account.

Another approximation which can speed up the algorithm is to assume $\hat{k}^g_s$ from each needle in the cluster is approximately the same as that from the center of the cluster. Since the cluster is small it appears as a point source in the far-field. It has to be mentioned that the $\hat{k}^g_s$ in the "sinc" function must be retained since small differences can be amplified by the multiplication with large k_0 at relatively high frequencies. Applying this approximation to (A.9), $\hat{k}^g_s$ is factored out from the braces. And the cross multiplication need only be performed once, after summing the contributions from all needles. The same technique can be applied to $\bar{E}_i$ as well as r. However the computation of r in the phase calculation must preserve the exact value.

Finally, the total scattered field from an N-needle cluster can be calculated as ("c" in the subscript stands for "cluster")

$$\bar{E}^g_{sc} \approx -\frac{Alk_0^2}{4\pi R}\hat{k}^g_s \times \hat{k}^g_s \times \left\{ \sum_{i=1}^{N} \left[\overline{\overline{P}}^g_i \cdot \bar{E}^g_i \right] \mathrm{sinc}(U)\, e^{jk_0 r} \right\}, \tag{A.19}$$

where R is the distance from the center of the cluster to the receiver, and the subscript "i" represents the i^{th} needle in the needle cluster.

BIBLIOGRAPHY

BIBLIOGRAPHY

[1] George M. Calhoun, *Third Generation Wireless Systems, Volume 1*, Artech House, Inc., Boston, MA, 2003.

[2] M.D. Casciato, *Radio Wave Diffraction and Scattering Models for Wireless Channel Simulation*, Ph.D. dissertation, Univeristy of Michigan, Ann Arbor, MI, 2001.

[3] K. Sarabandi and Il-Suek Koh, "A Complete Physics-Based Channel Parameter Simulation for Wave Propagation in a Forest Environment," *IEEE Trans. Antennas Propagation*, vol. 49, No. 2, pp. 260-271, 2001.

[4] Il-Suek Koh, *Advanced Diffraction and Wave Propagation Models for Characterization of Wireless Communication Channels*, Ph.D. dissertation, Univeristy of Michigan, Ann Arbor, MI, 2002.

[5] T. Okumura, E. Ohmori, and K. Fukuda, "Field Strength and Its Variability in VHF and UHF Land Mobile Service," *Review Electrical Communication Laboratory*, vol. 16, No. 9-10, pp. 825-873, 1968.

[6] A.G. Longley and P.L. Rice, "Prediction of Tropospheric Radio Transmission Loss Over Irregular Terrain, A Computer Method − 1968," Tech. Rep. ERL 79-ITS67, ESSA Research Laboratories, Washington, D.C., 1968, US Government Printing Office.

[7] M.A. Weissberger, *An Initial Critical Summary of Models for Predicting the Attenuation of Radio Waves by Trees*, Tech. Rep. ESD-TR-81-101, EMC Analysis Center, Annapolis, MD, 1982.

[8] R. Matschek and B. Linot, "Model for Wave Propagation in Presence of Vegetation Based on the UTD Associating Transmitted and Lateral Waves," *National Conference on Antennas and Propagation, Conference Publication*, No. 461, 30 March - 1 April, 1999.

[9] L.W. Li, T.S. Yeo, P.S. Kooi, and M.S. Leong, "Radio Wave Propagation Along Mixed Paths Through a Four-Layered Model of Rain Forest: An Analytic Approach," *IEEE Trans. Antennas and Propagation*, vol. 46, No. 7, pp. 1098-1110, November 1998.

[10] T. Tamir, "On Radio-Wave Propagation in Forest Environments," *IEEE Trans. Antennas and Propagation*, vol. AP-15, No. 6, pp. 806-817, November 1967.

[11] N.S. Chauhan, R.H. Lang, and K.J. Ranson, "Radar Modeling of a Boreal Forest," *IEEE Trans. Geosci. Remote Sensing*, vol. 29, pp. 627-638, 1991.

[12] K.C. McDonald, *Modeling Microwave Backscatter From Tree Canopies*, Ph.D. dissertation, University of Michigan, Ann Arbor, MI, 1991.

[13] S.S. Saatchi and K.C. McDonald, "Coherent Effects in Microwave Backscattering Models for Forest Canopies," *IEEE Trans. Geosci. Remote Sensing*, vol. 35, No. 4, pp. 1032-1044, July 1997.

[14] Yi-Cheng Lin and K. Sarabandi, "A Monte Carlo Coherent Scattering Model For Forest Canopies Using Fractal-Generated Trees," *IEEE Trans. Geosci. Remote Sensing*, vol. 37, No. 1, pp. 440-451, 1999.

[15] A. Ishimaru, *Wave Propagation and Scattering in Random Media*, IEEE Press, New York, 1997.

[16] L. Tsang, J.A. Kong, and R.T. Shin, *Theory of Microwave Remote Sensing*, John Wiley & Sons, Inc., New York, 1985.

[17] Y.C. Lin and K. Sarabandi, "Retrieval of Forest Parameters Using a Fractal-Based Coherent Scattering Model and a Genetic Algorithm," *IEEE Trans. Geosci. Remote Sensing*, vol. 37, No. 3, pp. 1415-1424, May 1999.

[18] Il-Suek Koh and K. Sarabandi, "Polarimetric Channel Characterization of Foliage for Performance Assessment of GPS Receivers Under Tree Canopies," *IEEE Trans. Antennas Propagation*, vol. 50, No. 5, pp. 713-726, 2002.

[19] F. Wang and K. Sarabandi, "An Enhanced Millimeter-Wave Foliage Propagation Model," *IEEE Trans. Antennas Propagation*, vol. 53, No. 7, pp. 2138-2145, July, 2005.

[20] M.O. Al-Nuaimi and A.M. Hammoudeh, "Measurements and Predictions of Attenuation and Scatter of Microwave Signals by Trees," *IEE Proc. Microwave Antennas Propagation*, vol. 141, No. 2, pp. 70-76, April 1994.

[21] D. Didascalou, M. Younis, and W. Wiesbeck, "Millimeter-Wave Scattering and Penetration in Isolated Vegetation Structures," *IEEE Trans. Geosci. Remote Sensing*, vol. 38, No. 5, pp. 2106-2113, September 2000.

[22] Neil Rogers *et al.*, *A Generic Model of 1-60 GHz Radio Propagation through Vegetation - Final Report*, QinetiQ Ltd., Malvern Technology Center, Mlvern, Worcs., WR14 3PS, May 2002.

[23] Il-Suek Koh, Feinian Wang, and K. Sarabandi, "Estimation of Coherent Field Attenuation Through Dense Foliage Including multiple-scattering," *IEEE Trans. Geosci. Remote Sensing*, vol. 41, No. 5, pp. 1132-1135, 2003.

[24] L.L. Foldy, "The multiple-scattering of Waves," *Phys. Rev.*, vol. 67, pp. 107-119, 1945.

[25] R.K. Tewari, S. Swarup, and M.N. Roy, "Radio Wave Propagation Through Rain Forests of India," *IEEE Trans. Antennas and Propagation*, vol. 38, No. 4, pp. 433-449, April, 1990.

[26] F.K. Schwering, E.J. Violette, and R.H. Espeland, "Millimeter-Wave Propagation in Vegetation: Experiments and Theory," *IEEE Trans. Geosci. Remote Sensing*, vol. 26, No. 3, pp. 355-367, May, 1988.

[27] *http://solarsystem.nasa.gov/missions/*, accessed in January 2006.

[28] *http://eis.jpl.nasa.gov/deepspace/dsndocs/810-005/*, document 101A, accessed June 2005.

[29] *http://eis.jpl.nasa.gov/deepspace/dsndocs/810-005/*, document 104A, accessed June 2005.

[30] G. J. Wells and R. E. Zee, "A feasibility study of techniques for interplanetary microspacecraft communications," *Proc. 17th Annual AIAA/USU Conference on Small Satellites*, Logan, Utah, 2003.

[31] V. Jamnejad, J. Huang, B. Levitt, T. Pham, and R. Cesarone, "Array Antennas for JPL/NASA Deep Space Network," *IEEE Aerospace Conference Proceedings*, vol. 2, pp. 2-911 - 2-921, 2002.

[32] W.A. Imbriale, S. Weinreb, V. Jamnejad, and J. Cucchissi, "Exploring the next generation Deep Space Network," *IEEE Aerospace Conference Proceedings*, vol. 2, pp. 2-901 - 2-910, 2002.

[33] M.S. Gatti, "The Deep Space Network large array," *IPN Progress Report* 42-157, May 2004.

[34] A. Mileant and S. Hinedi, "Overview of arraying techniques for deep space communications," *IEEE Trans. Communications*, vol.42, No. 2/3/4, Feb./Mar./Apr. 1994.

[35] B. Mandelbrot, The Fractal Geometry of Nature, W. H. Freeman, New York, 1982.

[36] P. Prusinkiewicz and A. Lindenmayer, *The Algorithmic Beauty of Plants*, Spring-Verlag, New York, 1990.

[37] Eric Mougin *et al.*, "Effect of Tree Structure on X-Band Microwave Signature of Conifers," *IEEE Trans. Geo. Remote Sens.*, vol. 31, No. 3, pp. 655-667, May 1993.

[38] M.L. Imhoff, "A Theoretical Analysis of the Effect of Forest Structure on Synthetic Aperture Radar Backscatter and the Remote Sensing of Biomass," *IEEE Trans. Geo. Remote Sens.*, vol. 33, No. 2, pp. 341-352, March 1995.

[39] Yi-Cheng Lin, *A Fractal-Based Coherent Scattering and Propagation Model for Forest Canopies*, Ph.D. dissertation, Univeristy of Michigan, Ann Arbor, MI, 1997.

[40] R. Schiffer and K.O. Thielheim, "Light Scattering by Dielectric Needles and Disks," *J. Appl. Phys.*, vol. 50, No. 4, pp. 2476-2483, 1979.

[41] Kamal Sarabandi, *Electromagnetic Scattering from Vegetation Canopies*, Ph.D. dissertation, University of Michigan, Ann Arbor, MI, 1989.

[42] J.M. Stiles and K. Sarabandi, "A Scattering Model for Thin Dielectric Cylinders of Arbitrary Cross Section and Electrical Length," *IEEE Trans. Antennas and Propagation*, vol. 44, No. 2, pp. 260-266, February 1996.

[43] K. Sarabandi, "Δk-Radar Equivalent of Interferometric SARs: A Theoretical Study for Determination of Vegetation Height," *IEEE Trans. Geoscience and Remote Sensing*, vol. 35, pp. 1267-1276, 1997.

[44] Johnson J.H. Wang, *Generalized Moment Methods in Electromagnetics*, Chapter 7, John Wiley & Sons, Inc., New York, 1991.

[45] Arthur D. Yaghjian, "Electric Dyadic Green's Functions in the Source Region," Proc. IEEE, Vol. 68, No. 2, pp. 248-263, 1980

[46] D. E. Livesay and Kun-mu Chen, "Electromagnetic Fields Induced Inside Arbitrary Shaped Biological Bodies," IEEE Transactions on Microwave Theory and Techniques, Vol. 22, No. 12, December, 1974

[47] *http://www.netlib.org/linpack*

[48] G. T. Ruck, *Radar Cross Section Handbook, Volume 1*, Plenum Press, New York, 1970.

[49] D. Polder and J.H. van Santen, "The Effective Permeability of Mixtures of Solids," *Physica*, vol. XII, No. 5, pp. 257-271, 1946.

[50] K. Sarabandi and T.B.A. Senior,"Low-frequency Scattering from Cylindrical Structures at Oblique Incidence," *IEEE Trans. Geosci. Remote Sensing*, vol. 28, No. 5, pp. 879-885, 1990.

[51] G.B. Arfken and H. J. Weber, *Mathematical Methods for Physicists, Fourth Edition*, Academic Press, San Diego, 1995.

[52] R.J.E. Clausius, *Die mechanische Behandlung der Electricität*, Abschnitt III (F. Vieweg, Braunschweig, 1879).

[53] Tsenchieh Chiu and K. Sarabandi,"Electromagnetic Scattering from Short Branching Vegetation," *IEEE Trans. Geosci. Remote Sensing*, vol. 38, No. 2, pp. 911-925, 2000.

[54] R. F. Harrington, *Time-Harmonic Electromagnetic Fields*, McGraw-Hill, New York, 1961.

[55] R.E. Collin and F.J. Zucker, *Antenna Theory*, McGraw-Hill, New York, 1969.

[56] *http://hort.ifas.ufl.edu/trees/CARILLA.pdf*, accessed in November 2005.

[57] Theodore S. Rappaport, *Wireless Communication Systems Principles & Practice*, Prentice-Hall, Inc., New Jersey, 2000.

[58] D.H. Rogstad, A. Mileant, T.T. Pham, *Antenna Arraying Techniques in the Deep Space Network*, . John Wiley & Sons, Inc., Hoboken, New Jersey, 2003.

[59] A. Leick, *GPS Satellite Surveying, 2nd Ed.*, John Wiley & Sons, Inc., New York, 1995.

[60] *http://www.stk.com*, accessed June 2005.

[61] *http://www2.jpl.nasa.gov/basics/bsf13-1.html*, accessed June 2005.

[62] *http://www.colorado.edu/geography/gcraft/notes/gps/gps_f.html*, accessed June 2005.

[63] J.I. Molinder, "A Tutorial Introduction to Very Long Baseline Inerferometry (VLBI) Using Bandwidth Synthesis," *DSN Progress Report*, 42-46, pp. 16-28, 1978.

[64] R.M. Dickinson, D.L. Losh, R.D. Barber, and J.K. Dempsey, "A phase-control approach for a large-element coherent microwave power uplink system," *IEEE Trans. Antennas Propagat.*, vol. 47, No. 3, Mar. 1999.

[65] D.S. Bagri, "A proposed array system for the Deep Space Network," *IPN Progress Report* 42-157, May 2004.

[66] *http://www.celestrak.com/columns/*, accessed June 2005.

[67] R.C. Dixon, *Spread Spectrum Systems, 2nd Edition*, John Wiley & Sons, Inc., New York, 1984.

[68] T.W. Thompson et al., "Radar Maps of the Moon at 70-cm Wavelength and Their Interpretation," *Radio Science*, vol. 5, No. 2, pp. 253-262, 1970.

[69] *http://eis.jpl.nasa.gov/deepspace/dsndocs/810-005/*, document 304, accessed June 2005.

[70] C.V. Jakowatz, Jr. *et al.*, *Spotlight-Mode Synthetic Aperture Radar: A Signal Processing Approach*, Kluwer Academic Publishers, Boston, 1996.

[71] R.O. Harger, *Synthetic Aperture Radar System: Theory and Design*, Academic Press, New York, 1970.

[72] S.A. Hovanessian, *Introduction to Synthetic Array and Imaging Radars*, Artech House, Norwood, MA, 1980.

[73] J.C. Curlander and R.N. McDonough, *Synthetic Aperture Radar: Systems and Signal Processing*, John Wiley & Sons, New York, 1991.

[74] W.M. Brown, "Synthetic Aperture Radar," *IEEE Trans. Aerosp. Electron. Syst.*, vol. 3, p. 217, 1967.

[75] Elachi, et al., "Spaceborne Synthetic Aperture Imaging Radars: Applications, Techniques, and Technology," *Proc. IEEE*, vol. 70, p. 1174, 1982.

[76] K. Tomiyasu, "Tutorial Review of Synthetic Aperture Radar with Applications to Imaging of the Ocean Surface," *Proc. IEEE*, vol. 66, p. 563, 1978.

[77] G.H. Pettengill, S.H. Zisk, and T.W. Thompson, "The Mapping of Lunar Radar Scattering Characteristics," *The Moon*, vol. 10, pp. 3-16, 1974.

[78] N.J.S. Stacy, *High-Resolution Synthetic Aperture Radar Observations of the Moon*, Ph.D. dissertation, Cornell Univ., Ithaca, NY, 1993.

[79] J.L.H. Webb, D.C. Munson, and N.J.S. Stacy, "High-Resolution Planetary Imaging via Spotlight-Mode Synthetic Aperture Radar," *IEEE Trans. Image Processing*, vol. 7, No. 11, pp. 1571-1582, 1998.

[80] J.L. Margot et al., "Digital Elevation Models of the Moon from Earth-Based Radar Interferometry," *IEEE Trans. Geo. Rem. Sensing*, vol. 38, No. 2, pp. 1122-1133, 2000.

[81] D. Just and R. Bamler, "Phase Statistics of Interferograms with Applications to Synthetic Aperture Radar," *Applied Optics*, Vol. 33, No. 20, pp. 4361-4368, 1994.

[82] J.S. Lee et al., "Intensity and Phase Statistics of Multilook Polarimetric and Interferometric SAR Imagery," *IEEE Trans. Geo. Rem. Sensing*, Vol. 32, No. 5, pp. 1017-1028, 1994.

[83] K. Sarabandi, "Derivation of Phase Statistics of Distributed Targets from the Mueller Matrix," *Radio Science*, Vol. 27, No. 5, pp. 553-560, 1992.

[84] R. Touzi and A. Lopes, "Statistics of the Stokes Parameters and of the Complex Coherence Parameters in One-Look and Multilook Speckle Fields," *IEEE Trans. Geo. Rem. Sensing*, Vol. 34, No. 2, pp. 519-531, 1996.

[85] F.T. Ulaby et al., "Fluctuation Statistics of Millimeter-Wave Scattering from Distributed Targets," *IEEE Trans. Geo. Rem. Sensing*, Vol. 26, No. 3, pp. 268-281, 1988.

[86] F.K. Li and R.M. Goldstein, "Studies of Multibaseline Spaceborne Interferometric Sythetic Aperture Radars," *IEEE Trans. Geo. Rem. Sensing*, Vol. 28, No.1, pp. 88-97, 1990.

[87] G. Franceschetti and R. Lanari, *Synthetic Aperture Radar Processing, Chapter 4*, CRC Press, New York, 1999.

[88] L.D. Jaffe, "Properties of Lunar Surface Material from Direct Observation by Spacecraft-Summary," *Radio Science*, Vol. 5, No. 2, pp. 185-187, 1970.

[89] N.J. Trask, "Ranger Photographs of the Moon," *Radio Science*, Vol. 5, No. 2, pp. 123-128, 1970.

[90] E.M. Shoemaker and E.C. Morris, "Physical Characteristics of the Lunar Regolith Determined from Surveyor Television Observations," *Radio Science*, Vol. 5, No. 2, pp. 129-155, 1970.

[91] G.L. Tyler and R. A. Simpson, "Bistatic Radar Measurements of Topographic Variation in Lunar Surface Slopes with Explorer 35," *Radio Science*, Vol. 5, No. 2, pp. 263-271, 1970.

[92] J.H. Patterson et al., "Chemical Analysis of the Lunar Surface in the Surveyor Program - Summary," *Radio Science*, Vol. 5, No. 2, pp. 181-183, 1970.

[93] T. Hagfors, "Remote Probing of the Moon by Infrared and Microwave Emissions and by Radar," *Radio Science*, Vol. 5, No. 2, pp. 189-227, 1970.

[94] R.A. Simpson, "Spacecraft Studies of Planetary Surfaces Using Bistatic Radar," *IEEE Trans. Geo. Rem. Sensing*, Vol. 31, No. 2, pp. 465-482, 1993.

[95] E. Bahar and M. Haugland, "Unified Full Wave Solutions to Interpret Apollo Lunar Surface Data," *IEEE Trans. Geo. Rem. Sensing*, Vol. 32, No. 1, pp. 72-77, 1994.

[96] *http://nssdc.gsfc.nasa.gov/planetary/factsheet/moonfact.html*, accessed June 2005.

[97] R.S. Sayles and T.R. Thomas, "Surface Topography as a Nonstationary Random Process," *Nature*, Vol. 271, pp. 431-434, 1978.

[98] H.E. Hurst, "Long-term Storage Capacity of Reservoirs," *Trans. Am. Soc. Civ. Eng.*, 116, pp. 770-808, 1951.

[99] D.E. Smith et al., "Topography of the Moon from the Clementine Lidar," *J. Geophys. Res.*, Vol. 102, No. E1, pp. 1591-1611, 1997.

[100] J.A. Goff and T.H. Jordan, "Stochastic Modeling of Seafloor Morphology: Inversion of Sea Beam Data for Second-Order Statistics," *J. Geophys. Res.*, Vol. 93, pp. 13,589-13,608, 1988.

[101] S. Nozette et al., "The Clementine Mission to the Moon: Scientific Overview," *Science*, Vol. 266, pp. 1835-1839, 1994.

[102] D. Saupe, "Algorithms fro Random Fracctals," in *The Science of Fractal Images by H.O. Peitgen and D. Saupe*, Eds. New York: Springer-Verlag, 1988, pp. 71-136.

[103] R. T. Austin, *Electromagnetic Wave Scattering By Power-Law Surfaces*, Ph.D. Dissertation, University of Michigan, Ann Arbor, MI 1994, section 5.3, pp. 85-88.

[104] A.K. Gabriel and R.M. Goldstein, "Crossed Orbit Interferometry: Theory and Experimental Results from SIR-B," *Int. J. Rem. Sensing*, Vol. 9, No. 5, pp. 857-872, 1988.

[105] G. Macelloni *et al.*, "Experimental Validation of Surface Scattering and Emission Models," *IEEE Trans. Geo. Rem. Sensing*, Vol. 38, No. 1, pp. 459-469, 2000.

[106] F.T. Ulaby, R.K. Moore, and A.K. Fung, *Microwave Remote Sensing: Active and Passive, Volume II*, Artech House, Inc., Norwood, 1982.

[107] O.J. Sovers, J.L. Fanselow, and C.S. Jacobs, "Astrometry and Geodesy with Radio Interferometry: Experiments, Models, Results," *Reviews of Modern Physics*, Vol. 70, No. 4, pp. 1393-1454, October 1998.

[108] F. Takahashi, T. Kondo, Y. Takahashi, and Y. Koyama, *Very Long Baseline Interferometer*, IOS Press, Inc., 2000.

[109] J.B. Thomas, "An Analysis of Long Baseline Radio Interferometry," *JPL Technical Report* 32-1526, Vol. VII, pp. 37-50, February 1972.

[110] A.E.E. Rogers, "Very Long Baseline Interferometry with Large Effective Bandwidth for Phase-Delay Measurements," *Radio Science*, Vol. 5, No. 10, October 1970.

[111] C.S. Jacobs, Private Communications, September 2004.

[112] C.A. Balanis, *Antenna Theory*, Chapter 12, John Wiley & Sons, Inc., New York, 1997.